UNIVERSITY OF CALIFORNIA, MERCED

INVESTIGATING AND MODELING THE MICROSTRUCTURE AND MECHANICAL PROPERTIES OF ADDITIVELY MANUFACTURED HIGH STRENGTH ALLOYS

by

Ala'aldin Alafaghani

A thesis submitted in partial satisfaction of the
requirements for the degree of
Doctor of Philosophy

in

Mechanical Engineering

Committee in charge:
Professor Jian-Qiao Sun, Chair
Professor Ala Qattawi
Professor Venkattraman Ayyaswamy
Professor Christopher Viney

The thesis of Ala'aldin Alafaghani is approved:

Professor Jian-Qiao Sun, Chair	Date
Professor Ala Qattawi, Co-Chair	Date
Professor Venkattraman Ayyaswamy	Date
Professor Christopher Viney	Date

University of California, Merced

To my parents. There is no doubt that without you I would not have made it.

Brother, those DoTA nights certainly helped.

ACKNOWLEDGEMENTS

I would like to thank my advisors Prof. Qattawi and Prof. Sun who guided me throughout my Ph.D. I also appreciate the help and guidance of my committee members Prof. Viney and Prof. Ayyaswamy. I wouldn't have been able to do it without your help.

I would like to thank my labmates Muhammad-Ali Nuryar and Md. Shah Jaman for their support and encouragement.

My wife, thank you. Long journey, huh?!

CURRICULUM VITAE

EDUCATION

Ph.D. in Mechanical Engineering, University of California, Merced, Dissertation "Post-processing additively manufactured parts to produce functional load-bearing parts" 2021

M.S. in Mechanical Engineering, University of California, Merced, 2019

B.Sc. in Mechanical Engineering, University of Jordan, Amman, Jordan 2014

ACADEMIC EMPLOYMENT

Graduate Student Researcher at the integrated design and manufacturing lab.
Aug 2015-Dec 2021

- Investigated the design considerations of additive manufacturing with a focus on powder bed fusion and fused deposition modeling.
- Performed a topology optimization case study for a load-bearing additively manufactured part to produce a function-based design.
- Developed data-driven predictive models of the mechanical properties of additively manufactured parts using an ensemble of artificial neural networks.
- Utilized multi-objective optimization algorithms to optimize multiple mechanical properties using particle swarm optimization and genetic algorithm.

Teaching Assistant at the School of Engineering, University of California, Merced.
Aug 2015-Dec 2020

- Teaching assistant for the following courses: Component Design, Computer-Aided Engineering, Fluid Dynamics, and Statics and Dynamics at UC Merced, responsible for grading and holding lab and discussion sessions.
- Received good reviews for ability to explain and communicate the material.

Graduate Student Mentor at the undergraduate research opportunity center.
May 2019-Aug 2019

- Mentored more than 20 undergraduate students during their scholarship in UROC (Undergraduate Research Opportunity Center), who were doing research in different labs
- Prepared and presented various workshops to prepare for graduate school applications, such as preparing for the GRE, preparing their personal statements and resumes.

AWARDS

- Graduate Dean's Dissertation Fellowship 2021
- Southern California Edison Fellowship 2021
- ME Bobcat Fellowship (University of California, Merced) 2021
- ME Graduate Travel Fellowship Award (University of California, Merced) 2017
- ME Bobcat Award (University of California, Merced) 2016

PUBLICATIONS

[1] **A. Alafaghani**, A. Qattawi, M.A. Ablat, J.Q. Sun, Modified Solution Annealing Heat Treatments of Powder Bed Fused Inconel 718. **(Submitted)**

[2] **A. Alafaghani**, M.A. Ablat, A. Qattawi, Modeling the Influence of Fused Filament Fabrication Processing Parameters on the Mechanical Properties of ABS Parts. **(Submitted)**

[3] **A. Alafaghani**, A. Qattawi, J. Truong, M.S. Jaman, J.Q. Sun, Optimizing Fused Deposition Modeling Processing Parameters Using Response Surface Method for Strong Parts, in: Vol. 1 Addit. Manuf. Adv. Mater. Manuf. Biomanufacturing; Life Cycle Eng. Manuf. Equip. Autom., American Society of Mechanical Engineers, Cincinnati, OH, USA: Submitted, 2020. https://doi.org/10.1115/MSEC2020-8528.

[4] M.A. Ablat, A. Qattawi, M.S. Jaman, **A. Alafaghani**, C. Yau, M. Soshi, J.-Q. Sun, An experimental and analytical model for force prediction in sheet metal forming process using perforated sheet and origami principles, Procedia Manuf. 48 (2020) 407–418. https://doi.org/10.1016/j.promfg.2020.05.063.

[5] **A. Alafaghani**, A. Qattawi, M.S. Jaman, M.A. Ablat, Microstructure and mechanical properties of direct metal laser–sintered 15-5PH steel with different solution annealing heat treatments, Int. J. Adv. Manuf. Technol. 105 (2019) 3499–3520. https://doi.org/10.1007/s00170-019-04404-8.

[6] A. Qattawi, D. Ulutan, **A. Alafaghani**, Prediction of Mechanical Properties of Direct Metal Laser Sintered 15-5PH Steel Parts Using Bayesian Inference: A Preliminary Study, in: Vol. 2 Process. Mater., American Society of Mechanical Engineers, 2019. https://doi.org/10.1115/MSEC2019-3052.

[7] **A. Alafaghani**, A. Qattawi, M.A.G. Castañón, Effect of manufacturing parameters on the microstructure and mechanical properties of metal laser sintering parts of precipitate hardenable metals, Int. J. Adv. Manuf. Technol. 99 (2018) 2491–2507. https://doi.org/10.1007/s00170-018-2586-5.

[8] **A. Alafaghani**, A. Qattawi, Investigating the effect of fused deposition modeling processing parameters using Taguchi design of experiment method, J. Manuf. Process. 36 (2018) 164–174. https://doi.org/10.1016/j.jmapro.2018.09.025.

[9] **A. Alafaghani**, A. Qattawi, M.A. Ablat, Design Consideration for Additive Manufacturing: Fused Deposition Modelling, Open J. Appl. Sci. 07 (2017) 291–318. https://doi.org/10.4236/ojapps.2017.76024.

[10] **A. Alafaghani**, A. Qattawi, B. Alrawi, A. Guzman, Experimental Optimization of Fused Deposition Modelling Processing Parameters: A Design-for-Manufacturing Approach, Procedia Manuf. 10 (2017) 791–803. https://doi.org/10.1016/j.promfg.2017.07.079.

SELECT PRESENTATIONS AND TALKS

[1] Prediction of Mechanical Properties of Direct Metal Laser Sintered 15-5PH Steel Parts Using Bayesian Inference: A Preliminary Study. Technical presentation in MSEC 2019 International Manufacturing Sience and Engineering Conference, June 2019. Erie, PA, USA.

[2] Modified Heat Treatments of DMLS Of Precipitate Hardenable Steel. Poster presentation in MSEC 2019/NAMRC 45/ICMP11, June 2019. Erie, PA, USA.

[3] Investigating the Effect of Fused Deposition Modeling Processing Parameters Using Taguchi Design of Experiment Method. Poster presentation in MSEC 2018/NAMRC 45/ICMP11 June 2019. Los Angeles, USA

[4] Effect of Processing Parameters on Fused Deposition Modeling parts. Technical presentation in ASME 2016 International Mechanical Engineering Congress & Exposition (IMECE 2016), November 2016. Phoenix, Az

[5] Introduction to additive manufacturing. Guest Lecturer, University of Toledo, Fall 2020.

[6] Introduction to design of experiments. Workshop, University of California: Merced, Summer 2020.

TABLE OF CONTENTS

LIST OF FIGURES

LIST OF TABLES

ABSTRACT

Laser-based powder bed fusion (LPBF) is an additive manufacturing method that fabricates parts layer by layer by fusing the raw material powder using laser as the energy source. Originally, LPBF was used for rapid prototyping due to its capability to fabricate prototypes whenever changes are introduced to the concept CAD model without lead-time or the need to modify the fabrication line. Due to the inferior mechanical properties such as strength and stiffness of the fabricated parts compared to conventionally manufactured parts, and the limited options of materials, additive manufacturing was not used to fabricate end user functional parts. However, the recent developments in the last decade such as the introduction of high-power lasers with more compatible wavelengths, and higher quality raw materials, provide the opportunity to produce functional parts with high mechanical properties. Currently, LPBF is capable of producing parts with near full relative density. However, these parts still suffer from high anisotropy, defects, residual stresses, and inferior tensile strength, and fatigue life. This dissertation investigates different approaches to render the manufacturing of load-bearing metallic parts using LPBF more effective and reliable. The work presented focuses on two alloys, 15-5PH stainless steel and Inconel 718, due to their comparability with LPBF and their use in aerospace and automotive industries where additive manufacturing can be used cost-effectively.

The microstructure and mechanical properties of LPBF parts are highly sensitive to the processing parameters during fabrication and post-processing. Metallic parts are sensitive to the laser power, laser scanning speed, hatch spacing, powder layer thickness, and the orientation of the part during fabrication. Several studies investigated the effect of the processing parameters on the relative density and mechanical properties of LPBF parts. It was found that the set of processing parameters required to obtain high relative density is usually different than the set of processing parameters required to optimize the mechanical properties. To achieve the full potential of LPBF parts this work aims at optimizing the microstructure and mechanical properties of parts fabricated with the set of processing parameters that maximizes the relative density of the part. Therefore, the first objective of this dissertation is to characterize the microstructure and mechanical properties of as-fabricated LPBF parts at room and elevated temperatures.

The second objective is to develop and investigate different post-processing heat treatments that aim to homogenize the microstructure, improve the reliability

of the parts, and identify the treatments that have the potential to improve fatigue strength and life.

Finally, the last objective of this dissertation is to develop predictive models that assist in estimating the effect of different heat treatments on the mechanical properties of LPBF produce parts. A hybrid approach of physical and data-based derived models was used to evaluate the influence of post-processing heat treatment on the tensile strength of additively manufactured Inconel 718.

Chapter 1

INTRODUCTION

Additive manufacturing (AM) is a generic term used to refer to all manufacturing methods that fabricate parts layer by layer by adding material instead of removing material as in machining. Additive manufacturing is defined by the American Society of Materials and Testing (ASTM) as a process of joining materials to make objects from 3D model data, usually layer upon layer, as opposed to subtractive manufacturing methodologies [1]. The idea of fabricating 3D parts layer by layer from 3D CAD models is 30 years old approximately with a patent by Pierre Ciraud which was later developed and licensed by DTM Corporation. Currently, there are different groups of AM technologies based on how the raw material is introduced and the method of fusing the material.

1.1 Types of Additive Manufacturing

1.1.1 VAT Photopolymerization

VAT Photopolymerization is an AM technology that uses photopolymer resins as the raw material out of which the part is fabricated layer by layer. Usually, a UV-light source is used to scan and cross-link the resin selectively to solidify the resin. The process starts by fusing a thin film of the resin on a substrate that moves away from the UV light whenever the fusion of a layer is completed alloying a new layer of the uncured resin to flow on top of the completed layers. This process is repeated until the parts is completed [2, 3]. This technology is limited to polymers that can be cured using UV light.

1.1.2 Material Jetting

Material jetting is an AM technology that is very similar to traditional ink printers. However, instead of jetting ink, material jetting uses cartridges that move horizontally across the build platform to deposit uncured photopolymer resin on a substrate. The deposited resin is cured using UV light. When the first layer is completed, the build platform moves down and the cartridge continuous to deposit the next layer. When the part is completed, it is cleaned up and further exposed to UV-light to further cure [4, 5]. This technology is limited to photopolymer resins that have suitable flow properties for jetting.

1.1.3 Binder Jetting

Binder jetting refers to AM methods that create objects from raw material in the form of fine powder by fusing it using a binder that is usually in a liquid state. The powder is introduced using a roller that pushes the powder from the storage bed and levels it on the powder bed. The printing head then deposits the binder on the powder to fuse it and create a solid layer. After the layer is completed the powder bed drops down in increments equal to the layer thickness chosen by the designer. Then a new layer of powder is introduced to the bed upon which the binder is deposited again to create a new solid layer [6, 7]. Usually, the as-fabricated part is called a green part, which is then post-processed by heat to strengthen the fusion between the layers.

1.1.4 Material Extrusion

Material extrusion refers to AM methods that use filaments as the raw material, which is fed to an extruder where it is heated and pushed through a nozzle. The extruded material is deposited on a substrate where it cools and solidifies. Once a layer is completed either the build platform drops down or the extruder goes up in increments equal to the desired layer thickness. The deposition of the next layer then starts and the process is repeated until the whole part is completed [8]. This process is suitable for thermoplastics and metals that have low melting temperatures. In addition to that, the raw material should have good flow characteristics so that the deposition is controlled. Fused Deposition Modeling (FDM), or sometimes called Fused Filament Fabrication (FFF), falls in this category.

1.1.5 Sheet Lamination

Sheet lamination refers to AM methods that use materials in the form of thin sheets which are bonded and cut to the shape of the desired object. The thin sheets can be fused using different methods depending on the material. Using a binding material between the sheets or using ultrasonic vibration are two of the most common joining methods in sheet lamination [9, 10]. Sheet lamination was applied successfully using metals such as aluminum, copper, and stainless steel. However, sheet lamination parts are usually used as prototypes and not for structural use.

1.1.6 Directed Energy Deposition

Directed energy deposition (DED) is one of the most promising AM methods. It uses fine metal powder as the raw material and laser as the energy source for melting and fusing the powder. Different variations use small cylindrical filaments as the raw material or electron beam as the energy source instead of the laser. The powder or filament is deposited coaxially with the laser which melts the powder and fuses it to the substrate. Subsequent layers are deposited and fused to the previous

layers until the part is completed. The layer thickness and deposited line width are controlled by processing parameters such as the laser power and powder feed rate. DED is currently capable of producing parts with near full relative density [11, 12]. One of the advantages of DED is its capability to produce parts with graded chemical composition by feeding different mixtures of powders at different regions of the part. However, the production of parts with overhanging features using DED is challenging, unless sufficient supports are provided [13, 14].

1.1.7 Powder-Bed Fusion

Similar to DED, powder-bed fusion (PBF) uses powder as the raw material, however, instead of supplying the powder coaxially with the laser, PBF uses a bed filled with powder mounted on a piston. Usually, laser energy is used to melt or sinter the powder to fuse it. Once a layer of the object is completed, the piston supporting the powder-bed drops down to allow for a new layer of powder to be leveled on top of the previous layers. The laser then fuses the new layers of powder to the previous layers until the part is completed. Due to the low energy of the laser and poor absorptivity of metal powders to the laser energy, powders of low melting points were mixed with metal powders to act as a binder. Once the green part is completed it was heat-treated to complete the fusion. However, these parts suffered from high porosity and low mechanical properties and were usually subjected to infiltration by other metals to densify them and improve their mechanical performance. Currently, high-power lasers are used with more compatible wavelengths to improve the metal powder's absorption of laser energy. Different brands of AM methods belong to the PBF group such as selective laser sintering, electron beam melting, and direct metal laser sintering [15–17].

1.2 Direct Metal Laser Sintering

This dissertation focuses on direct metal laser sintering (DMLS) because of its ability to produce near full dense parts with greater than 99% relative density.DMLS is a powder bed laser-based additive manufacturing method. It uses fine metal powder as the raw material and laser as the heating energy source to fuse the powder according to the 3D CAD model. The DMLS process starts by laying a thin layer of powder on the powder bed ranging between 20-40 µm. The powder is then fused by the laser by melting the powder or partially melting it. The small laser spot follows computer-controlled paths as in CNC machines. The laser paths are generated by a slicing software, that draws these paths by slicing the 3D CAD model into finite-thick layers and calculating paths to fuse the powder in these layers. The commands are sent by the slicer to the DMLS system using G-codes. After each layer is finished, the powder bed moves down by a distance equal to the layer thickness while the powder supply bed rises by the same amount, after which a roller helps in

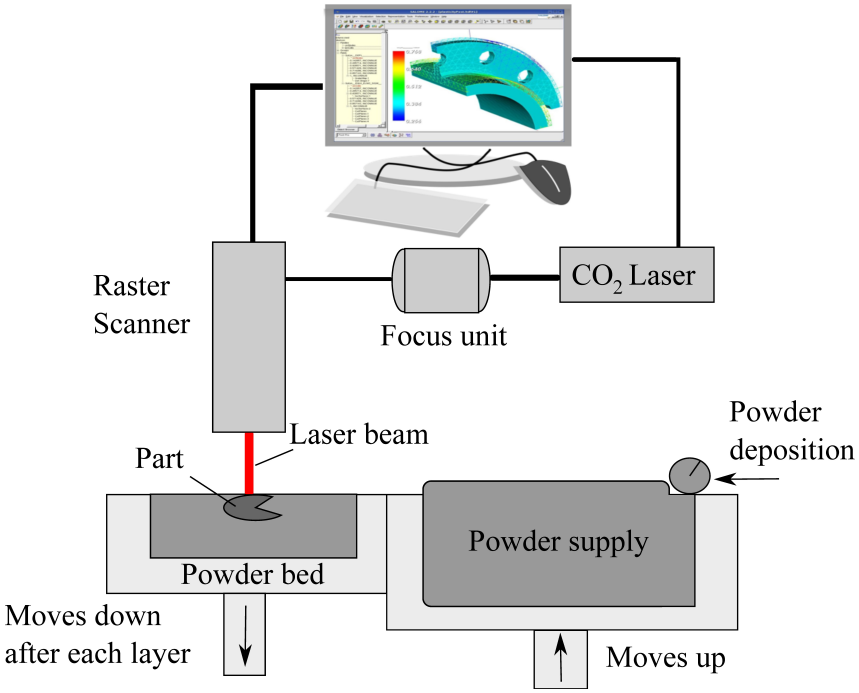

Figure 1.1: A schematic of LPBF.

distributing the powder evenly on top of the powder bed. This process is repeated until the part is completed. Figure 1.1 shows a schematic of the DMLS process.

Researchers studied the utilization of Ti-6Al-4V, Inconel 718 and 625, stainless steel 316 and 316L, precipitation hardening stainless steels 17-4 PH and 15-5PH, and the aluminum alloy AlSi10Mg metals in AM application [18]. These materials are suitable for AM due to the ability to produce it in powder form in addition to the ability to control metal flow during melting or sintering [19].

This research focuses on 15-5PH and Inconel 718 (IN718) metals. Both metals have good corrosion resistance, high stiffness, and tensile strength at elevated temperatures. In addition, both metals are precipitation hardenable materials, which makes them suitable for aerospace, automotive, chemical, and food processing applications [20–27]. 15-5PH can be precipitation hardened at different temperatures and durations resulting in a range of different tensile strengths, hardness values, and ductility values. This makes it suitable for a wide range of applications. IN718, on the other hand, is very hard to machine because of its high hardness and poor thermal conductivity [28]. Therefore, producing parts at or near-net shape mitigates this problem. Their use in the aerospace industry does not require mass production in many cases, which makes using them in parts produced using DMLS feasible.

1.3 Advantages of DMLS

The fabrication of parts layer by layer using DMLS directly from a 3D CAD model provides many advantages and bypasses many of the disadvantages of conventional manufacturing methods. DMLS can fabricate complex parts with shapes that would be otherwise impossible or very costly to produce. Using DMLS parts can be fabricated with internal features such as channels for heat exchangers or flow devices [29] or have internal structures that can support the mechanical loadings while minimizing the weight of the part and the material used [30]. This opens new opportunities for designs that focus more on the functionality of the part than on the fabrication process or design for manufacturing [31]. Topology optimized parts can be fabricated with no extra cost, where such parts might take long hours of machining to achieve [32]. This makes DMLS cost-effective for parts with high buy-to-fly ratios [33]. Furthermore, DMLS enables the production of functionally graded parts, where one or more properties can vary along the dimensions of the part. This is possible because the parts are fabricated layer by layer. The parts can have varying porosity across their length and varying support structures where needed [34]. Also, the material can vary continuously or discreetly across the layers which can produce parts with varying mechanical, thermal, or electrical properties [35]. This can open new fields of application for AM.

Economically, DMLS can be very advantageous in low volume production because every part's cost will be the material and energy required for its production. In conventional manufacturing, however, the production line, mold, tooling, labor and any dedicated machine for producing that parts will be added cost. Therefore, if the required production volume is small, these costs will be divided over a small number of parts making them very expensive [36]. Changing the design in conventional manufacturing might require a new casting or forging molds or modifying the production line. Additive manufacturing solves this problem by moving away from static designs and enabling engineers to produce multiple versions of a single design in a cost-effective manner and without additional lead time [37]. This makes it very convenient for highly customized products such as jewelry, dental and medical implants [38].

DMLS reduces material waste as most of the material not used can be directly recycled and used for later parts [39, 40]. DMLS produces parts that are at or near-net shape, post-processing such as machining and surface finishing are reduced significantly. DMLS can significantly reduce energy usage by using less material and eliminating steps in the production process [41]. No assembly is required, moving parts such as hinges and bicycle chains can be printed in metal directly into the product, which can significantly reduce the part numbers [42].

There are several economic advantages that are a product of the previous advantages. For example, additively manufactured topology optimized parts can have a high strength-to-weight ratio making them ideal for aerospace and automotive

industries. Since DMLS can produce parts combined, this reduces the number of parts and the assembly steps required. This has an impact on the storage needs and the transportation required to carry out these additional steps [43].

DMLS can be used to support conventional manufacturing methods. Rapid tooling is a technique where the molds are additively manufactured and then used for casting or injection molding. Different fixtures and special purpose tools can be manufactured on-site to support the operation or production in conventional manufacturing [44, 45].

1.4 Materials

This research focuses on 15-5PH and Inconel 718 (IN718) metals. Both metals have good corrosion resistance, high stiffness, and tensile strength at elevated temperatures. In addition, both metals are precipitation hardenable materials, which makes them suitable for aerospace, automotive, chemical, and food processing applications [20–27]. 15-5PH can be precipitation hardened at different temperatures and durations resulting in a range of different tensile strengths, hardness values, and ductility values. This makes it suitable for a wide range of applications. IN718, on the other hand, is very hard to machine because of its high hardness and poor thermal conductivity [28]. Therefore, producing parts at or near-net shape mitigates this problem. Their use in the aerospace industry does not require mass production in many cases, which makes using them in parts produced using DMLS feasible. This section describes the metals and their applications, composition, and crystal structures.

1.4.1 Traditional 15-5PH

The 15-5PH steel is a complex iron-based alloy. The main alloying elements in 15-5 PH are chromium, nickel, and copper as listed in Table 1.1. It is considered a low Carbon steel with a composition weight% less than 0.007wt% Carbon which is demonstrated in Figure 1.2. Chromium increases the corrosion resistance by creating an impermeable Cr2O3 scale on the alloy to reduce further corrosion in addition to stabilizing the Martensite body-centered cubic (BCC) phase structure. On the other hand, nickel stabilizes the Austenite phase face-centered cubic (FCC) structure and increases the corrosion resistance and toughness. The copper is added to introduce the precipitate hardening effect to the alloy. Manganese is kept higher than the expected sulfur content and acts as a sulfur getter [46]. Manganese sulfides form evenly throughout the grains instead of the detrimental iron sulfides at grain boundaries. Manganese is limited because it is an Austenite stabilizer. Excess quantities have a similar effect as nickel. Silicon is also used in limited quantities. Small amounts will increase corrosion resistance, but larger amounts can cause unwanted brittle phases to form. It is also a Martensite/Ferrite phase promoting element. Molybdenum is also a Martensite/Ferrite phase promoting element and, in

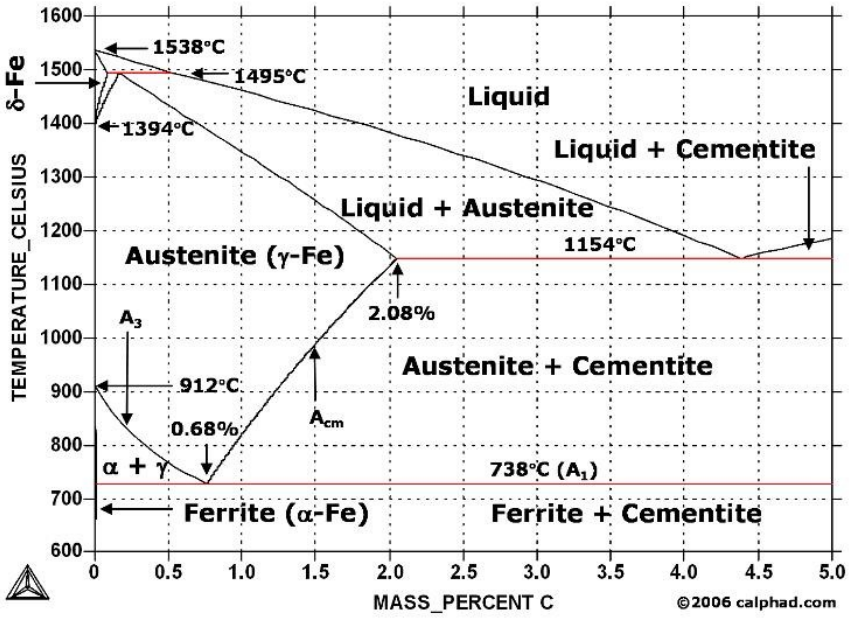

Figure 1.2: Stainless steel phase diagram

small quantities, can increase corrosion resistance when paired with chromium. In controlled amounts, niobium will preferentially be a carbon getter to form carbides that are less harmful to the alloy than other undesired carbides that would otherwise form. The carbides will form preferentially in the Martensite lath and grow to a size of approximately 35 to 45 nm. It is also a Martensite/Ferrite phase promoter. Carbon is limited because in excess it will promote Austenite phase formation by preferentially precipitating carbides in the grain boundaries.

Traditional 15-5PH steel is usually heated above its A3 temperature (1038 ± 14 °C) to transform its phase from BCC crystalline structure of Ferrite to the FCC phase of Austenite [47] refer to Figure 1.2 [48]. The extra space in the FCC crystal structure of the Austenite phase allows more carbon to be dissolved. The alloy is cooled rapidly so that the dissolved carbon does not have time to diffuse back from the FCC resulting in a highly strained body-centered tetragonal (BCT) crystal structure, which is known as Martensite [49]. To guarantee full transformation the rapid cooling should not stop until the temperature of the part is below 100°C as

Table 1.1: Accepted chemical composition in weight percentage of the 15-5PH alloy

15-5PH	Cr	Ni	Cu	Mn	Si	C	Mo	Nb	Fe
	14.0-15.5	3.5-5.5	2.5-4.5	1.00 max	1.00 max	0.07 max	0.5 max	0.15-0.45	Bal

shown in the time-temperature-transformation (TTT) diagram Figure 1.3 [50]. The steel is further strengthened without heat treatment, because of the shear deformation caused by the dissolved carbon atoms. The heat precipitation hardening treatments for 15-5PH steel are done by heating the alloy to a lower temperature ranging between 900 and 1150 F (482 -621 °C) during which a copper-rich ϵ-phase regions nucleate and grow until a designed particle size of 4 nm to 45 nm is reached based on the selected precipitation hardening heat treatment [51]. The copper-rich precipitates form 9R crystal structures. They grow with higher temperature heat treatments to become elliptical in shape and have an FCC crystal structure [52]. These particle sizes are effective in impeding dislocation movement and provide a semi-coherent interface, therefore hardening the alloy.

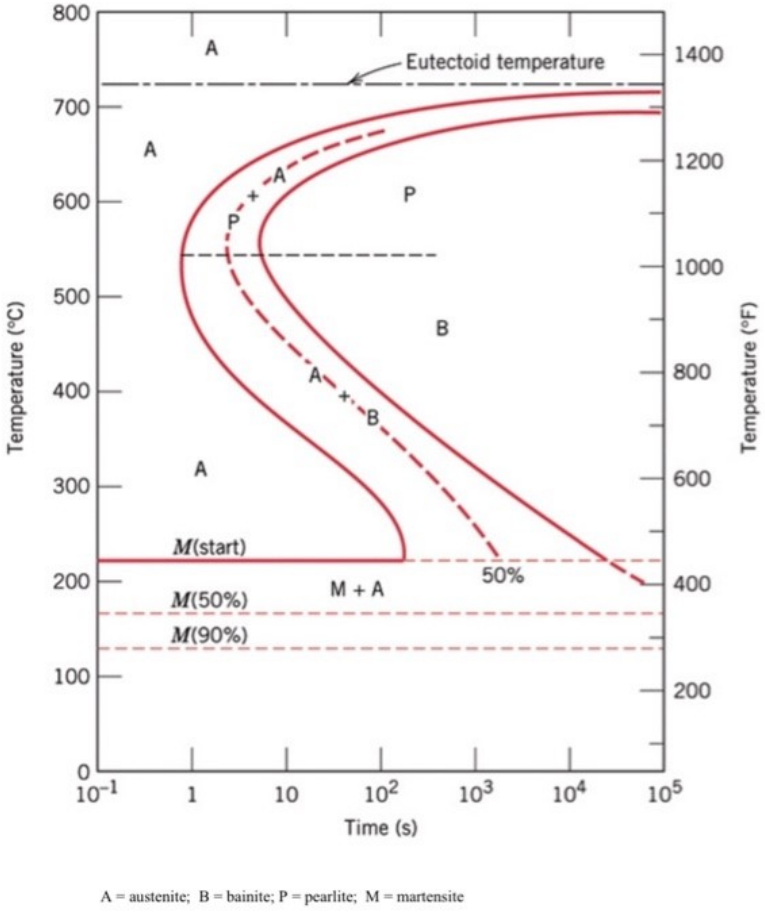

Figure 1.3: Stainless steel TTT diagram

1.4.2 Traditional Inconel 718

Nickel-based superalloys such as IN718 are currently used in many high-end applications such as aerospace and nuclear industries. IN718 has a high-temperature strength and excellent corrosion resistance needed for components such as jet engines, gas turbines, and rocket motors. It is used in nuclear reactors and cryogenic tanks, as well. Specifically, Inconel alloy 718 is used for high strength, corrosion-sensitive applications, between -423 and 1300°F [53]. The structure of nickel-based superalloys is primarily that of nickel, which has an FCC crystal structure. This is beneficial for high-temperature applications because it provides a good combination of toughness and ductility. In addition, IN718 has no phase transformation from room temperature to the melting point, so the alloys maintain their properties well over a large temperature range. Nickel-based superalloys are relatively light and inexpensive [54]. The acceptable chemical composition of IN718 alloy is listed in Table 1.2. Wrought Inconel mainly exhibits FCC Nickel γ phase due to the relatively low Nb wt% as can be observed from Figure 1.4 [55]. Three more metastable intermetallic phases that precipitate out of the γ matrix: γ' (FCC), γ" (BCC), and δ (simple orthorhombic) constitute the main phases present in IN718 [56, 57]. Each alloying element has a purpose determined by its properties Ni, Co, Fe, Cr, Ru, Mo, Rh, and W all have similar atomic radii to Ni and, therefore, act as γ-matrix stabilizers. Al, Ti, Nb, and Ta promote ordered phase formations and tend to have larger atomic radii (though Al is smaller than some stabilizers). Both much smaller (B and C) and much larger (Zr) atoms tend to segregate to grain boundaries. Creep resistance is improved by the low interdiffusion coefficients of Ir, Re, Ru, Pt, W, Rh, and Mo [58]. During solidification, Nb, Mo, and Ti segregate to the interdendritic regions [59]. Cr adds corrosion resistance, and Co increases the solubility temperature of γ", which increases the maximum service temperature.

The γ' phase (Ni3Al) and γ" (Ni3Nb) phase are the main strengthening phases in IN718. Therefore, after IN718 parts are solution annealed they undergo precipitation strengthening heat treatment at temperatures between 620°C - 750°C to precipitate γ' and γ" as shown in Figure 1.5 [60]. The δ (Ni3Nb) orthorhombic delta phase, has the same composition as γ" precipitates but with a different crystal structure. This phase is usually found along grain boundaries after homogenization and solution heat treatments but can also be within grains coincident with the 111 planes [61]. A γ"-BCT phase is present in the γ-FCC (face-centered cubic) matrix as a precipitate of oblong geometry with an average size of 250 nm long by 7 nm

Table 1.2: Acceptable chemical composition in weight percentage of the IN718 alloy

IN718	Ni	Cr	Nb	Mo	Ti	Al	Co	Cu	C	Si, Mn	P, S	B	Fe
wt%	50-55	17.0-21.0	4.75-5.5	2.8-3.3	0.65-1.15	0.20-0.80	1.0 max	0.3 max	0.08 max	0.35 max	0.015 max	0.006 max	Bal

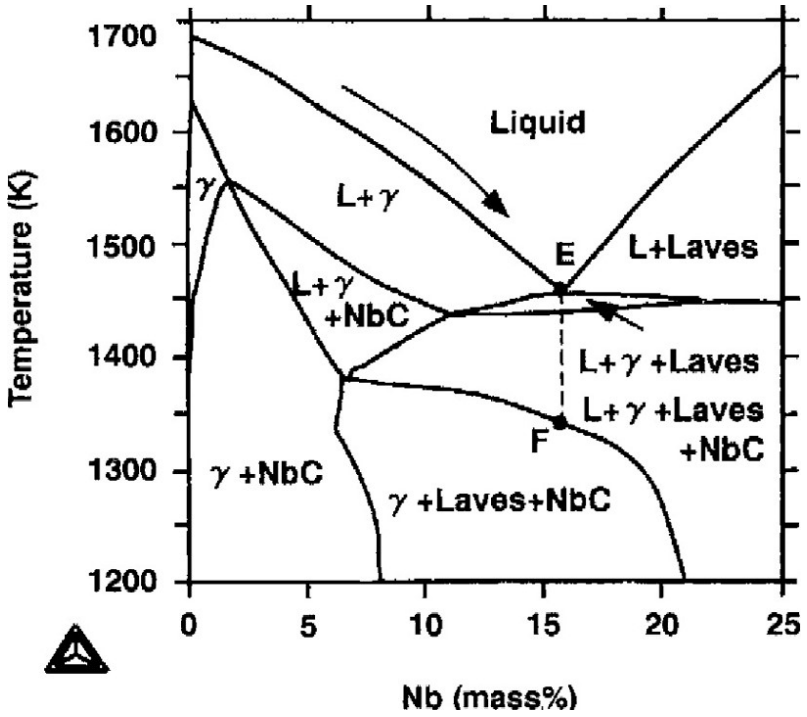

Figure 1.4: Inconel 718 phase diagram

in height [62]. The size of γ"-BCT precipitates controls mechanical properties in IN718, with courser precipitates yielding higher tensile strength [63]. The γ"-BCT precipitate is coherent with the γ-FCC matrix causing distortion of the lattice. The strain induced adds an extra barrier for dislocation movement, thus increasing the strength of the material. Furthermore, the γ"-BCT phase is stable to 600 °C. Following stability loss of the precipitate, the mechanical properties drop off exponentially [64]. Though preferred, γ" is much more difficult to observe in the microstructure since it is in the nanoscale [54, 65].

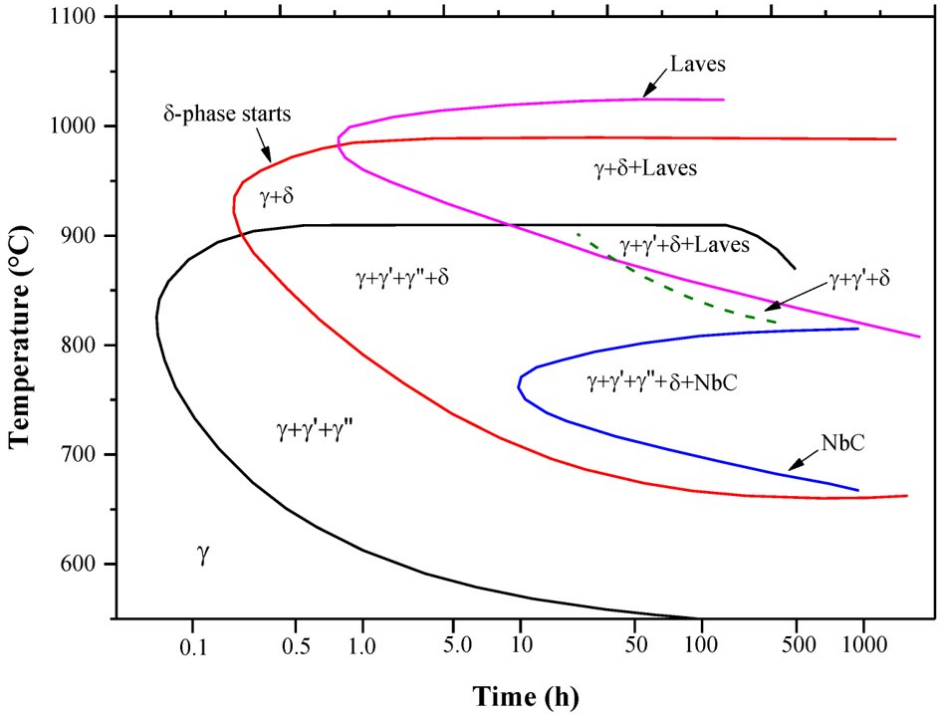

Figure 1.5: Inconel 718 TTT diagram

1.5 Literature Review

1.5.1 Influence of DMLS Processing Parameters on Additively Manufactured Parts

Laser additive manufacturing has been studied considerably in the last two decades. Much of that research aimed at optimizing the processing parameters to increase the relative density of the fabricated parts in addition to improving the mechanical properties such as the tensile strength and Young's modulus [66]. First laser-based additive manufacturing techniques such as selective laser sintering (SLS) employed a binding material powder mixed with the raw metal powder or pre-coat the metal powder with the binding material [67]. This binding material was usually a thermoplastic polymer. This was necessary because the laser powers used were not sufficient to melt the metal powder in addition to the poor absorptivity of the metal powder to the laser energy as compared with the polymer powder at the laser wavelength used at the time [68]. The laser would melt the binding powder or the binding coat around the metal powder thus creating the green part [69]. Then the green part would be placed in an oven to fuse the metal powder and remove the binding material. This would leave the part with low relative density due to the porosity left by the binding material. Different techniques were used to densify the part such as diffusion densification usually using infiltration [70]. This problem was

solved by using higher laser powers 200 watts up to 1 kW and sometimes up to 3kW with wavelengths more suitable for metals to absorb. Preheating the powder bed also reduced the required energy from the laser to melt and fuse the powder [71].

Currently, steels and Inconel alloys are additively manufactured with full density by optimizing the scanning speed and laser power [72–74]. It was found that high laser densities, i.e., lower scanning speed and higher laser power result in lower porosity by melting and fusing the powder better. However, if the laser density was too high bubbling could occur and cause porosity and poor surface finish [75]. Researchers studied the tensile and compression properties of 15-5 PH and IN718 in [76, 77] and [78–81], respectively. Previous work also compared traditional manufacturing properties such as casting and wrought specimens to the DMLS parts, where the DMLS samples were found to fall within standards in terms of compressive and tensile strength. In addition, the microstructure of both metals has been investigated for specimens fabricated in different orientations in the work of [46, 82, 83]. It was found that the anisotropy, is a direct result of the building orientation, which affects the tensile and compression mechanical properties. This anisotropy is inherent in most DMLS parts [84–89]. The vertically sintered specimens (Z direction) are usually inferior to the horizontally fabricated specimens. The extent of the difference in the mechanical properties of different orientations varies between different studies, which could be caused by using different processing parameters for specimen fabrication.

While the as-built parts show high tensile strength and hardness due to the rapid cooling during laser sintering, they suffer from high residual stresses [90], unmolten regions, and porosity. This causes unpredictable failures, shorter fatigue lives, and lower overall reliability. Therefore, most manufacturers recommend stress relief heat treatments. In most applications such as aerospace and automotive, the loads are primarily not static. Therefore the high and low cyclic fatigue lives of these metals have been studied taking into account building orientation and surface finishing [91–94]. Gribbin et al. [93] showed that DMLS IN718 parts lasted longer at low strain amplitudes than the wrought samples at low cycle fatigue. However, at higher strain amplitudes, the wrought samples had a longer life than the DMLS ones. The porosity and unmolten/fused powder defects in DMLS parts contribute significantly to the shorter fatigue life. Since fatigue life is affected highly by the surface condition, the DMLS specimens with surface treatment showed a longer fatigue life than as-built specimens. However, despite surface treatment, the AM metal samples resulted in shorter fatigue life than traditionally manufactured specimens. This is attributed to the subsurface defects that can initiate cracks [95].

The fatigue life of AM 15-5PH and the similar 17-4PH has been investigated. The high and low cyclic fatigue lives of these metals have been studied taking into account building orientation and surface finishing [96–99]. Researchers found that vertically fabricated specimens have a much lower fatigue life than horizontally built

ones [96]. In general, both building directions have a lower life than traditionally manufactured specimens, especially at long life cycles [100, 101]. Furthermore, the influence of different loading conditions is being investigated [102]. It was shown that the fully reversed case survived a smaller number of cycles before failure.

In most aerospace and automotive industries' applications of AM metal parts, the loading condition will not take place at room temperature. Instead, it usually occurs at elevated temperatures. IN718 is a high-temperature alloy that can preserve its high stiffness and strength for temperatures as high as 600 °C, while the 15-5 PH can handle temperatures around 300 °C [103]. However, there is no guarantee that AM parts will behave similarly to traditional manufacturing parts. In [83], the influence of environmental temperature on the tensile and yield strength of SLM IN718 was investigated and compared with forged and cast IN718 at room temperature, 450 °C and 650 °C. However, the change in microstructure and chemical composition as a result of the elevated temperatures were not investigated. No similar work was done on DMLS 15-5PH. Therefore, it is important to verify experimentally the influence of elevated temperature and fill this gap in the body of literature. One of the objectives of this study is to investigate the influence of elevated environmental temperature on the mechanical properties, and microstructure of IN718 and 15-5PH stainless steel parts fabricated by DMLS for a temperature range of up to 350 °C. The presented work also compares the microstructure and the failure pattern of the specimens with similar samples loaded at room temperature.

1.5.2 Influence of Post-Processing Heat Treatments on Additively Manufactured Parts

In literature, different heat treatments have been investigated. Some investigated stress relief heat treatments [104–107], while some investigated precipitate hardening the as-built parts [46, 96, 108]. It was shown that stress relief heat treatments reduced the residual stresses. However, this was insufficient to improve the reliability of DMLS parts. The stress relief heat treatments did not change the microstructure resulting from the laser sintering. In the work of Rafi et al. [109] as-built and solution annealed specimens were precipitate hardened, and it was found that as-built parts had reduced the precipitation due to the presence of phases other than martensite that restricts the diffusion process required for the precipitation of copper. Different precipitation or aging heat treatments were investigated in [77, 110] but the anisotropy remained and the fatigue life of AM 15-5PH remained inferior to traditionally manufactured parts. Studies showed that precipitation hardening heat treatments could increase the tensile strength and stiffness. However, it was shown that precipitation hardened DMLS specimens had a shorter fatigue life than as-built specimens due to the hardening around unmolten powder. The hardening effect causes faster crack initiation [100]. Also, some research showed that heat treatment reduced the influence of building orientation over tensile strength. However, other

research showed an increase in the anisotropy of heat-treated specimens [77, 100]. The inconsistency among the studies' results for heat-treated DMLS metal samples calls for more investigation. Furthermore, none of the literature investigated the influence of different solution annealing heat treatments for 15-5PH, which might be required to homogenize the AM parts. Therefore, one of the objectives focuses on investigating different solution treatments prior to the H900 precipitate hardening and their effect on the microstructure and mechanical properties such as Young's modulus tensile strength, ductility, and fatigue life of 15-5 PH steel fabricated using DMLS. Homogenizing DMLS parts can reduce design and manufacturing considerations [31, 87, 111] required due to the limited fabrication orientations without requiring supports or increasing the residual stresses. Thus, a part can be fabricated in the most feasible orientation without worrying about the resulting mechanical properties, which can be improved by suitable heat treatment.

Different heat treatments for IN718 have been investigated in the literature. In [112] a different aging heat treatment was investigated in which the aging was done at 700°C for 28 hours. In addition to that two different solution annealing heat treatments were investigated at 1100°C and 1200°C both for 2 hours. It was found that the modified aging resulted in similar tensile properties as the standard aging process. The modified solution annealing resulted in decreasing the tensile strength while improving the ductility. The grain size was increased due to the extended time. Similar results were found in [113] where solution annealing at 1100°C and 1250°C for 7 hours was investigated. It was shown that Laves phase and metal carbide phases did not dissolve. This disagrees with the results of [114] which claimed that the laves phase was completely dissolved at 1100 °C. Hot iso-static pressing (HIP) is investigated in [115, 116] where high pressure around 100MPa is applied during homogenization heat treatment. It was shown that the porosity size was reduced but the grain size increased which resulted in reducing the tensile strength.

1.5.3 Data-Driven Modeling in Additive Manufacturing

There are considerable efforts that aim to use machine learning algorithms to aid in improving the quality of additively manufactured parts. This is due to recent improvements in computational power and the availability of machine learning tools. Machine learning has been used considerably in manufacturing to help in recommending design features [117], cost estimation [118], topology optimization [119] and tolerancing [120]. Convolutional neural networks have been used for defect detection, and in-situ thermal analysis, and process classification, in addition to part geometry compensation [121–124]. Correlating the processing parameters to the quality of additive manufactured parts using machine learning is an increasingly common approach in published literature [17, 125]. Support Vector Machine (SVM) and artificial neural network (ANN) as main supervised machine learning approaches were used to predict the dimensional accuracy of FFF parts for different

layer thicknesses, nozzle temperatures, and infill densities [126]. ANN and genetic algorithm hybrid approaches were used to optimize the processing parameters for improving the dimensional accuracy in [127].

Artificial neural network (ANN) is one of the most dominant machine learning approaches in recent years. Its ability to use previous data to model complex systems made it practical for many applications. While a single hidden layer in ANN with a sufficient number of hidden neurons can be used to approximate any function [128], multilayer deep neural networks can improve the efficiency and reduce the computational cost [129, 130]. The adaptive nature of ANN, the ability to change its structure, activation function, and cost function make them suitable for classification and regression problems [131, 132]. ANN has been used in the manufacturing industry to optimize forming processes and predicts the properties of materials produced using different processing parameters [133]. Previous research has demonstrated the efficiency of ANN in optimizing manufacturing processes such as machining and metal forming [134]. ANN was applied to optimize the milling process for hard-to-machine materials where the cutting tool is suspect to rapid wear when subject to severe cutting conditions [135–137]. Traditional sheet metal bending and laser sheet bending were optimized using ANN by modeling the spring back [138]. Neural networks have proven useful in novel manufacturing methods where limited previous knowledge is available. A series of recent studies on additive manufacturing employed ANN to predict the porosity, surface roughness, and mechanical properties of laser or electron beam-based metal additive manufactured parts [139]. These studies often employ the design of experiments and material characterization techniques to improve the performance of the ANN by providing additional information about the process or planning the investigated values of the processing parameters for the training data [140]. The ANN model takes the processing parameters of the additive manufacturing method such as laser power, layer thickness, and scanning speed as model inputs, and using the training data, the response such as tensile strength and porosity are predicted. The training data can be obtained from tested samples prepared based on factorial design, Taguchi's orthogonal arrays, or from the available literature. Characterization techniques such as microstructure imaging, X-ray diffraction, and CT-scans are often used to support the model [141].

Hybrid modeling refers to models where part of the model can be formulated based on first principles and part of the model has to be inferred from data due to lack of understanding of the physical mechanism details [142]. The physics involving the powder bed fusion process is complex due to the high interactions between the processing parameters in addition to the complexity of the powder metallurgy. Therefore, modeling and simulating the influence of the processing parameters and post-processing heat treatments on the microstructure and mechanical properties of additively manufactured parts remains a challenge in further improving their

quality. Hybrid modeling utilizes the available knowledge to reduce the number of free parameters that need to be determined using data-driven machine learning. In [143–145] a thermal model and a Bayesian machine learning algorithm were used to predict the melt pool geometry in PBF. In [146] the inter and intra-layer bond strength and porosity in FFF parts were modeled using a hybrid approach that utilized neural networks, thermal modeling, and geometric analysis of the deposited filament. The work reported ¿94% accuracy. Kapusuzoglu et. al. [147] investigated three hybrid approaches that combine physical models and deep neural networks (DNN) to correlate the temperature profile during the FFF process to the layer bond strength and tensile strength of FFF parts. It was demonstrated that implementing physics-informed constraints significantly improves the accuracy and physical consistency of the DNN model. Thermophysical models combined with genetic algorithm were combined in [148] to simulate the influence of PBF processing parameters on the balling susceptibility of molten powder. The model was able to predict the balling susceptibility with an accuracy of 90% for 6 different alloys with only 166 data points collected from the literature.

The literature demonstrates the potential of hybrid machine learning approaches in improving the quality of additively manufactured parts with limited data by employing physics-derived models to alleviate the need for big data to simulate complex systems.

1.5.4 Objectives

Considering the literature and the state of the art of laser-based powder bed fusion, the goal of the work presented in this dissertation is to understand the influence of the DMLS process on the microstructure and mechanical properties of the as-built condition 15-5PH steel and Inconel 718 superalloy. Then develop heat treatments that aim at improving the mechanical properties and the reliability of additively manufactured parts made from these metals. Furthermore, the heat treatments aim at reducing the anisotropy in the mechanical behavior of DMLS parts and the dependency of the mechanical properties on the part's orientation during the DMLS process. This can alleviate the design consideration which may restrict the part's topology due to the limited feasible orientations the part can be fabricated in. By optimizing the heat treatment, the part can be fabricated in the most feasible orientation and then post-process heat-treated to achieve the desired mechanical properties. Finally, a hybrid model is proposed to understand the influence of solution annealing and homogenization heat treatment on the tensile strength of additively manufactured Inconel 718.

The work presented here aims at answering the following questions:

- How does the orientation of the part during the DMLS process affect the microstructure and mechanical properties of as-built 15-5PH steel and Inconel 718 parts?
- How is the mechanical behavior of DMLS 15-5PH and Inconel 718 affected at elevated environmental temperatures?
- What is the impact of post-processing heat treatments on the microstructure, mechanical properties, and anisotropy of DMLS Inconel 718 and 15-5PH parts?
- What is the influence of the temperature and duration of the homogenization and solution annealing heat treatments on the strengthening mechanisms in additively manufactured Inconel 718?

Chapter 2

METHODS

This chapter describes the experimental characterization methods used throughout this dissertation, their background, and the theory required to analyze the experimental results.

2.1 Tensile Test

The tensile test was used to characterize the mechanical behavior of the material after the additive manufacturing process. In this work, tensile testing was used to investigate Young's modulus, the yield strength, tensile strength, and ductility. These values can be extracted from the stress-strain diagram produced during the testing. Young's modulus is defined as the slope of the linear or elastic region. To obtain robust results, the slop was calculated by fitting the linear region of the stress-strain diagram. Since the material investigated in this work does not exhibit a distinct yield point, Young's modulus was calculated in a region far from the yield point. Furthermore, the yield strength as the stress level required to produce a plastic strain of 0.2%. It can be calculated by constructing a line with an offset of 0.002 in the X-axis (the strain axis) and a slop equal to Young's modulus. The 0.2% offset yield strength is equal to the Y-axis (stress axis) component of the intersection between the line and the stress-strain curve as can be seen in Figure 2.1. The tensile strength is defined as the maximum stress level in the engineering stress-strain curve. Finally, the ductility is defined as the maximum elongation percent (relative to the original length) sustained by the tested specimen before fracture. The tensile test speed was controlled by setting a constant extension rate. This is done by controlling the speed of the cross-head of the tensile testing machine. In this work, the tensile test setting was chosen based on appropriate American Society for Testing and Materials (ASTM) standards. The load was measured using a load cell installed between the moving grips and the cross-head of the tensile test machine. The strain was directly measured using an extensometer attached to the gauge length of the specimen. A Digital Image Correlation (DIC) system (described below) was also used to calculate Poisson's ratio.

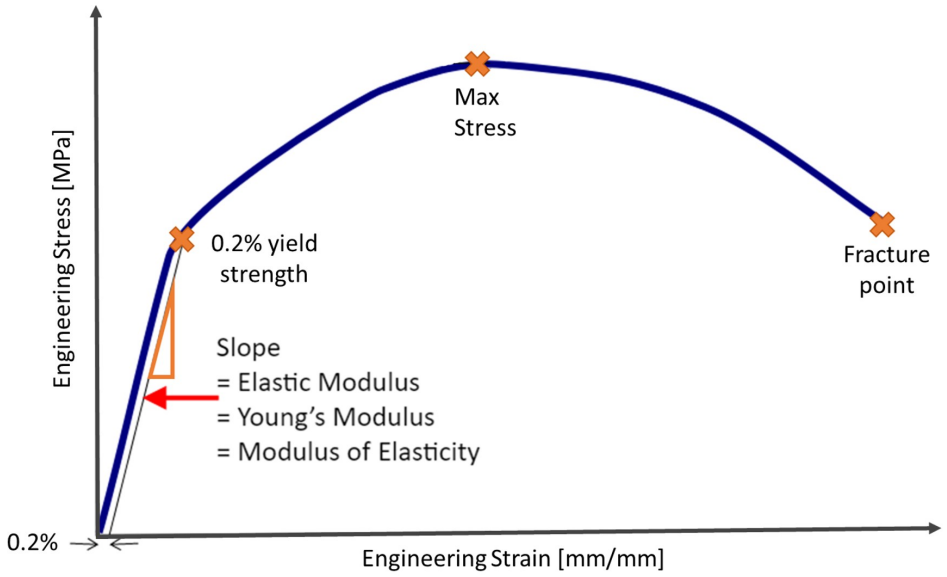

Figure 2.1: Engineering stress-strain diagram

2.2 Digital Image Correlation

Aramis Digital Image Correlation (DIC) system was used during the testing to evaluate Poisson's ratio and observe the breaking patterns and the strain fields associated with it. The DIC system used in this study consists of two digital cameras with a resolution of (2752 x 2200) pixels observing the same spot from two different angles, therefore forming a 3D surface of the tested specimens as seen can be seen in Figure 2.2. The distance and angle between the two digital cameras were set up to provide the volume of focus required based on the specimen's size and expected deformation. The specimens were painted with white and black patterns to aid the system in measuring the strains as the tensile test progresses. The DIC system took two images per second during the test. Strains in X, Y, and Z directions are measured by tracking the changes in the distances between points aligned in those directions. Multiple measurements were taken for strains associated with relatively small dimensions to reduce the effect of noise in the measurements.

2.3 Optical Microscopy

An upright-style Olympus BX51 microscope was used for the imaging using bright field mode and epi-illumination. An objective lens with 10x magnification was used for the low magnification images and a 50x objective lens for the high magnification images. The sample was illuminated by a mercury illumination system. The images were collected using the MU900 digital camera with a resolution of 3488x2616 pixels.

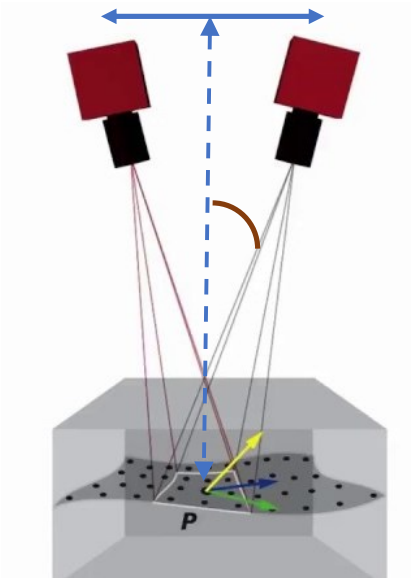

Figure 2.2: DIC system schematic

The microstructure analysis was done on regions on the specimen's grip section to avoid strain hardening effects on the microstructure. The microstructure was imaged in two planes one normal to the tensile force vector and one plane containing the tensile force vector, labeled A and B respectively, as shown in Figure 2.3. If otherwise not mentioned, the microstructure is imaged on plane A.

2.4 Scanning Electron Microsopy

Scanning electron microscopy (SEM) uses a focused electron beam to scan over the surface of a material, which gives off various signals after interacting with different depths within a specimen. The depth of interaction is known as the interaction volume. Usually, the size of the interaction volume depends on the accelerating voltage of the primary electron beam and the atomic density of the specimen. The electron beam accelerating voltage can range from as low as 0.1 kV to 30 kV, and the types of signals given off at different depths include: auger electrons, secondary electrons (SE), characteristic x-rays, back-scattered electrons (BSE), and Bremssarahung x-rays, as shown in Figure 2.4. The SEM used in the studies presented here is a field emission gun-SEM (Zeiss Gemini 500 FEG-SEM). The SEM has various detectors including an in-lens detector, secondary detector, and backscatter detector. Since the objectives of using SEM in the studies presented here are to characterize the fractured surface topography and characterize the microstructure morphology the in-lens and Everhart-Thornley secondary electron detector detectors were used. In addition, relatively low voltages were used (equal to or less than 3 kV) to avoid extensive electron beam penetration of the specimen. Operating at low

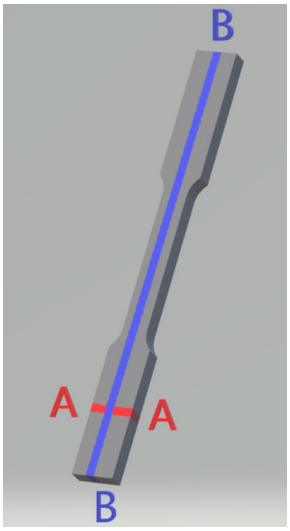

Figure 2.3: The planes on which the microstructure was investigated

voltage has the advantage of obtaining the surface signals of the material without the noise given off by electrons scattering from a larger interaction volume. In addition, operating at this low accelerating voltage also prevents the specimen from heating up and altering the microstructure. Even though the specimens were grounded using carbon tape, operating at a lower accelerating voltage prevents charge build-up on the surface of the specimen which has a negative impact on the image quality. However, operating at low voltage can lower the electron signal intensity and can affect the image quality and resolution, especially when higher magnifications are required.

2.5 X-Ray Diffraction

X-Ray Diffraction (XRD) is a material characterization technique that helps in determining the structure of a crystal. Crystalline material diffracts the incident X-rays beam into specific patterns. By measuring the angles and intensities of the diffracted beams a 3D model of the studied crystal can be produced. One of the most important accomplishments in crystallography was the idea of thinking of X-ray diffraction and scattering as reflections caused by the crystal planes. This led to the development of Bragg's law ($n\lambda = 2dsin(\theta)$). X-ray diffraction is based on constructive interference of monochromatic X-rays and a crystalline sample. These X-rays are generated by a cathode ray tube, filtered to produce monochromatic radiation, aligned, and directed toward the sample. The interaction of the incident rays with the sample produces constructive interference when conditions satisfy Bragg's Law. This law relates the wavelength of electromagnetic radiation to the diffraction

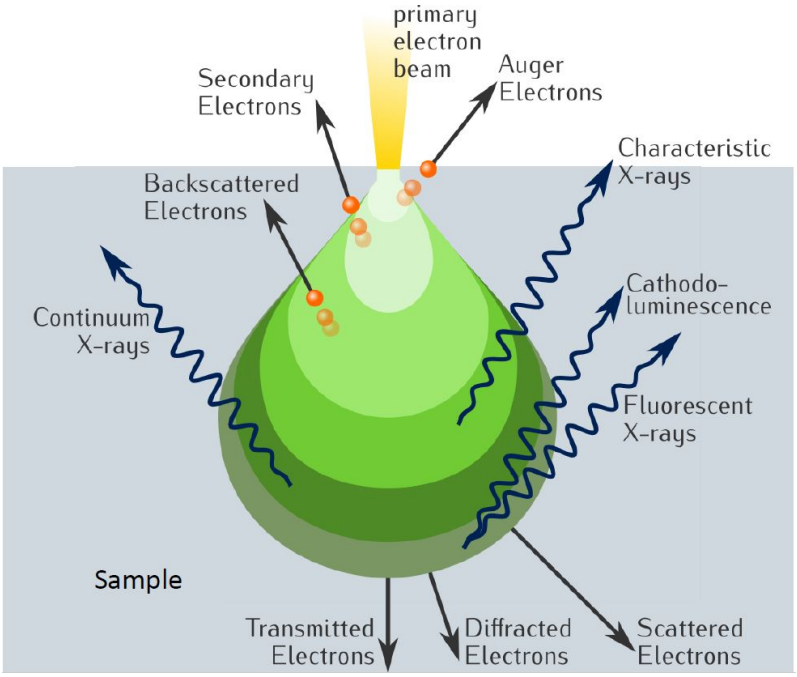

Figure 2.4: Principle of scanning electron microscopy

angle and the lattice spacing in a crystalline sample, as shown in Figure 2.5. These diffracted X-rays are then detected, processed, and counted. By scanning the sample through a range of angles, all possible diffraction directions of the lattice should be attained due to the random orientation of the powdered material. Conversion of the diffraction peaks to d-spacings allows identification of the crystal because each crystal has a set of unique d-spacings. However, as crystal structures get more complex it gets more difficult to use the d-spacings solely to determine the different phases present in a sample. Therefore, to determine the different phases present in a sample we compare the spectra with standard references or with databases such as maintained by the International Center of Diffraction Data (ICCD).

In this work, PANalytical X'Pert PRO Theta/Theta Powder X-ray Diffraction System was used to perform the XRD characterization. The system was equipped with a solid-state 3 kW X-ray generator with maximum settings of 60kV and 60mA and Cu and Co tubes. The measurements in this work were produced using the Co K(alpha) anode with a monochromatic wavelength of 0.1789 nm.

2.6 Rietveld Refinement

Rietveld refinement is a technique that involves fitting the complete experimental XRD spectrum by producing a calculated XRD spectrum from the known

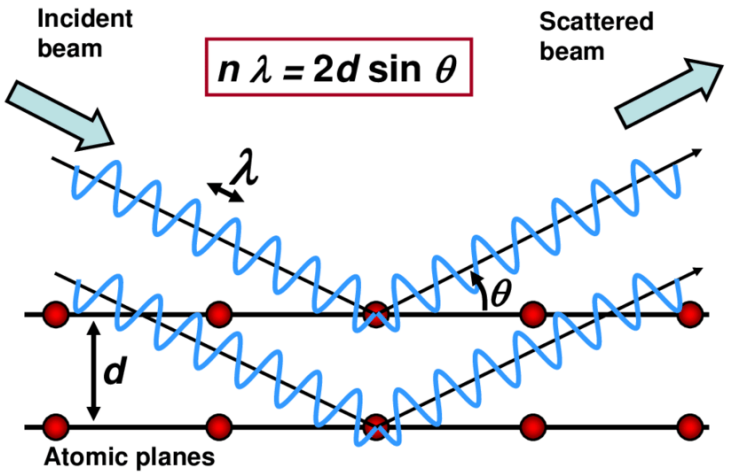

Figure 2.5: Principle of X-ray diffraction

crystal information. The term refinement refers to the adaptation of certain crystallographic parameters to minimize the square error between the experimental and calculated spectra. The method requires reasonable initial values for crystal and instrumental parameters such as the peak shape, unit cell dimensions, and coordinates of all atoms in the crystal structure. Therefore, crystal information from databases such as the ICCD are very useful when performing Retrieved refinement. The technique was used in the presented studies to perform a quantitative analysis of the phases in the studied specimens. The relative intensity ratio method was not suitable due to the presence of peak overlap between the present phases. Therefore, full spectra analysis was used to calculate the volume fraction of the phases. The initial crystal parameters were determined from crystallography open database (COD) and ICCD to start the quantitative Rietveld refinement. The fitting processes started by determining the background noise signal. The refinement protocol starts by refining the scale factor, the sample displacement, then the Caglioti coefficients W, V, and U, and finally the preferred orientation. The refinement of the lattice parameters was avoided because of the huge number of parameters required for the refinement, which will reduce the probability of convergence or produce non-physical values only to reduce the sum of squared errors between the calculated spectra and the experimentally observed spectra.

Chapter 3

CHARACTERIZATION OF AS-BUILT DMLS PARTS AT ROOM AND ELEVATED TEMPERATURES

3.1 Introduction

Additive Manufacturing (AM) started as a Rapid Prototyping (RP) technology to aid in visualizing and validating designs in the design process. However, with the recent improvements in metal AM parts, functional parts can be manufactured using laser-based AM. Currently, metal AM parts have comparable mechanical properties to traditional manufacturing parts. 15-5 PH stainless steel and Inconel 718 are two of the most commonly used metals in laser-based AM, and they have a high modulus of elasticity, corrosion resistance, and tensile strength, and can be precipitate hardened to increase their strength and hardness by aging heat treatment. These properties make 15-5 PH stainless steel and Inconel 718 suitable for many industrial applications such as aerospace and automotive. However, due to the layering nature of AM, AM parts usually suffer from anisotropy, porosity, defects, and low reliability. In this chapter, the mechanical properties such as tensile strength, modulus of elasticity, yield strength, and ductility are experimentally evaluated.

However, In most aerospace and automotive industries' applications of AM metal parts, the loading condition will not take place at room temperature. Instead, it usually occurs at elevated temperatures. IN718 is a high-temperature alloy that can preserve its high stiffness and strength for temperatures as high as 600°C, while the 15-5 PH can handle temperatures around 300°C [103]. However, there is no guarantee that the AM parts will behave similarly to the traditional manufacturing parts. In [83], the influence of environmental temperature on the tensile and yield strength of SLM IN718 was investigated and compared with forged and cast IN718 at room temperature, 450°C and 650°C. However, the change in microstructure and chemical composition as a result of the elevated temperatures were not investigated. Therefore, it is important to verify that experimentally and fill this gap in the body of literature. This chapter will investigate the influence of elevated environmental temperature on the mechanical properties, and microstructure of IN718 and 15-5PH stainless steel parts fabricated by DMLS for a temperature range of up to 350°C. The presented work also compares the microstructure and the failure pattern of the specimens with similar samples loaded at room temperature. The mechanical

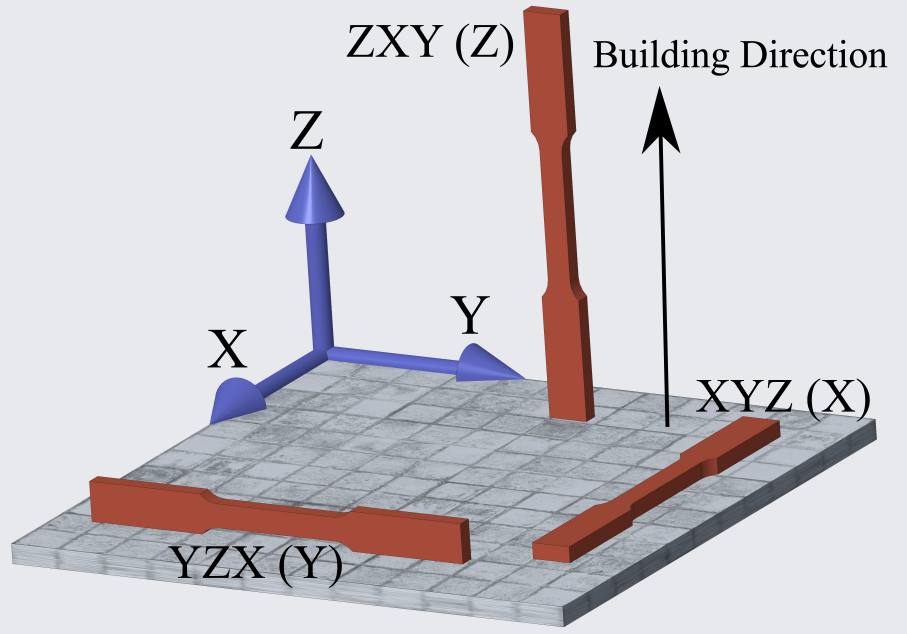

Figure 3.1: The three orientations used in fabricating the specimens

properties are evaluated using specimens fabricated in three different orientations to capture the effect on the anisotropy. In addition to that, the microstructure of the specimens is studied to investigate the influence of elevated temperature on the microstructure.

3.2 Methodology

3.2.1 Experimental plan

To investigate the influence of the elevated environmental temperatures on the mechanical properties of 15-5PH steel and IN718 parts, a total of 18 patches of specimens were fabricated, 9 patches for each metal type. Every six patches were fabricated in one of the three principal orientations XYZ, YZX, ZXY described in ASTM-F2971-13 standards [1] and abbreviated in this work as X, Y, and Z, respectively as, shown in Figure 3.1. The patches were tested at three different environmental temperatures: at room temperature, 200°C, and 350°C. For each testing chamber temperature, three orientations are tested. Table 3.1 lists the sample number, the material type, the assigned building direction, the testing chamber temperature in degree Celsius, and the number of tested specimens for each sample. The goal of the testing plane is to capture the influence of the elevated temperatures on the samples' mechanical properties, anisotropy, and microstructure. Each sample was repeatedly tested using three specimens to check for repeatability.

Table 3.1: Specifications of DMLS Samples

Sample No.	Material	Build Direction	Test Tempe	Replicas
1	15-5PH	(X)	Room temperature	3
2	15-5PH	(Y)	Room temperature	3
3	15-5PH	(Z)	Room temperature	3
4	15-5PH	(X)	200°C	3
5	15-5PH	(Y)	200°C	3
6	15-5PH	(Z)	200°C	3
7	15-5PH	(X)	350°C	3
8	15-5PH	(Y)	350°C	3
9	15-5PH	(Z)	350°C	3
10	IN718	(X)	Room temperature	3
11	IN718	(Y)	Room temperature	3
12	IN718	(Z)	Room temperature	3
13	IN718	(X)	200°C	3
14	IN718	(Y)	200°C	3
15	IN718	(Z)	200°C	3
16	IN718	(X)	350°C	3
17	IN718	(Y)	350°C	3
18	IN718	(Z)	350°C	3

3.2.2 Specimens preparation

All the 15-5PH steel specimens were fabricated on the EOSINT M 270 system using the commercialized powder PH1 from EOS, while the IN718 specimens were fabricated on the EOSINT M 280 using the commercialized powder IN718. Table 3.2 lists the weight percentage by the chemical composition of the raw powders we used for fabricating the IN718 and 15-5PH specimens. Table 3.3 lists the processing parameters used during the additive manufacturing of the specimens such as the laser power, scanning speed, hatch spacing, layer thickness, etc. The specimens were fabricated according to the ASTM-E8/E8M [149] with dimensions as shown in Figure 3.2.

Table 3.2: Raw powder chemical composition in weight percentage of the DMLS Samples

15-5PH	Cr	Ni	Cu	Mn	Si	C	Mo	Nb	Fe				
	14.0-15.5	3.5-5.5	2.5-4.5	1.00 max	1.00 max	0.07 max	0.5 max	0.15-0.45	Bal				
IN718	Ni	Cr	Nb	Mo	Ti	Al	Co	Cu	C	Si,Mn	P, S	B	Fe
	50-55	17.0-21.0	4.75-5.5	2.8-3.3	0.65-1.15	0.20-0.80	1.0 max	0.3 max	0.08 max	0.35 max	0.015 max	0.006 max	Bal

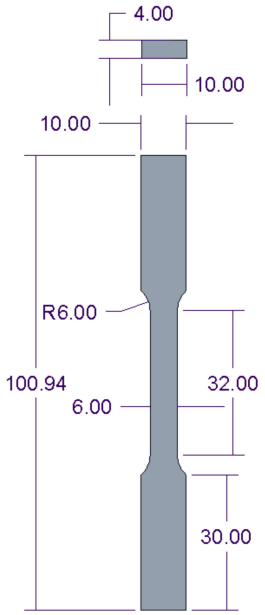

Figure 3.2: The dimensions of the fabricated specimens (all dimensions are in mm)

3.2.3 Mechanical proprieties test

To investigate the mechanical properties of the DMLS fabricated samples for 15-5PH And IN718, the authors performed tensile tests on an Instron universal testing machine 3369 with an environmental chamber with a type N thermocouple. We carried the test according to ASTM E8/E8M and E21 for axial tension tests of metallic specimens with elevated temperature. To minimize any compression caused by the thermal expansion, the tensile machine grips were closed after reaching the testing temperature. The tests started after 30 min minimum of reaching the testing temperature to ensure thermal equilibrium. The testing speed was controlled by an extension rate of 0.16 mm/min, which should maintain a strain rate of 0.005/min in the region before yield in the stress-strain diagram per the ASTM E21 standards. The data collected were time, extension, load, and the strain recorded by a high-temperature extensometer with 25 mm gauge length.

Table 3.3: DMLS processing parameters used to fabricate the samples

Metal	System	Laser Power (W)	Laser Diameter (µm)	Scan Style	Layer Thickness (µm)	Inert Gas
15-5PH	M 270	200 W	100 microns	Alternating Stripes	40 microns	N2
IN718	M 290	400 W	100 microns	Alternating Stripes	40 microns	Ar

3.2.4 Imaging analysis

Optical and Scanning Electron Microscope (SEM) images of the used powder were taken to verify the powder particle size. Also, fractography SEM images of the broken specimens' surfaces were taken to observe the presence of porosity and unmolten powder at the surface of the fracture. The microstructure analysis was done on regions on the specimen's grip section to avoid strain hardening effects on the microstructure. The specimens were cut and mounted in epoxy at room temperature to avoid further exposure to elevated temperature. The specimens were then polished with silicon carbide paper with grit 120 and increased gradually to 1200. Much care was taken not to overheat the sample so that the martensite phase does not revert to austenite [46]. Then they were polished using diamond suspensions with particles sizes 1 µm then 0.25 µm. To reveal the microstructure, different chemical etchants were used. For the 15-5PH Fry's reagents (40 ml HCL + 5 g CuCl2 + 30 ml water + 25 ml methanol) was used while for the IN718 waterless Kalling's reagent (2 g CuCl2 + 40 ml HCl + 40 ml Methanol) etchant was used. All etchants were applied by swapping for a few seconds to a few minutes and then rinsed with deionized water and isopropanol. The microstructure was imaged on two planes, plane A, which is normal to the tensile force, and plane B, which is parallel to the force as shown in Figure 2.3.

3.3 Results and Discussion

3.3.1 Mechanical Properties Test Results

The presented results of the mechanical properties are Young's modulus, the yield strength, ultimate tensile strength and the ductility or strain at fracture. The averaged results of the tests are summarized in Table 3.4. To illustrate the influence of elevated temperature on the mechanical properties of the specimens with different orientations we studied the relationship between each of the processing parameters and the resulted mechanical properties. To better illustrate the influence of the environmental temperature on the mechanical properties, Figures 3.3 and 3.4 show the relationship between the samples building orientation and the mechanical properties for samples at room temperature, abbreviated as RT, 200°C, and 350°C. Each point shown in the figures is located using the average of the three repeated samples for each testing specimen listed in Table 3.1.

Table 3.4: Mechanical properties test results for DMLS samples of 15-5PH and IN718 materials. Each row results are the average of three repeated specimens

Sample Number	Modulus [GPa]	Yield [MPa]	Yield Strain [mm/mm]	Tensile Strength [MPa]	Ductility [mm/mm]	Condition
15-5PH-1	149.65	1015.87	0.00880	1156.58	0.1638	X RT
15-5PH-2	164.68	1028.23	0.00831	1212.50	0.1414	Y RT
15-5PH-3	129.48	948.20	0.00934	1196.31	0.14080	Z RT
15-5PH-4	143.28	935.50	0.00854	1019.98	0.1190	X 200
15-5PH-5	147.40	945.40	0.00892	1074.98	0.0897	Y 200
15-5PH-6	131.05	956.85	0.00930	1035.66	0.0942	Z 200
15-5PH-7	114.15	848.25	0.00908	988.66	0.0835	X 350
15-5PH-8	144.04	869.00	0.00729	1049.77	0.0609	Y 350
15-5PH-9	113.66	892.20	0.00990	1021.52	0.0643	Z 350
IN718-10	134.61	694.77	0.00736	1007.04	0.2864	X RT
IN718-11	127.01	662.90	0.00727	1004.21	0.2792	Y RT
IN718-12	82.16	604.43	0.00941	912.63	0.3363	Z RT
IN718-13	120.70	702.82	0.00896	1016.54	0.2508	X 200
IN718-14	121.23	634.35	0.00726	968.86	0.2451	Y 200
IN718-15	90.27	539.90	0.00793	850.76	0.3143	Z 200
IN718-16	108.44	667.97	0.00820	955.15	0.2645	X 350
IN718-17	121.64	615.30	0.00695	931.03	0.2498	Y 350
IN718-18	70.03	517.935	0.00936	786.57	0.3139	Z 350

Figure 3.3a-c shows that Young's modulus, the yield strength, and the tensile strength of the 15-5PH specimens have decreased with increasing the environmental temperature during the test as expected. However, unlike traditionally fabricated steel specimens, the ductility of the 15-5PH specimens has dropped at higher temperatures as can be seen in Figure 3.3d. In addition, the results show that Young's modulus is affected by high anisotropy where the samples with Y-built orientation demonstrated the highest stiffness followed by X-built and then Z-built. The anisotropy existed at higher temperatures and slightly increased at 350°C.

The yield and tensile strength results vary around 50 MPa between the three different orientations built, where generally Z-built or Y-built orientations are usually higher than the X-built. The tensile strength of Y-built specimens showed the highest tensile strength closely followed by Z-built specimens and then the X-built specimens with strength difference close to 50 MPa at all testing temperatures

as shown in Figure 3.3b. Unlike the tensile strength where the Y-built specimens showed the highest tensile strength, in the yield strength (Figure 3.3c), Z-built specimens showed the highest strength than the Y-built specimens and X-built specimens showed the lowest yield strength. This pattern is observed at all testing temperatures except at room temperature where the Z-built specimens showed the lowest yield strength, while the Y-built specimens retained a higher yield strength than the X-built specimens. The difference in strengths can be explained by the favorable thermal history due to the smaller cross-section and smaller interlayer scanning time in the Z- and Y-built specimens compared to the X-built specimens.

The anisotropy in the ductility remained the same among all of the testing temperatures, with the X-built orientation showing a higher ductility than the Y and Z-built orientations. In addition to that, the ductility decreased with increased testing temperature as shown in Figure 3.3d, which is unlike conventionally fabricated parts.

The mechanical properties of IN718 showed a decrease as the testing temperatures increased similar to 15-5PH (see Figure 3.4). However, different anisotropy trends are observed. The X-built orientation had the highest Young's modulus value at room temperature while the Y-build samples showed the highest Young's modulus value at 350°C with the Z-built specimens showing the lowest Young's modulus at all testing temperatures as seen in Figure 3.4a. While results showed no significant effect on Young's modulus between the X and Y-builds samples as the temperature increased to 200°C. The results also showed that the Y-build orientation demonstrated a minimum change in Young's Modulus value as the testing temperature increased from room temperature to 350°C.

The results in Figure 3.4b, c showed that the tensile strength and the yield strength of IN718 showed higher anisotropy than those of 15-5PH. The difference between different orientations in yield and tensile strengths for 15-5PH was close to 50 MPa for the same testing temperature, while for IN718, the difference can reach close to 200 MPa for specimens tested at the same temperature but built in different directions. Also, the X-build orientation showed the maximum tensile and yield at all testing temperatures unlike in 15-5PH where X-built specimens showed the lowest strength.

For the ductility, the Z-built specimens demonstrated the highest value for all temperatures followed by the X-built orientation and then the Y-built orientation, See Figure 3.4(d).

3.3.2 Microstructure analysis

The microstructure analysis of 15-5PH and IN718 was done using brightfield optical microscopy. The images were taken at magnifications of 100×, 200×, 500×, and 1000×.

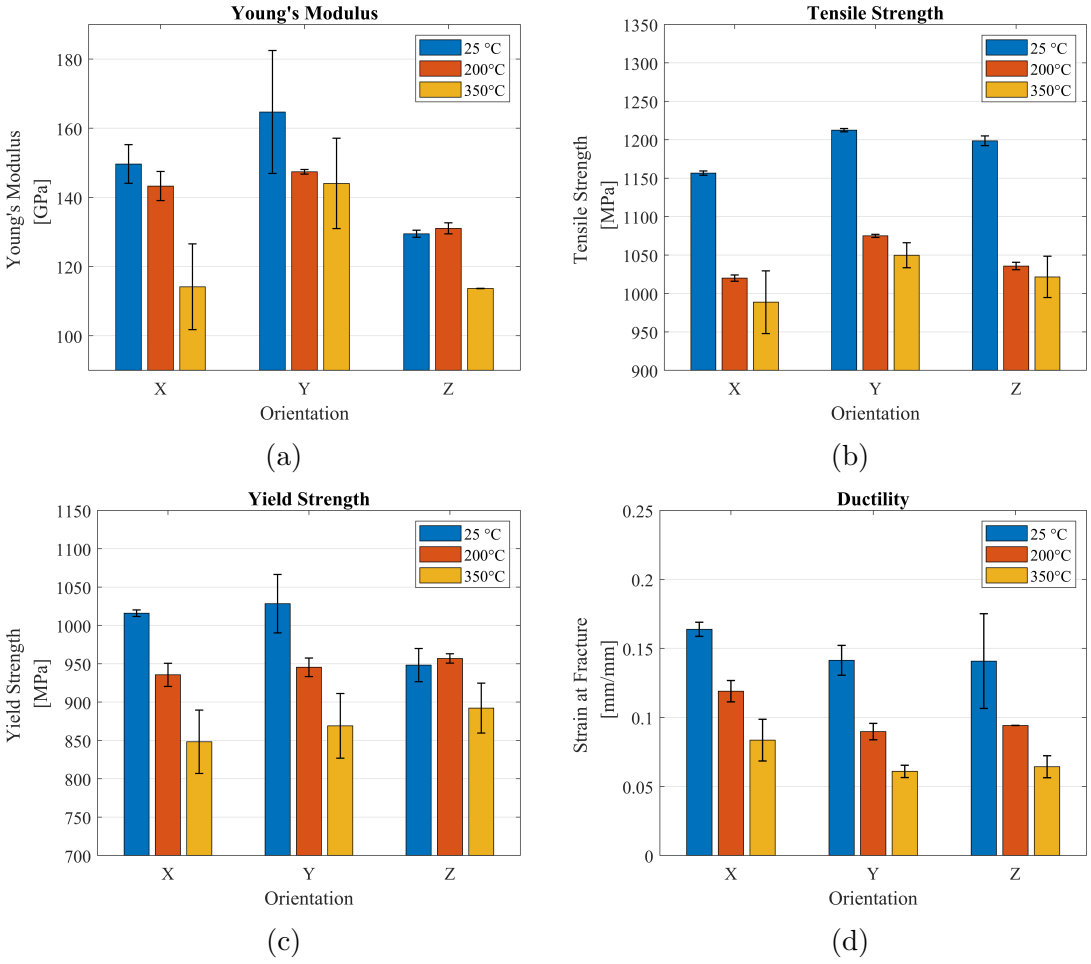

Figure 3.3: Mechanical properties of DMLS 15-5PH with different heat treatments vs building orientation.

3.3.2.1 Microstructure of 15-5PH

In the microstructure analysis for 15-5PH etched specimens, we observed the effect of the specimens' building direction layer by layer in addition to the fusing of each layer along the laser's scan lines. In Figure 3.5a, the results show a stack of layers from left to right, which shows the building direction. We can also see the cross section of the overlapping scanning lines, which were scanned in a direction out of the plane. The size of the grains at the center of a scanline is significantly larger than at the border of the scanline's cross section. This can be seen easily in Figure 3.5b at 500× magnification. By comparing panels a and b to c and d of Figure 3.5, we can see that the microstructure on plane A for both building directions X and Y shares the same pattern. However, the microstructure on plane A for building direction Z is completely different as can be seen in Figure 3.5e, f. The scan lines can

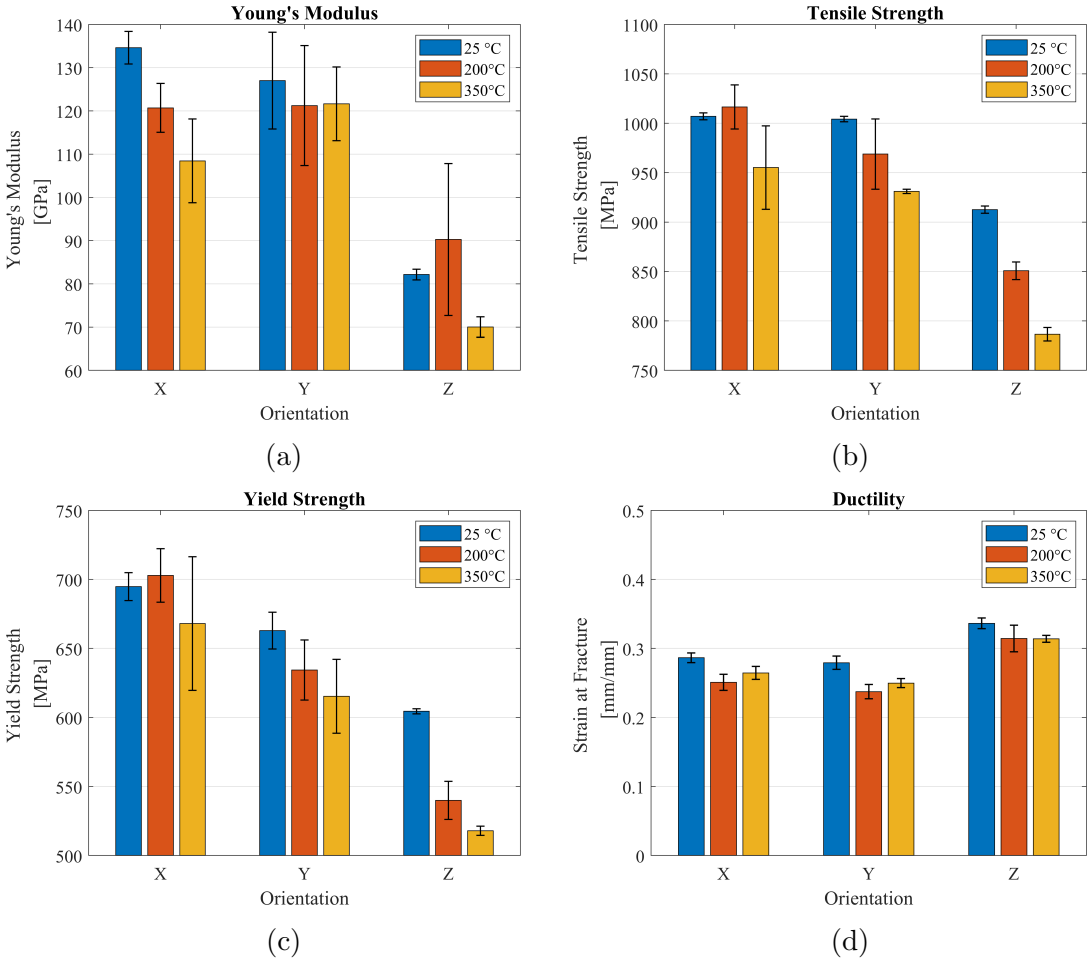

Figure 3.4: Mechanical properties of DMLS IN718 with different heat treatments vs building orientation.

be seen since they are in plane A for the building direction Z as opposed to building directions X and Y, where we can only see the cross sections of the scan lines and melting pools. The grain size at the center of the scanlines in building direction Z is slightly larger than at the borders of the scan lines making the grains size in the Z-built specimens more uniform compared to the X- and Y-built specimens. In addition, the grain size in the Z-built specimens in plane A is generally smaller than the grain sizes in X- and Y-built specimens at the center of the scan lines' cross sections.

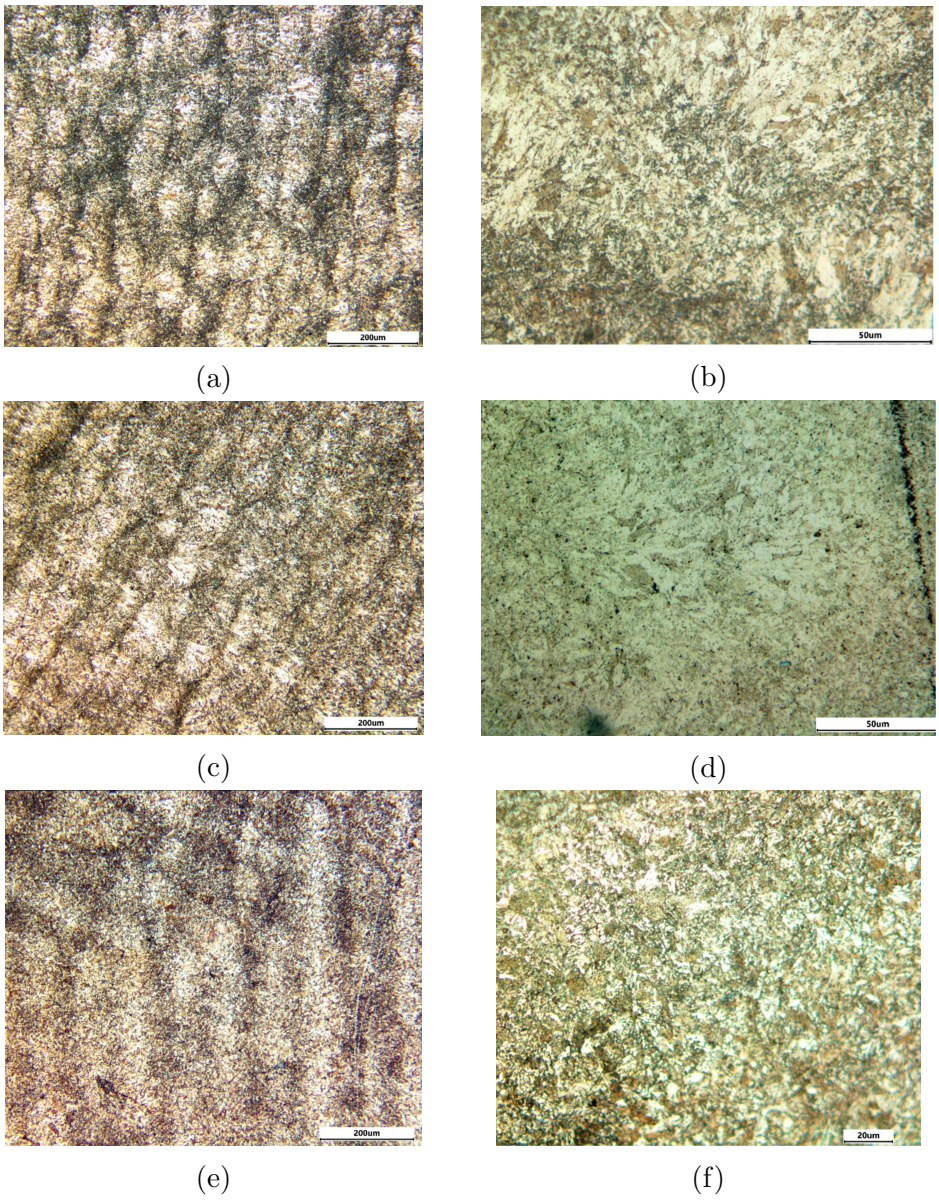

Figure 3.5: Microstructure of DMLS 15-5PH tested at room temperature imaged from plane A for different building directions. a X-building direction at ×100 magnification. b X-building direction at ×500 magnification. c Y-building direction at ×100 magnification. d Y-building direction at ×500 magnification. e Z-building direction at ×100 magnification. f Z-building direction at ×500 magnification

The micrographs of the DMLS 15-5PH tested at 350°Cshow that the specimens tested at 350°C retained there microstructure's shape and grain size as can be observed by comparing Figure 3.6a with Figure 3.5a and Figure 3.6c with Figure

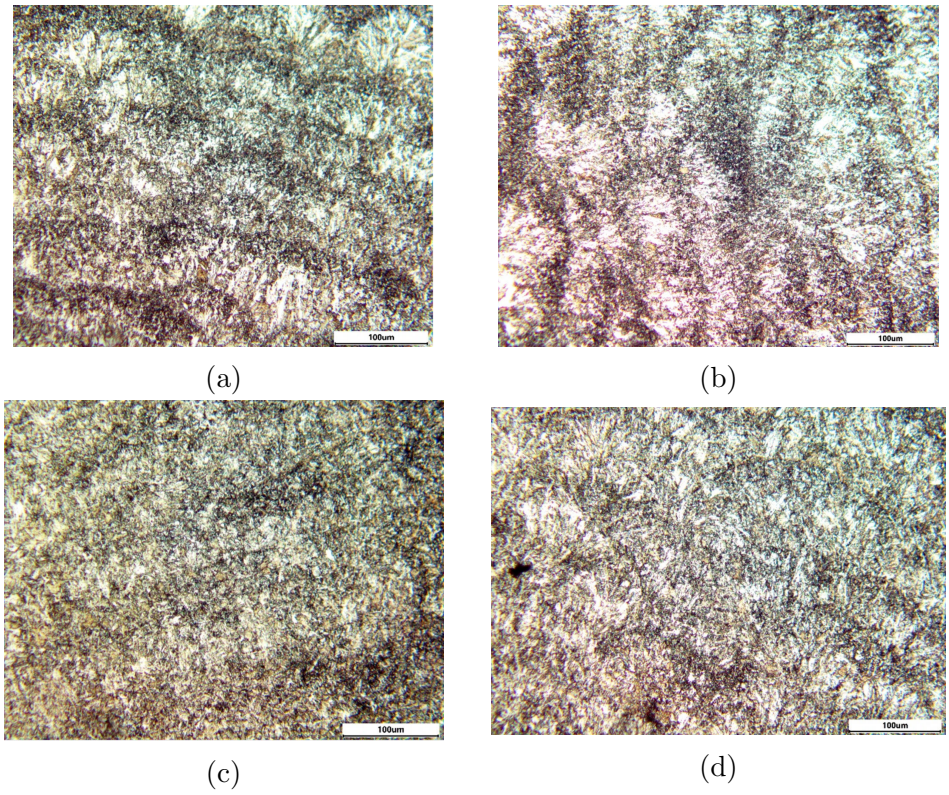

Figure 3.6: Microstructure of DMLS 15-5PH tested at 350°C. All images are taken at ×200 magnification. a X-building direction imaged on plane A. b X-building direction imaged on plane B. c Z-building direction imaged on plane A. d Z-building direction imaged on plane B

3.5e. Figure 3.6a, b shows that the microstructure on plane A for specimens printed in the X direction is similar to the microstructure on plane B. Figure 3.6c, d, however, shows that the microstructure on plane B for Z-built specimens is different than the one observed on plane A. The microstructure of plane B of the Z-built specimens is similar to the microstructure of plane A of specimens built in the X and Y directions.

The observed difference in the mechanical properties of the X- and Y-built specimens compared to the Z-built specimens can be explained by the difference in the microstructure on the planes normal to the tensile force as observed in panels a and c compared to e of Figure 3.5. The similarity in the microstructure of plane A, the plane normal to the tensile force, for X- and Y-built as seen in Figure 3.5a, b compared to Figure 3.5c, d samples, suggests similar mechanical properties for specimens printed in these directions. However, the results of the tensile tests suggest that there might be other strengthening mechanisms not observed in this

microstructure analysis that resulted in tensile test variations.

3.3.2.2 Microstructure of IN718

The optical micrographs of IN718 are represented in Figure 3.7. The cross-section of the scan lines can be clearly observed in the X- and Y-built specimens on the plane A, the plane normal to the tensile force, as shown in Figure 3.7a-d. In Z-built specimens, we can see the scan lines as shown in Figure 3.7e, f. The micrographs of the X- and Y-building specimens show that plane A is full of the dendritic microstructure. In Figure 3.7b-d, we can see that this dendritic microstructure has grown in patches pointing in different directions in different scan line cross-sections. Some scan lines' cross sections have more than one patch, each grown in a different direction. However, for Z-built specimens, the dendritic microstructure is observed to have much lower density and smaller size, as can be seen in Figure 3.7f, compared to specimens built in the X and Y directions. This could be due to the dendritic microstructure growing out of plane A for specimens built in the Z direction.

Figure 3.8 shows that the microstructure of the specimens tested at 350°C is similar to the ones tested at room temperature in both shape and grain size. The X-built specimens imaged on plane B, shown in Figure 3.8b, indicate that the microstructure of the specimens built in the X direction has similar microstructure in planes A and B. However, the Z-built specimens imaged on plane B, shown in Figure 3.8d, show that the microstructure of specimens built in the Z direction has a different microstructure in plane B compared to plane A. The microstructure observed in plane B of Z-building direction specimens is similar to planes A and B of specimens printed in X- and Y-building directions with similar dendritic microstructure.

Like the 15-5PH, the difference in the microstructure normal to the tensile force explains the different mechanical properties between the Z direction and the X and Y directions. However, since the microstructure on plane A, which is perpendicular to the tensile force as indicated in Figure 2.3, for both the X- and Y-building directions are similar, this suggests that there are different mechanisms that affect the strength of the DMLS specimens other than the shape and size of the grains.

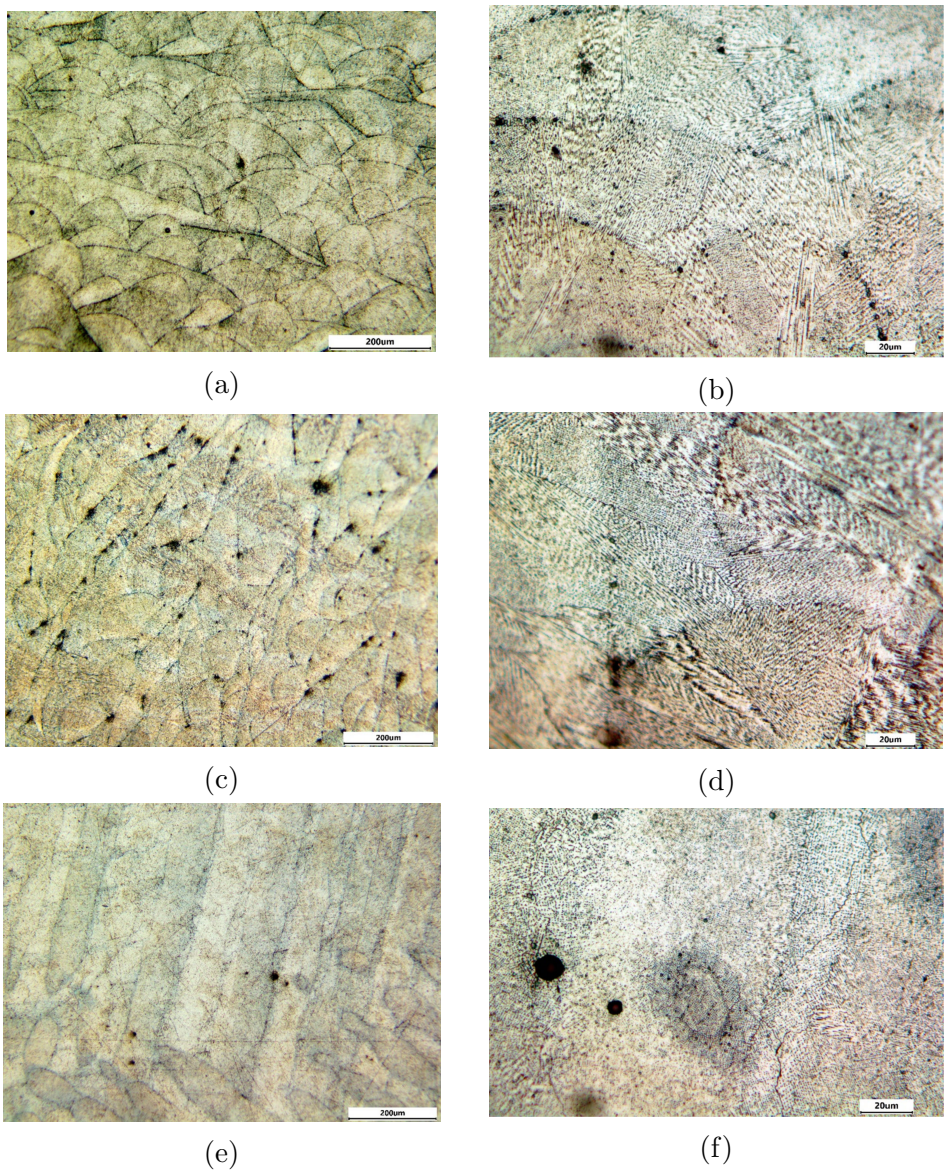

Figure 3.7: Microstructure of DMLS IN718 tested at room temperature imaged from plane A for different building directions. a X-building direction at ×100 magnification. b X-building direction at ×500 magnification. c Y-building direction at ×100 magnification. d Y-building direction at ×500 magnification. e Z-building direction at ×100 magnification. f Z-building direction at ×500 magnification

3.3.2.3 DMLS Powder SEM micrographs

The SEM micrographs of the powder show that the powders of both 15-5PH and IN718 have, generally, a spherical shape, with few deformed particles. The

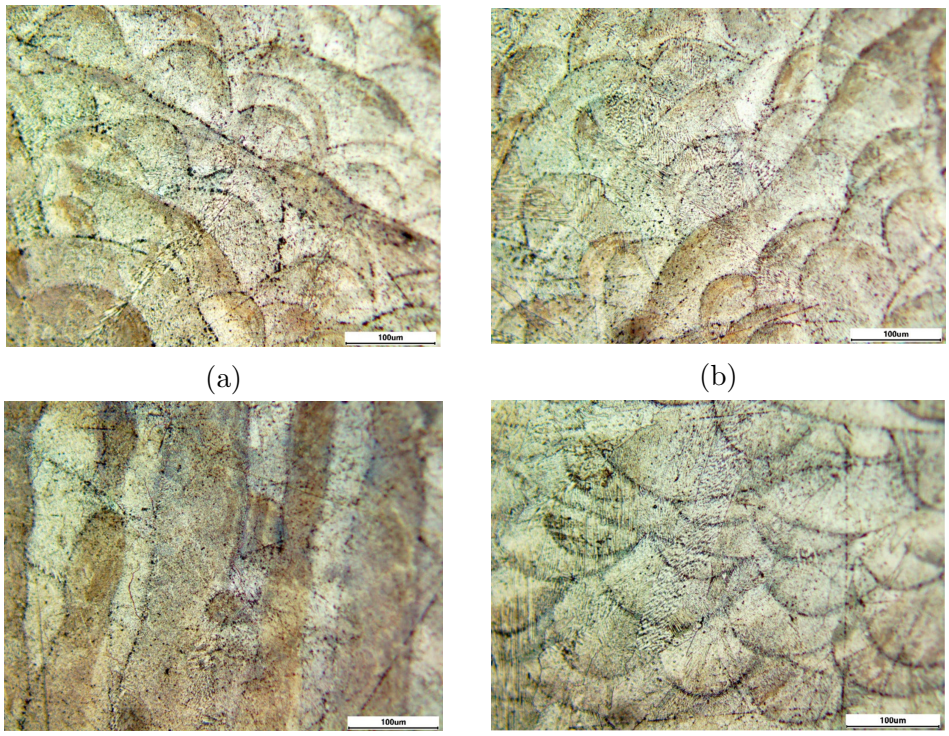

(a) (b)

(c) (d)

Figure 3.8: Microstructure of DMLS IN718 tested at 350°C. All images are taken at ×200 magnification. a X-building direction imaged on plane A. b X-building direction imaged on plane B. c Z-building direction imaged on plane A. d Z-building direction imaged on plane B

particles have a range of diameters up to 60 µm, as can be seen in Figures 3.9 and 3.10. This confirms to the data-sheets from the vendor [150,151]. The range in sizes of the powder particles aids in reducing the gaps between the powder particles, which in turn reduces the porosity in the produced parts. This is apparent in the high tensile testing mechanical properties as a result of the nearly full relative density as compared to traditionally manufactured parts.

3.3.2.4 Fractography

The fractured surfaces of the 15-5PH specimens built in the X and Y directions have similar fracture surfaces to the fracture surfaces of the specimens built in the Z directions as can be seen in Figure 3.11a, c. The similarity can be observed better at 20k× magnification as in Figure 3.11b, d. In addition to that, the fracture surface of the specimens tested at room temperature is similar to the specimens tested at 350°C as observed in Figure 3.11e, f. Similarly, from Figure 3.12, it can

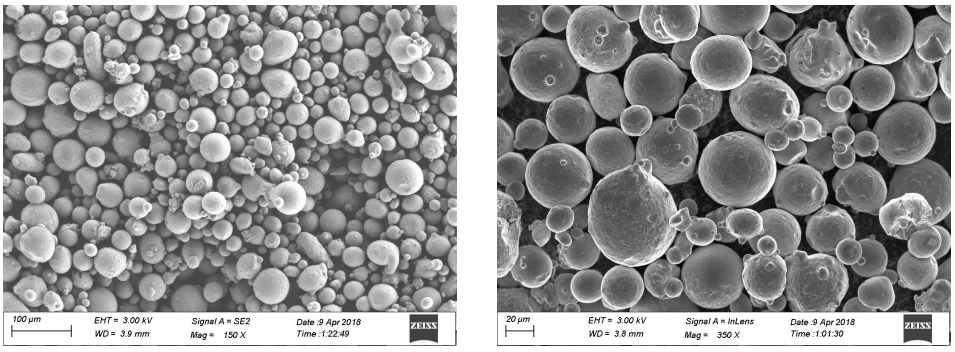

(a) (b)

Figure 3.9: SEM micrographs of 15-5PH powder. a ×150 magnification. b ×350 magnification

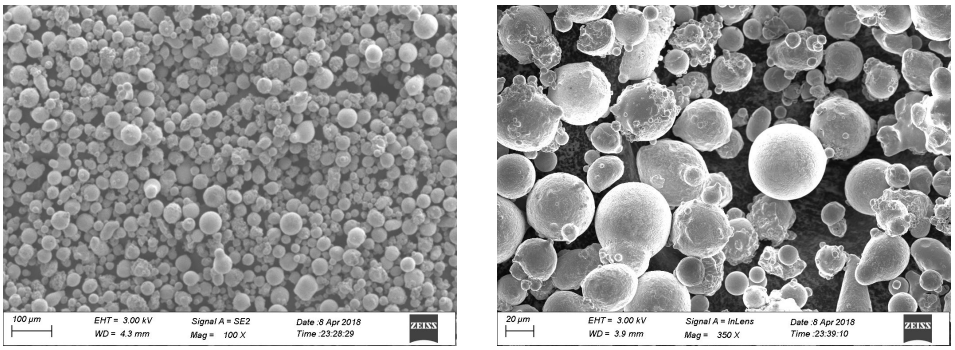

(a) (b)

Figure 3.10: SEM micrographs of IN718 powder. a ×100 magnification. b ×350 magnification

be seen that IN718 specimens built in the X and Y directions have similar fractured surfaces to Z-built specimens. However, in IN718 the topography is more prominent for Z-built specimens than for X- and Y-built specimens, while in 15-5PH the topography is more prominent for X-built specimens compared to Y-built specimens or Z-built specimens, which have the least prominent features in 15-5PH as can be seen in panel b compared to panels d and e of Figure 3.11. This can be explained by the different strains suffered before fracture. The ductility of the X-building direction specimens of the 15-5PH material is larger among the three building directions, while the samples with the Z-direction showed the lowest ductility. Refer to Figures 3.3d and 3.4d.

On the other hand, for IN718 specimens, the results showed that the samples with Z-build direction had the greatest ductility in all of the three building orientations.While the samples with Y-build directions showed a slightly less ductility than

the X- build direction specimens as observed in panel f compared to panels b and d of Figure 3.12. Refer to Figure 3.4d for the strain values.

Although the fractured surfaces of the specimens show nearly full relative density, there are locations in the specimens with observable porosities. Some of these locations are easily observed in Figures 3.11e and 3.12a, c, which are circled. These porosities did not have a significant impact on the tested mechanical properties but will significantly impact the fatigue life.

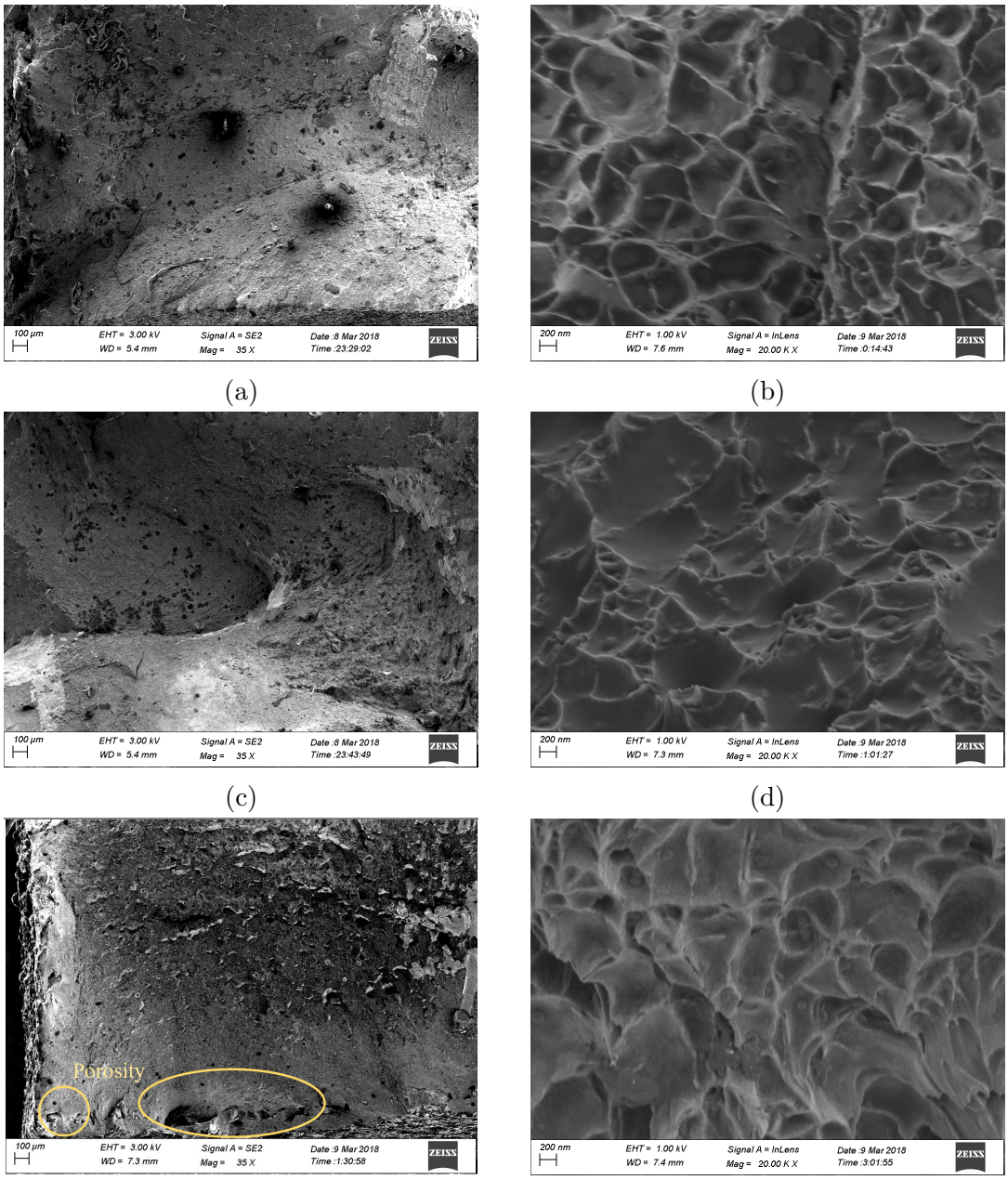

Figure 3.11: SEM fractography of 15-5PH. a X-building direction tested at room temperature ×35 magnification. b X-building direction tested at room temperature ×20k magnification. c Z-building direction tested at room temperature ×35 magnification. d Z-building direction tested at room temperature ×20k magnification. e Z-building direction tested 350°C ×35 magnification. f Z-building direction tested at 350°C ×20k magnification

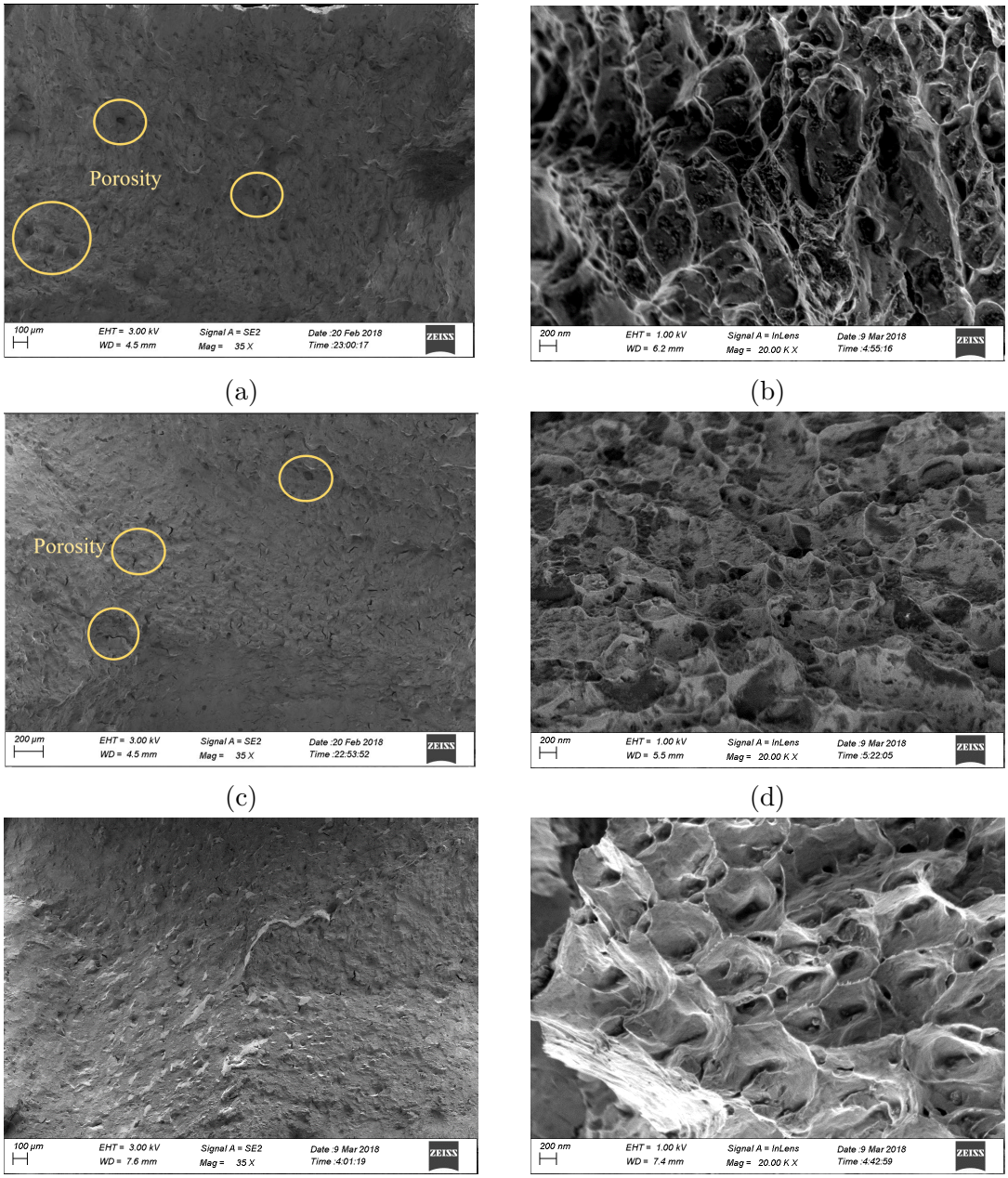

Figure 3.12: SEM fractography of IN718. a X-building direction tested at room temperature ×35 magnification. b X-building direction tested at room temperature ×20k magnification. c Z-building direction tested at room temperature ×35 magnification. d Z-building direction tested at room temperature ×20k magnification. e Z-building direction tested 350°C ×35 magnification. f Z-building direction tested at 350°C ×20k magnification

3.4 Coclusions

This study has investigated the influence of elevated environmental temperatures on the tensile test mechanical properties of 15-5PH and IN718 fabricated using DMLS in three different orientations to observe changes in the inherent anisotropy of additive manufacturing. Based on the results, this study concludes that 15-5PH and IN718 produced using DMLS can be used in applications with elevated environmental temperatures, as there was no observable permeant change in the microstructure. Reduction in the tensile mechanical properties is to be expected. However, these applications should not be sensitive to sudden failures because 15-5PH and IN718 DMLS parts have shown reduced ductility with elevated temperatures which reduce the ability to predict failure. The observed anisotropy at elevated temperatures up to 350°C shows that heat treatments geared toward reducing the anisotropy should be done at higher temperatures. This agrees with the results of [100, 110][41], [67], where aging the specimens at temperatures up to 482°C for longer periods than standard heat treatments did not reduce the anisotropy and if done without annealing at 1038 °C, precipitation hardening was not successful, which was related to slow diffusion. Finally, the difference in the microstructure between Z-building direction and X and Y directions explains the difference in the mechanical behavior of vertical and horizontal specimens. However, the difference between the tensile strength and Young's modulus of the X and Y-building directions regardless of the similarity of the microstructure on the plane perpendicular to the tensile force suggests that there are other strengthening mechanisms present causing the difference, which invokes further investigation.

Chapter 4

MICROSTRUCTURE AND MECHANICAL PROPERTIES OF HEAT TREATED 15-5PH DMLS PARTS

4.1 Introduction

15-5PH parts fabricated using direct metal laser sintering (DMLS) have shown mechanical properties comparable to conventionally manufactured parts. However, DMLS fabricated 15-5PH parts have shown high anisotropy in their mechanical properties due to the layering nature of additive manufacturing. In addition, the fatigue life and strength of DMLS 15-5PH varies significantly between horizontally and vertically fabricated parts and both orientations are inferior to conventionally manufactured parts. Reliability and large variations in performance remain as a barrier from employing 15-5PH parts fabricated using DMLS. Standard heat treatment of 15-5PH was shown insufficient to eliminate the anisotropy and homogenize the DMLS parts. Modified precipitation hardening heat treatments did not show further improvement.

The differences between the microstructure observed on the planes parallel to the layer plane and the planes transverse to the layer plane remained after standard heat treatment and the modified precipitation hardening heat treatments.

Therefore, this work focuses on investigating different solution treatments prior to the H900 precipitate hardening and their effect on the mechanical and microstructure of 15-5 PH steel fabricated using AM. Furthermore, this work utilizes Digital Image Correlation (DIC) to capture real-time strain fields instead of only two-point strain provided by standard extensometers. This gives the ability to detect localized strains which enables a better understanding of the failure modes and enables the prediction of the regions of failure. In addition, DIC makes it possible to measure strains for different directions and on different planes when used to generate a 3D surface of the specimens. This enables the measurement of Poisson's ratio for different directions.

Homogenizing AM parts can reduce design and manufacturing considerations [87, 111] required due to the limited fabrication orientations without requiring supports or increasing the residual stresses. Thus, a part can be fabricated in the most feasible orientation without worrying about the resulting mechanical properties, which can be improved by suitable heat treatment.

4.2 Methodology

4.2.1 Experimental plan

To investigate the influence of the different solution annealing heat treatments on the mechanical properties of DMLS 15-5PH steel, a total of 12 patches of specimens were fabricated. Each patch contained three specimens to check the repeatability. Every four patches were fabricated in one of the three principal orientations XYZ, YZX, ZXY as described in the ASTM-F2971-13 standards [1] and abbreviated in this work as X, Y, and Z, respectively. Building orientations are shown in Figure 4.1. Three patches, one X, one Y, and one Z, were tested in as-built condition and called HT0 in this work. The rest of the patches were subjected to different solution annealing conditions and then precipitate-hardened using the same aging heat treatment. Table 4.1 lists the patch number, the building direction, the heat treatments, and the number of tested specimens for each patch. The first investigated solution treatment is the standard solution annealing for 15-5PH which is done at 1038°C ± 14°C for one hour then air cooling. This heat treatment is called HT1 in this work and referred to as Condition A in the industry. The second solution annealing heat treatment investigated had the same temperature as the standard with the duration extended to three hours instead of one and this heat treatment is called HT2 in this paper. The third heat treatment included heating the specimens up to 1200 °C, which is in the range recommended for forging 15-5PH parts then furnace cooled before solution annealing using the standard solution annealing method. This heat treatment is called HT3. All of these heat treatments were then followed by standard H900 aging heat treatment, which is done at 482 °C, for 1.5 hours and then air cooling. The goal of the testing plan is to capture the influence of the different solution annealing treatments on the samples' mechanical properties, anisotropy, and microstructure in a structural method that relates the material type, the building direction, the mechanical properties and the microstructure with specific heat treatment.

4.2.2 Specimens preparation

All the 15-5PH steel specimens were fabricated on EOSINT M 270 system using the commercialized powder PH1 from EOS, Table 4.2 lists the weight percentage by the chemical composition of the raw powders we used for fabricating the DMLS 15-5PH specimens. Table 4.3 lists the processing parameters used during the additive manufacturing of the specimens such as the laser power, scanning speed, hatch spacing, layer thickness, etc. The specimens were fabricated according to the ASTM-E8/E8M [149] with dimensions as shown in Figure 4.2. For each tested heat treatment and fabrication direction, three specimen replicas were tested to check for results' repeatability.

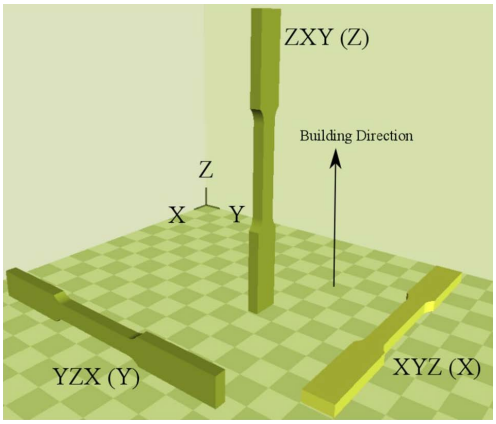

Figure 4.1: The three orientations used in fabricating the specimens

Table 4.1: 15-5PH samples and heat treatment specifications

Patch No.	Heat Treatment	Build Direction	Heat Treatment label	Replicas
1	As-built	(X)	HT0 X	3
2	As-built	(Y)	HT0 Y	3
3	As-built	(Z)	HT0 Z	3
4	1038 C for 1 hr then air-cooled (Condition A) + H900 for 1.5 hr and air-cooled	(X)	HT1 X	3
5	1038 C for 1 hr then air-cooled (Condition A) + H900 for 1.5 hr and air-cooled	(Y)	HT1 Y	3
6	1038 C for 1 hr then air-cooled (Condition A) + H900 for 1.5 hr and air-cooled	(Z)	HT1 Z	3
7	1038 C for 3 hrs then air-cooled + H900 for 1.5 hr and air-cooled	(X)	HT2 X	3
8	1038 C for 3 hrs then air-cooled + H900 for 1.5 hr and air-cooled	(Y)	HT2 Y	3
9	1038 C for 3 hrs then air-cooled + H900 for 1.5 hr and air-cooled	(Z)	HT2 Z	3
10	1200 C for 1.5 hrs then Furnace-cooled + Cond A + H900	(X)	HT3 X	3
11	1200 C for 1.5 hrs then Furnace-cooled + Cond A + H900	(Y)	HT3 Y	3
12	1200 C for 1.5 hrs then Furnace-cooled + Cond A + H900	(Z)	HT3 Z	3

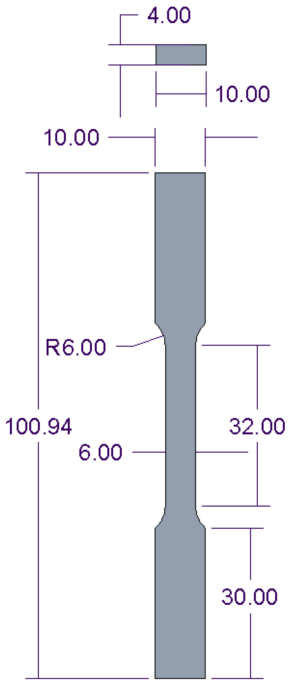

Figure 4.2: The dimensions of the fabricated specimens (all dimensions are in mm)

Table 4.2: Raw powder chemical composition in weight percentage of the 15-5PH DMLS Samples

15-5PH	Cr	Ni	Cu	Mn	Si	C	Mo	Nb	Fe
	14.0-15.5	3.5-5.5	2.5-4.5	1.00 max	1.00 max	0.07 max	0.5 max	0.15-0.45	Bal

Table 4.3: DMLS processing parameters used to fabricate the 15-5PH samples

Metal	System	Laser Power	Laser Diameter	Scan Style	Layer Thickness	Inert Gas
15-5PH	M 270	200 W	100 microns	Alternating Stripes	40 microns	N2

4.2.3 Mechanical proprieties test

To evaluate the mechanical properties of the DMLS fabricated samples of 15-5PH steel, the authors performed tensile tests on the heat-treated and as-built specimens using an Instron universal testing machine 3369. We carried the test according to ASTM E8/E8M for axial tension tests of metallic specimens. The testing

speed was controlled by an extension rate of 0.48 mm/min, which should maintain a strain rate of 0.015/min in the region before yield in the stress-strain diagram per the ASTM E8/E8M standard. The data collected were time, extension, load, and the strain recorded by an extensometer with 25 mm gauge length. In addition to that, a DIC system was used during the testing to evaluate Poisson's ratio and observe the breaking patterns and the strain fields associated with it. The DIC system used in this study consists of two digital cameras with a resolution of (2752 x 2200) pixels observing the same spot from two different angles, therefore forming a 3D surface of the tested specimens as seen can be seen in Figure 4.3. The specimens were painted with white and black patterns to aid the system in measuring the strains as the tensile test progresses. The DIC system took two images per second during the test. Strains in X, Y, and Z directions are measured by tracking the changes in the distances between points aligned in those directions. Distances 1 and 2 are aligned in the X direction, distance 3 in the Y direction and distances 4 and 5 in the Z direction. Two distances are assigned for the X and Z directions to improve the quality of the measurements in these directions due to the smaller dimensions associated with these directions as can be seen in Figure 4.3. The specimen's dimensions were measured before and after the heat treatments. Although the changes in the cross-sectional area's width and thickness were negligible, the measured values after the heat treatment were used for calculating the mechanical properties. It should be noted that while the transformation from Austinite to Martensite usually results in expansion [152], in this study, there was a slight shrinkage that can be seen in the change of the overall length of the specimens in Figure 4.4. As Figure 4.4 illustrates, most heat treatments yielded a negative length change which means the length after the heat treatment was less than before the heat treatment. Since the HT0 specimens were tested in the as-built condition, there is no length change. For HT1, HT2 and HT3 there was a 0.05 mm to 0.15 mm of shrinkage. Since the original average length of the specimens was 101.0 mm this translates to 0.05% - 0.15% shrinkage. This shrinkage can be explained by the reduction of porosity and unmolten regions.

4.2.4 Imaging analysis

Scanning Electron Microscopy (SEM) was used to take fractography images of the broken specimens' surfaces to observe the fracture behavior and the presence of porosity and unmolten powder at the surface of the fracture. The SEM images were taken using a field emission gun SEM-Gemini 500, with Everhart Thornley secondary electron detector, an acceleration voltage of 3.0 kV for the low magnification images and 1.0 kV for high magnification images with working distances ranging between 2.4-8.0 mm.

Optical microscopy images of the microstructures were taken, as well. The microstructure analysis was done on regions on the specimen's grip section to avoid

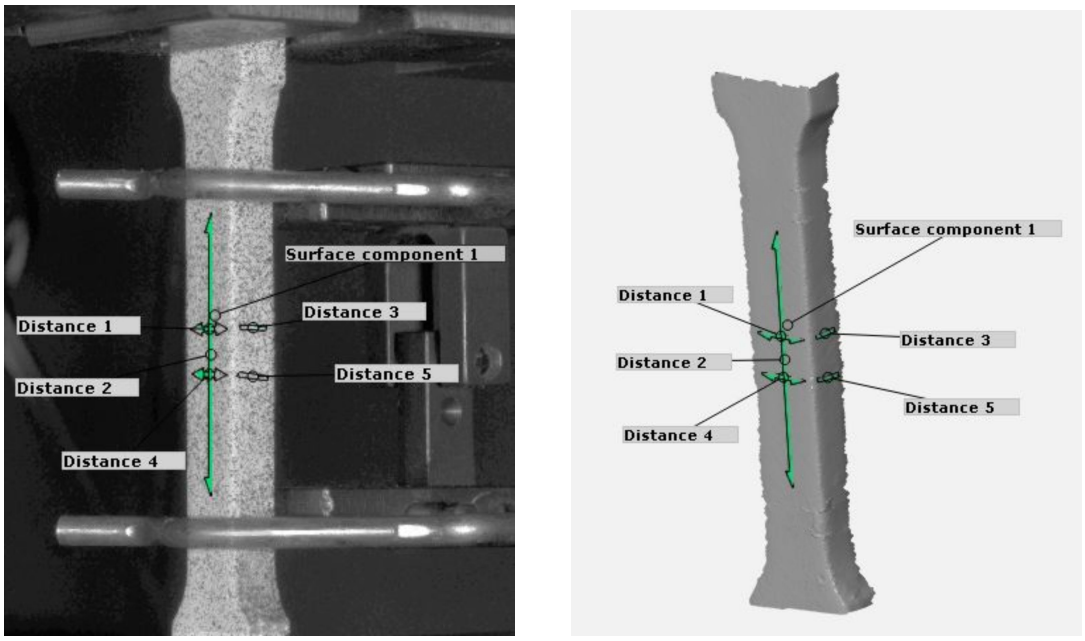

(a) (b)

Figure 4.3: The generated 3D surface using DIC for the tensile specimens. The left image showing the surface imposed on the image of the specimen, while the right image showing the surface by itself.

strain hardening effects on the microstructure. The specimens were cut and mounted in epoxy at room temperature to avoid further exposure to elevated temperature. The specimens were then polished with silicon carbide paper with grit 120 then gradually increased to 1200. Much care was taken not to overheat the samples so that the martensite phase does not revert to austenite [46]. Then, the samples were polished using diamond suspensions with particles sizes 1 micron followed by 0.25 microns.

To reveal the samples' microstructure, Fry's reagents (40 ml HCL + 5 g CuCl2 + 30 ml water + 25 ml methanol) was used. The etchant was applied by swapping for a few seconds to a few minutes and then rinsed with deionized water and isopropanol. The microstructure was imaged on the plane that is normal to the tensile force. An upright -style Olympus BX51 microscope was used for the imaging using bright field mode and epi-illumination. An objective lens with 10x magnification was used for the low magnification images and 50x objective lens for the high magnification images. The sample was illuminated by a mercury illumination system. The images were collected using the MU900 digital camera with a resolution of 3488x2616 pixels.

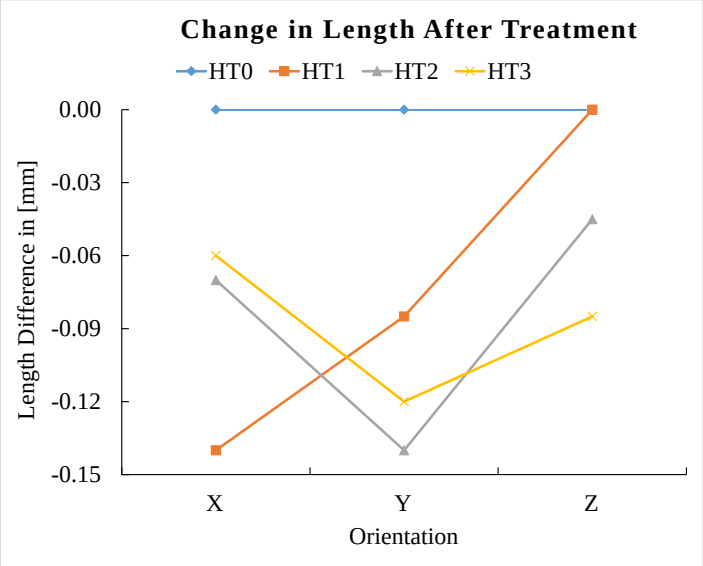

Figure 4.4: Change in the length of the heat-treated specimens after the heat treatments. Negative values signify shrinkage.

4.3 Results and Discussion

4.3.1 Mechanical Properties Test Results

The presented results of the mechanical properties are Young's modulus, the yield strength, ultimate tensile strength and the ductility or strain at fracture in addition to Poisson's ratio. The results of the tests are listed in Table 4.4. These properties were calculated according to each specimens' dimensions after the heat treatments to avoid artifacts caused by dimensional errors of the AM specimens. Figure 4.5 illustrates the influence of the different solution annealing heat treatments on the mechanical properties of DMLS specimens with respect to different fabrication orientations. Each point showed on the figures is located using the average of the three repeated specimens for each testing patch listed in Table 4.1.

Figure 4.5 shows that Young's modulus, the yield strength, the tensile strength, and the ductility of the 15-5PH specimens are highly affected by the heat treatments. Generally, all the mechanical properties increased after the solution annealing and H900 precipitation hardening except for the ductility. This effect is expected of the H900 precipitation hardening, which is supposed to increase the hardness, yield and tensile strengths on the expense of reducing the metal's ductility [110]. Looking at Figure 4.5(a), we can see that all the solution heat treatments resulted in a significant increase in Young's modulus for all orientations except Y-built specimens

which already had a high Young's modulus. HT1 resulted in the highest modulus in the X-built specimens but in the Y and Z-built specimens, HT2 and HT3 had close values or even higher with HT2 having the least variations across all building directions. The as-built Young's modulus results agree with literature showing that horizontally fabricated specimens had larger Young's modulus than vertically fabricated specimens [153].

The yield strength of the as-built specimens (HT0) showed high dependency on the fabrication orientation with the X-built specimens showing the highest yield strength followed by the Y-built and the Z-built specimens showing the lowest yield strength this disagrees with [153] which found that the yield strength of 15-5PH does not depend on orientation. The yield strength increased significantly after the heat treatments. The increase was comparable for all heat treatments with the exception of HT3 for the Z-built specimens, which all failed unpredictably before reaching the yield point. The increase in the yield strength was at least over 100 MPa in the case of X-built specimens and over 300 MPa for the Z-built specimens, which had the lowest yield strength for the as-built (HT0) specimens which agrees with the results of Sarkar et al. [101]. HT2 had the highest yield strength across all the building directions slightly higher than HT1 and HT3 with very low variations depending on the building direction as can be seen in Figure 4.5(b). Similarly, the tensile strength increased after the heat treatments except for the HT3 Z-built specimens which had lower tensile strength than the as-built specimens as can be seen in Figure 4.5(c). Both HT1 and HT2 had comparable strengths for all building directions with very low variations depending on the building direction with HT2 being slightly higher for the X and Z-built specimens. The tensile strength of vertically fabricated specimen having higher tensile and yield strength than horizontally fabricated specimens when heat treated using the standard heat treatment HT1 agrees with the results of Lum et al [77].

The ductility of the heat-treated specimens was significantly lower than the as-built specimens (HT0) as can be seen in Figure 4.5(d). This is expected from specimens that were precipitate-hardened using H900 heat treatment. The Z-built specimens had higher ductility than the Y-built specimens and slightly higher than the X-built specimens. This agrees with the findings of [154] where the ductility of vertically fabricated specimens was higher than horizontally fabricated specimens. HT3 has resulted in the biggest reduction in ductility. HT1 had the highest ductility among the heat treatments with strains ranging between 6-8% at fracture, while HT2 had strains ranging between 2-5% at fracture compared to at least 13% strain at fracture for the as-built specimens. The ductility of solution annealed then H900

Table 4.4: Mechanical properties test results for DMLS samples of IN718 materials. Each row results are the average of three repeated specimens

Patch Number	Condition / orientation	Modulus [GPa]	Yield [MPa]	Tensile Strength [MPa]	Ductility [mm/mm]	Vxy	Vzy
1_A	HT0 X	185.45	1038.12	1181.04	0.16709	0.2257	0.4333
1_B	HT0 X	173.24	1015.03	1148.30	0.15987	0.2553	0.3241
1_C	HT0 X	180.35	1020.98	1156.87	0.16344	0.2561	0.3512
2_A	HT0 Y	195.51	1006.52	1173.68	0.13831	0.1885	0.2608
2_B	HT0 Y	198.76	966.40	1153.82	0.12962	0.2017	0.2855
2_C	HT0 Y	198.13	982.91	1160.56	0.13401	0.2217	0.2915
3_A	HT0 Z	174.86	879.98	1179.77	0.157591	0.3433	0.334
3_B	HT0 Z	138.26	874.62	1149.58	0.17510	0.2914	0.2815
2_C	HT0 Z	155.56	873.14	1159.42	0.16641	0.3159	0.3342
4_A	HT1 X	239.52	1139.02	1275.91	0.05380	0.3246	0.3523
4_B	HT1 X	237.57	1119.83	1298.77	0.06545	0.2597	0.315
4_C	HT1 X	239.54	1114.13	1269.76	0.06112	0.2679	0.3223
5_A	HT1 Y	200.37	1138.75	1267.70	0.06672	0.39252	0.4486
5_B	HT1 Y	203.20	1158.52	1291.05	0.06090	0.3016	0.3956
5_C	HT1 Y	202.79	1148.39	1273.78	0.06392	0.2998	0.3533
6_A	HT1 Z	204.95	1179.36	1303.79	0.06731	0.2142	0.4166
6_B	HT1 Z	195.38	1170.04	1302.25	0.09138	0.2708	0.3795
6_C	HT1 Z	199.16	1177.29	1303.85	0.07935	0.2781	0.3896
7_A	HT2 X	209.36	1174.51	1310.11	0.03687	0.2833	0.3777
7_B	HT2 X	205.38	1175.63	1310.10	0.05649	0.2675	0.2821
7_C	HT2 X	206.37	1165.15	1299.18	0.04671	0.2835	0.2871
8_A	HT2 Y	188.17	1154.80	1252.91	0.01516	0.2900	0.3776
8_B	HT2 Y	192.17	1166.99	1295.70	0.03115	0.2922	0.2862
8_C	HT2 Y	191.17	1164.80	1282.12	0.02316	0.2981	0.2972
9_A	HT2 Z	202.84	1192.73	1316.65	0.05882	0.4016	0.4091
9_B	HT2 Z	211.91	1179.89	1310.53	0.04332	0.3214	0.5028
9_C	HT2 Z	206.37	1182.36	1303.02	0.05111	0.3319	0.4533
10_A	HT3 X	211.48	1139.04	1185.78	0.00900	0.229	0.373
10_B	HT3 X	222.41	1146.49	1244.04	0.01150	0.2890	0.4972
10_C	HT3 X	217.94	1144.95	1333.13	0.01019	0.2909	0.3437
11_A	HT3 Y	211.32	1131.84	1260.91	0.02999	0.2783	0.4026
11_B	HT3 Y	207.94	1157.49	1252.38	0.01215	0.2852	0.3646
11_C	HT3 Y	210.63	1147.40	1258.92	0.02110	0.2952	0.3665
12_A	HT3 Z	196.30	-	860.09	0.00454	0.2879	0.3798
12_B	HT3 Z	184.76	-	1104.94	0.00713	0.328	0.3516
12_C	HT3 Z	191.53	-	984.45	0.00589	0.3328	0.3616

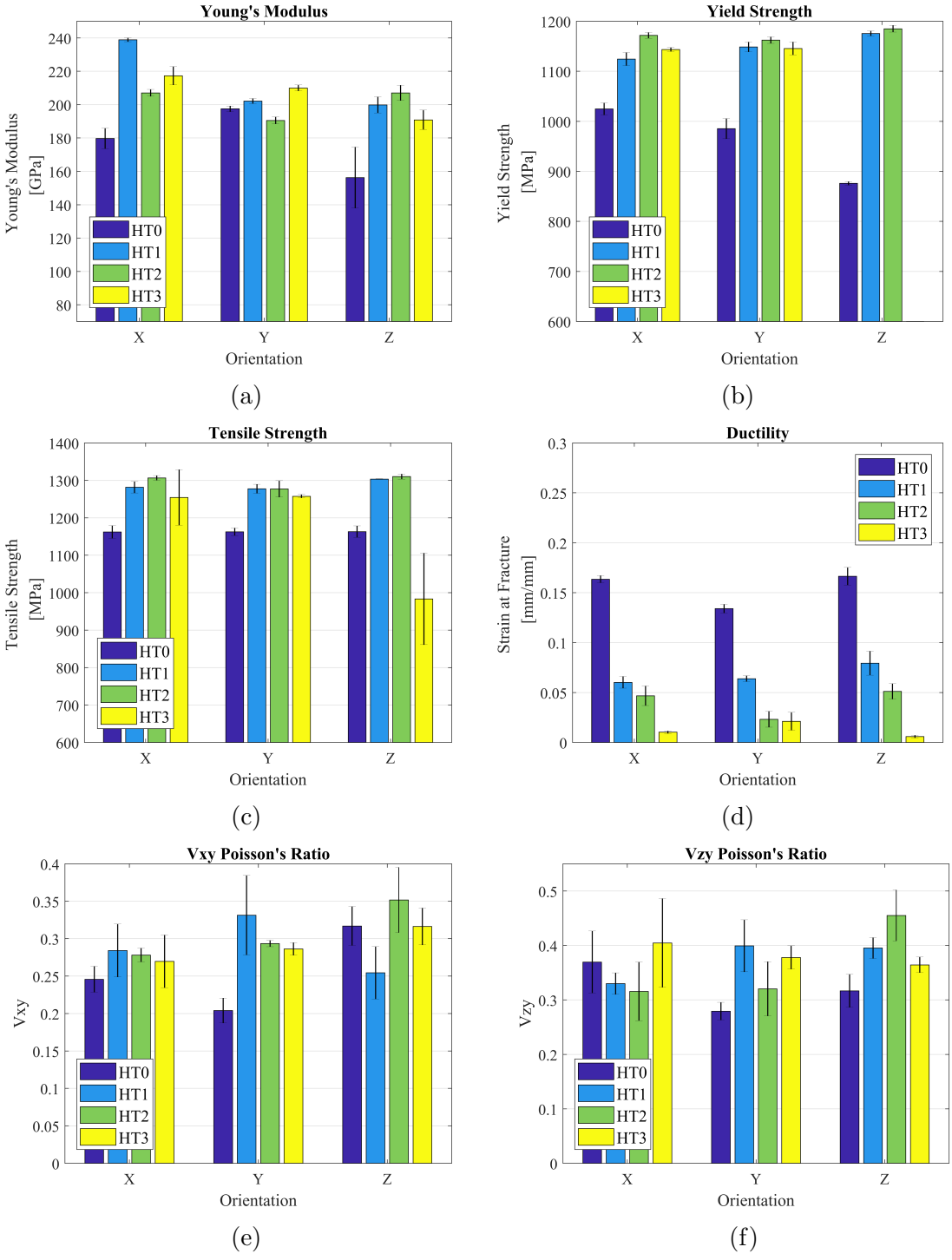

Figure 4.5: Mechanical properties of DMLS 15-5PH with different heat treatments vs building orientation.

hardened specimens are lower than specimens hardened by H900 directly without annealing by comparing the results of this study with the results of Rafi et al. [96] and Dempsey et al. [154] where the former reported a minimum 12% strain and the latter reported minimum 21.1% strain before fracture. This can be explained by the retained austenite in specimens directly hardened without annealing [101, 154–156]. The ductility can be better illustrated with the aid of Figure 4.6-Figure 4.9, which show the strain fields just before and after the fracture.

The influence of the heat treatments on Poisson's ratios $v_{xy} = -d\varepsilon_x/d\varepsilon_y$ and $v_{zy} = -d\varepsilon_z/d\varepsilon_y$ are presented in Figure 4.5(e) and Figure 4.5(f), respectively. Poisson's ratio for the heat-treated specimens was generally higher than the as-built specimens. In addition, we can see that vzy was generally higher than vxy, which suggests that Poisson's ratio depend more on the geometry of the part than on the building direction.

Figure 4.6-Figure 4.9 show the strain fields of tensile specimens just before and after a fracture. From the results shown in 4.6, we can see that as-built specimens suffered from high strains before failing. The effect of necking is clear with high strains in the necking area going up to 30%. High deformation and area reduction are clear in the strain fields just after a fracture. HT1 specimens were able to hold less strain before failing and less necking occurred before fracture as can be seen from Figure 4.7. The strain around the necking area dropped to 10%. In addition, one of the Y-built specimens broke slightly below the area with high strain as can be seen in Figure 4.7(c,d) indicating the presence of defects allowing the failure to occur there instead of the area with the high strain slightly above. From the images after fracture, we can still see that the fracture surface is not smooth, and some deformation has occurred before failure. HT2 specimens behaved similarly to HT1 specimens however they held even less strain, around 7%, and necking is not clear as can be observed in Figure 4.8. One of the Y-built specimens had two areas of high strain, one inside the gauge length and one slightly above. The specimen ultimately failed at the location slightly above as can be seen in Figure 4.8(b,c). From Figure 4.9 we can see that HT3 specimens held the lowest strains before fracture with no necking at all. Furthermore, the fractures usually occurred outside the gauge length in unpredictable locations. The fractured surfaces were mostly flat.

To investigate the influence of the heat treatments on the repeatability and anisotropy, the standard deviation of each property for each heat treatment was calculated and presented in Table 4.5. The values in column σ represent the scatter of the measured property for all the specimens sharing the same heat treatment regardless of the orientation during fabrication. The values in column A represent the standard deviation of the averaged property values for each orientation for a specific heat treatment which means it only calculates the variations of the averaged value for the X orientation, Y orientation, and Z orientation, which are the averaged points shown in Figure 4.5. For example, it can be seen from Table 4.5 that the A

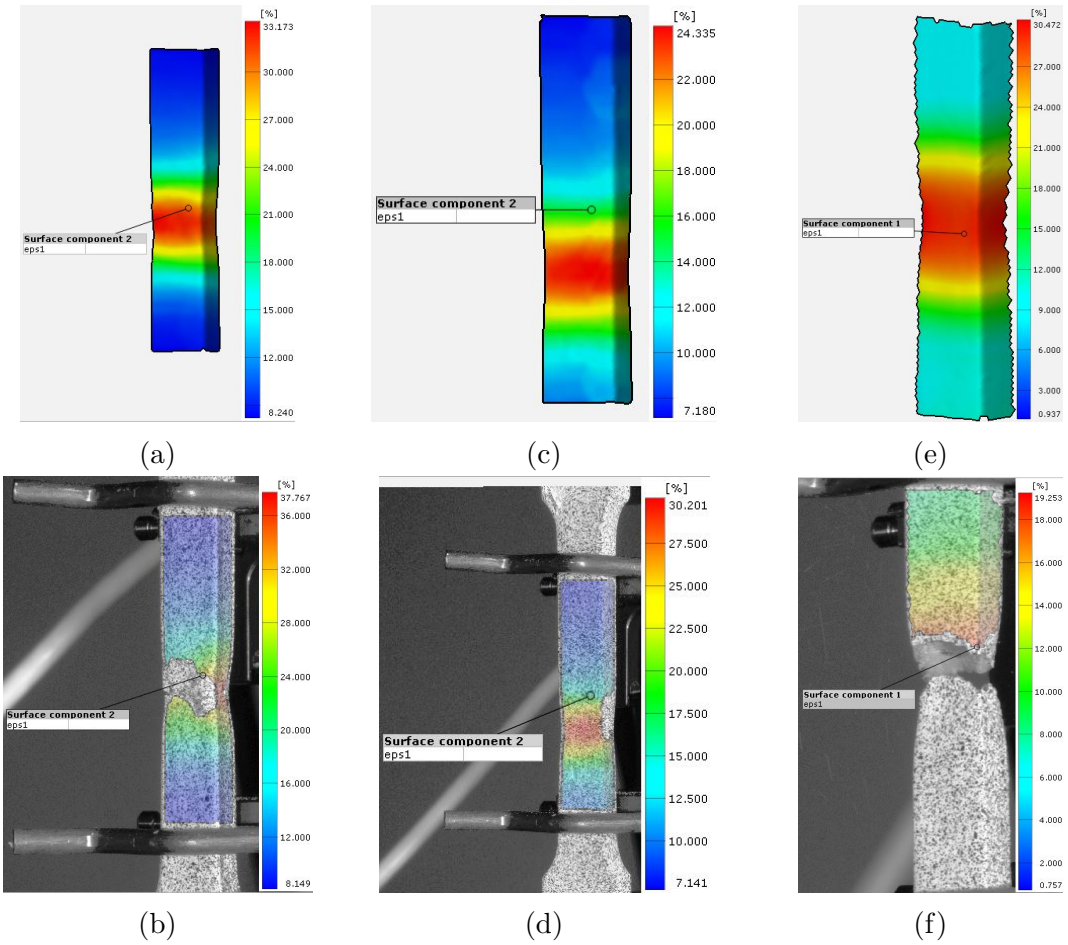

Figure 4.6: Strain fields of as-built (HT0) DMLS 15-5PH specimens generated by the DIC system. a) X-built specimen just before fracture. b) X-built specimen just after fracture. c) Y-built specimen just before fracture. d) Y-built specimen just after fracture. e) Z-built specimen just before fracture. f) Z-built specimen just after fracture.

value for HT0 for the tensile strength is equal to 0.44. This means that the tensile strength of the X, Y and Z orientations are very close, which can be confirmed by looking at Figure 4.5(c). However, by looking at the σ value we can see that there is still a significant scatter in tensile strength for HT0 even though the averages of the X, Y and Z orientations are very similar.

HT1 slightly reduced the scattering (σ) in Young's modulus, yield strength, and ductility. HT1 did not reduce the anisotropy (A) except in the yield strength. From Table 4.5 we can see that HT2 has a significantly lower A and σ values for Young's modulus and Yield strength properties. In addition, HT2 has the second

lowest σ and A for the tensile strength after HT0, however, HT2 has the second largest A and σ values for the ductility. HT3 showed the second lowest anisotropy (A) and scatter (σ) in Young's modulus after HT2. However, HT3 showed the worst scatter and anisotropy in the yield and tensile strength. The small scatter and anisotropy in the ductility shown by HT3 are caused by the sudden fracture at very small strains. Overall HT2 shows the most promising results in reducing the anisotropy and the scatter in most of the properties.

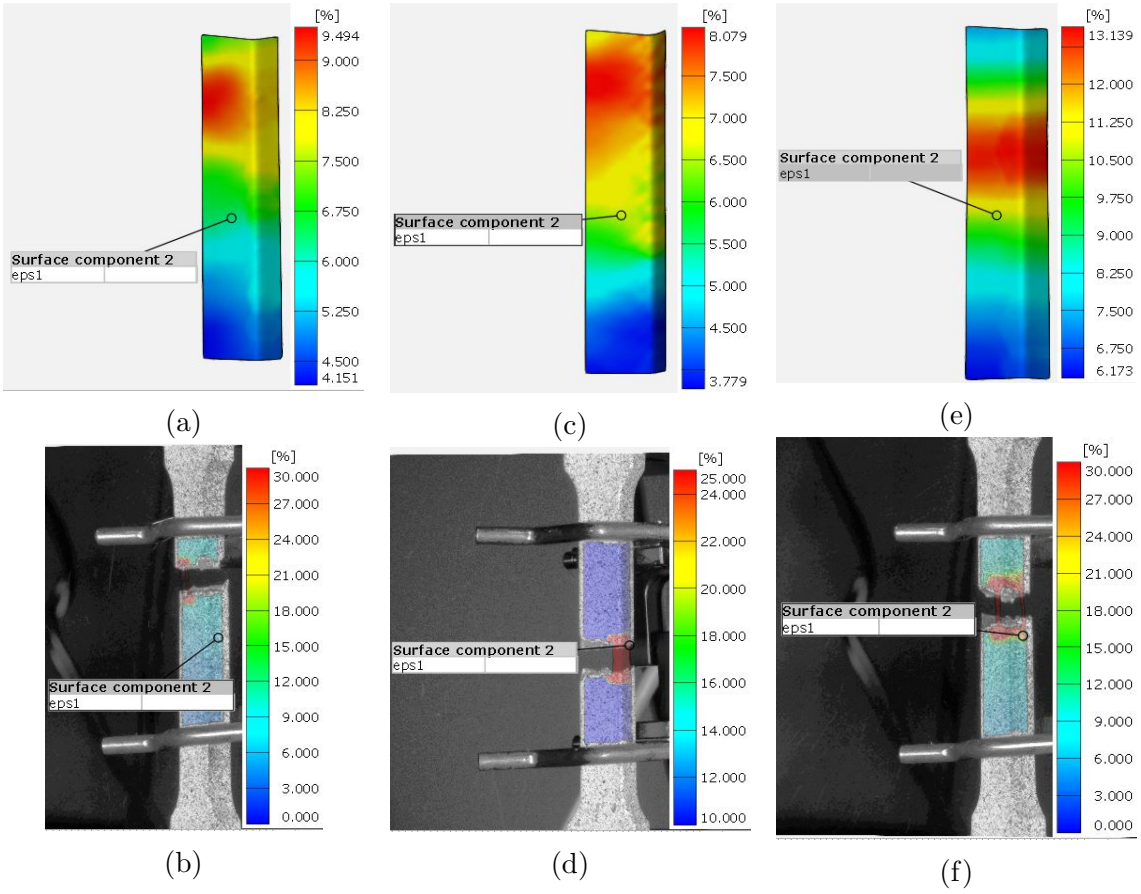

Figure 4.7: Strain fields of HT1 DMLS 15-5PH specimens generated by the DIC system. a) X-built specimen just before fracture. b) X-built specimen just after fracture. c) Y-built specimen just before fracture. d) Y-built specimen just after fracture. e) Z-built specimen just before fracture. f) Z-built specimen just after fracture.

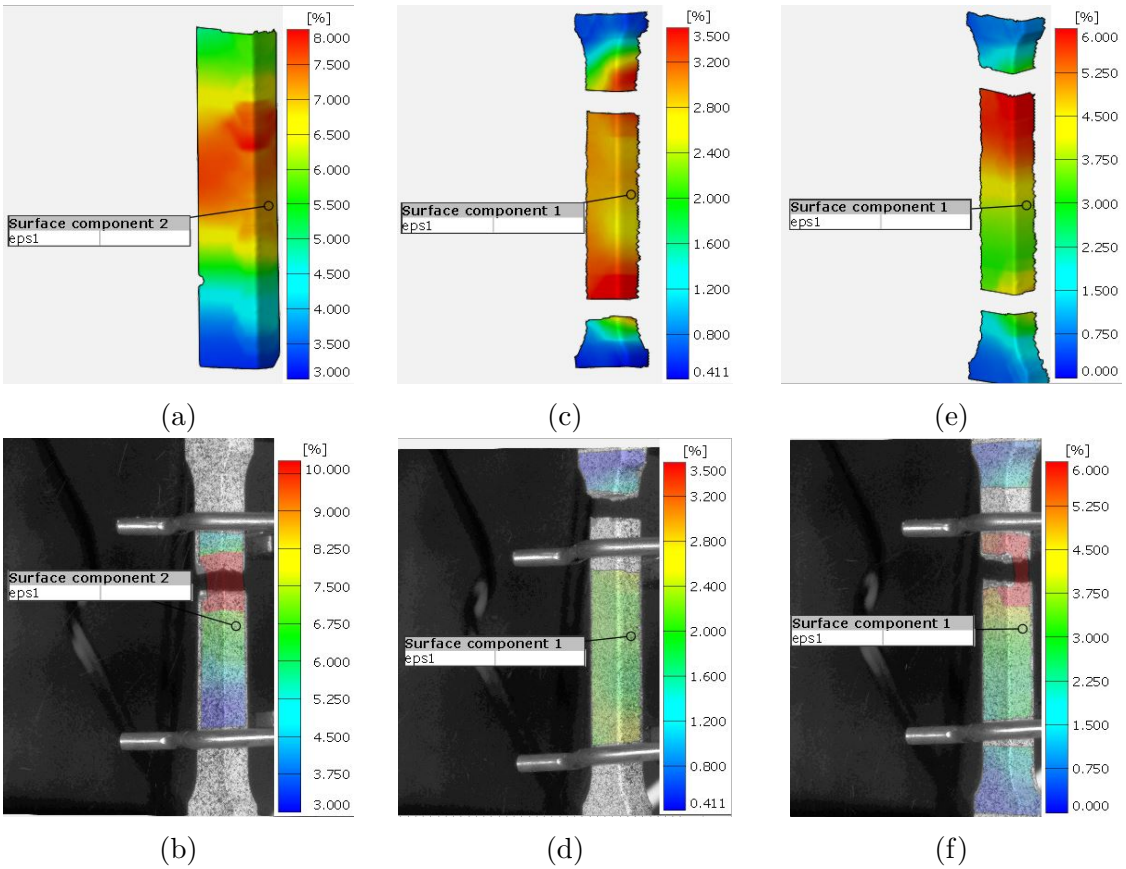

Figure 4.8: Strain fields of HT2 DMLS 15-5PH specimens generated by the DIC system. a) X-built specimen just before fracture. b) X-built specimen just after fracture. c) Y-built specimen just before fracture. d) Y-built specimen just after fracture. e) Z-built specimen just before fracture. f) Z-built specimen just after fracture.

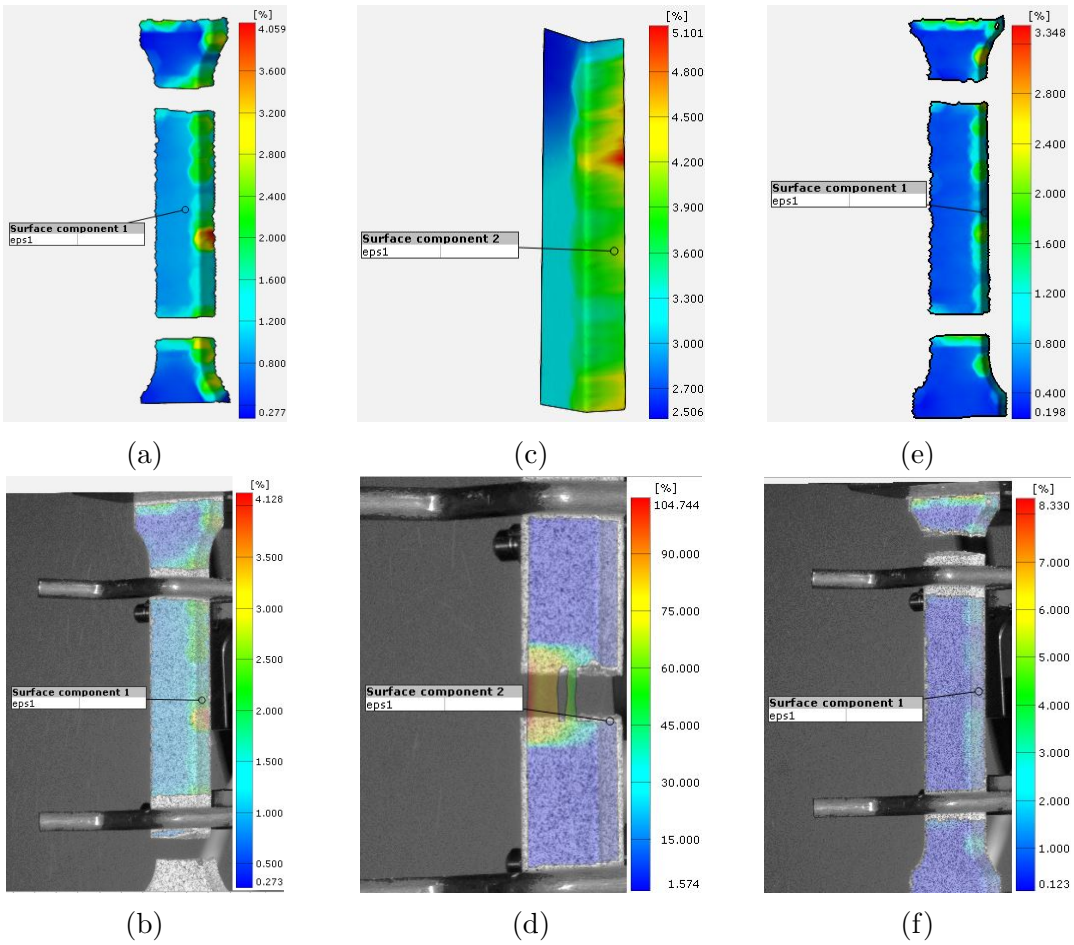

Figure 4.9: Strain fields of HT3 DMLS 15-5PH specimens generated by the DIC system. a) X-built specimen just before fracture. b) X-built specimen just after fracture. c) Y-built specimen just before fracture. d) Y-built specimen just after fracture. e) Z-built specimen just before fracture. f) Z-built specimen just after fracture.

Table 4.5: Standard deviation of the resulting mechanical properties for different heat treatments of DMLS 15-5PH

Heat Treatment	Young's Modulus		Yield Strength		Tensile Strength		Ductility	
	A	σ	A	σ	A	σ	A	σ
HT0	20.68	20.37	77.09	67.81	0.44	12.53	0.0179	0.1640
HT1	21.91	19.15	25.63	23.78	13.69	15.20	0.0104	0.0112
HT2	9.55	8.69	11.45	11.34	13.38	13.32	0.0150	0.0150
HT3	13.64	12.50	94.99	572.3	157.45	154.02	0.0078	0.0082

4.3.2 SEM Fractography

The study of the fractured surfaces of the 15-5PH specimens is presented in Figure 4.10-Figure 4.13. From Figure 4.10 we can see that the topography of as-built specimens is very prominent and rise high from the surface. Also, from the high magnification images in Figure 4.10(b,d,f) we can see clear topography, however, it is more prominent in X and Z-built specimens, which agrees with the higher ductility associated with these building directions than the Y building direction. The fracture patterns of the as-built specimens are similar to the vertically fabricated conventional condition A specimens reported in the work of Chae et al. [157], in addition to [110]. The presence of porosity should be noted as can be seen in panels c and e of Figure 4.10. For the HT1 and HT2 heat-treated specimens, the fractured surfaces were mostly flat in the center but had high changes in topography at the edges as can be seen in Figure 4.11(a,c,e) and Figure 4.12(a,c,e). These patterns are similar to the fractured surfaces present in the work of Jafarlou et al. [158], where the fractured surfaces had a central flat zone and shear lips around the edges. The flat central zone was smaller in the work of Jafarlou et al. however, but that can be due to precipitation-hardening the specimens (H900) without solution annealing them. Porosity is still present however only near the edges and more can be observed in HT1 compared to HT2 and both in less density than the as-built specimens. The topography observed in the high magnification images of HT1 and HT2 is similar to the ones observed in the as-built specimens. However, the holes in HT1 are more plentiful than in HT2. HT3 specimens' fractured surfaces are almost completely flat, even at the edges. Porosity is more scarce in HT3 specimens compared to the as-built specimens and the rest of the heat treatments as can be seen in Figure 4.13(a,c,e). Moreover, the holes are more sparse as can be seen in the high magnification images in Figure 4.13(b,d,f), which could be caused by the much lower ductility shown by the HT3 specimens. The flat fracture surfaces described

in Figure 4.13 for HT3 illustrate a brittle fracture behavior, while the prominent topography shown in Figure 4.10 for the as-built specimens illustrates a ductile behavior. The presence of small spheres in the halls can be observed in the high magnification images of the fractured surfaces in Figure 4.10-Figure 4.13, which was pointed to be precipitation strengthening phases in [66]. However, it should be noted that their presence in HT0 specimens is rare and can only be seen in frequency in the X-built specimen as in Figure 4.10(a) but they are very abundant in HT1 and HT2 specimens as can be seen in Figure 4.11(b,d,f) and Figure 4.12(b,d,f). In HT3 specimens the presence of these spherical particles is less than in HT1 and HT2 specimens but still significantly more than the as-built (HT0) specimens. Also, we can see that in Z-built specimens in HT3 very few of these strengthening precipitates compared to the X and Y-built specimens which can explain the poor yield and tensile strength of these specimens.

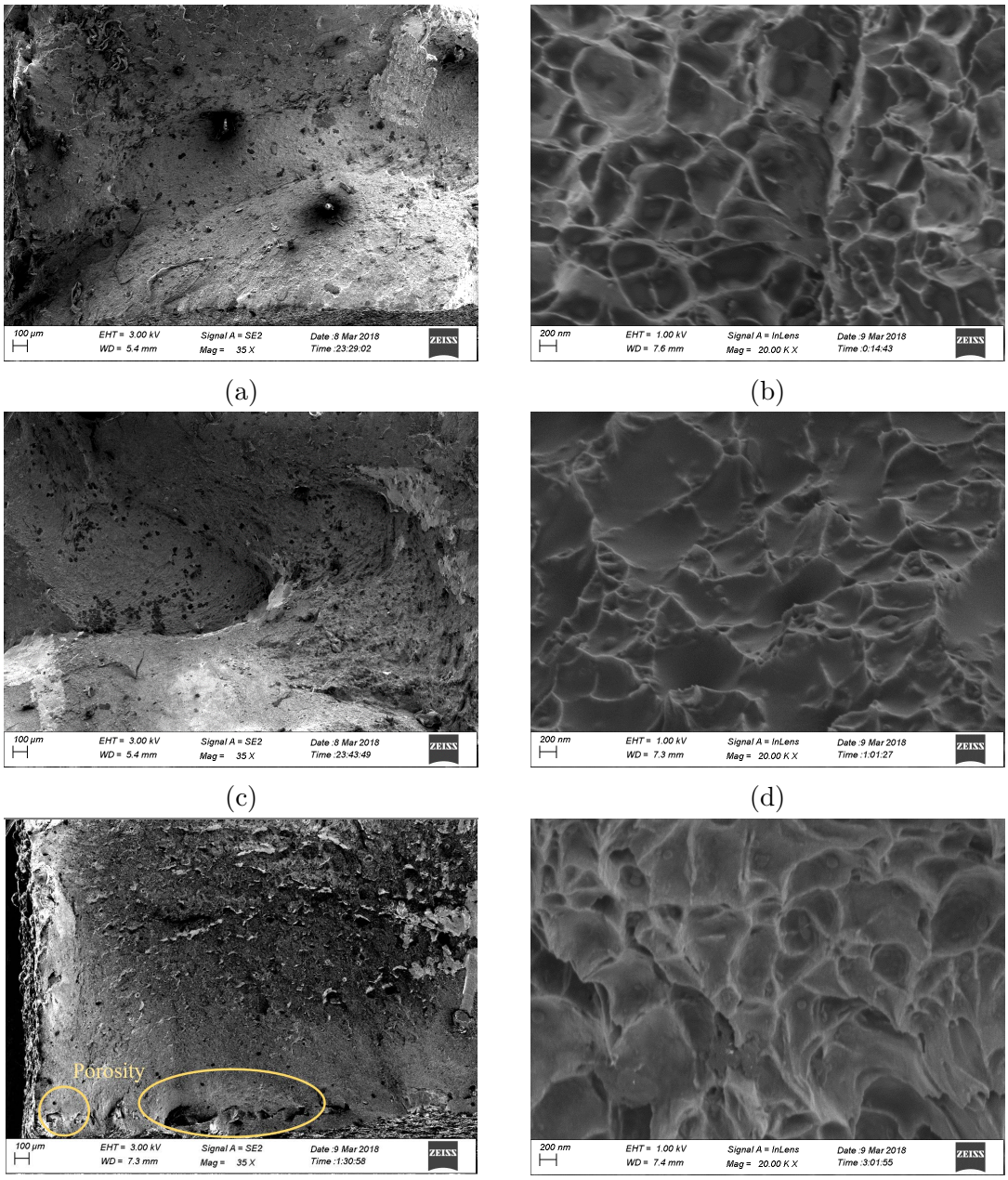

Figure 4.10: SEM fractography of as-built 15-5PH (HT0). a) X-building direction at 35X magnification. b) X-building direction at 20KX magnification. c) Y-building direction at 35X magnification. d) Y-building direction at 20KX magnification. e) Z-building direction at 35X magnification. f) Z-building direction at 20KX magnification.

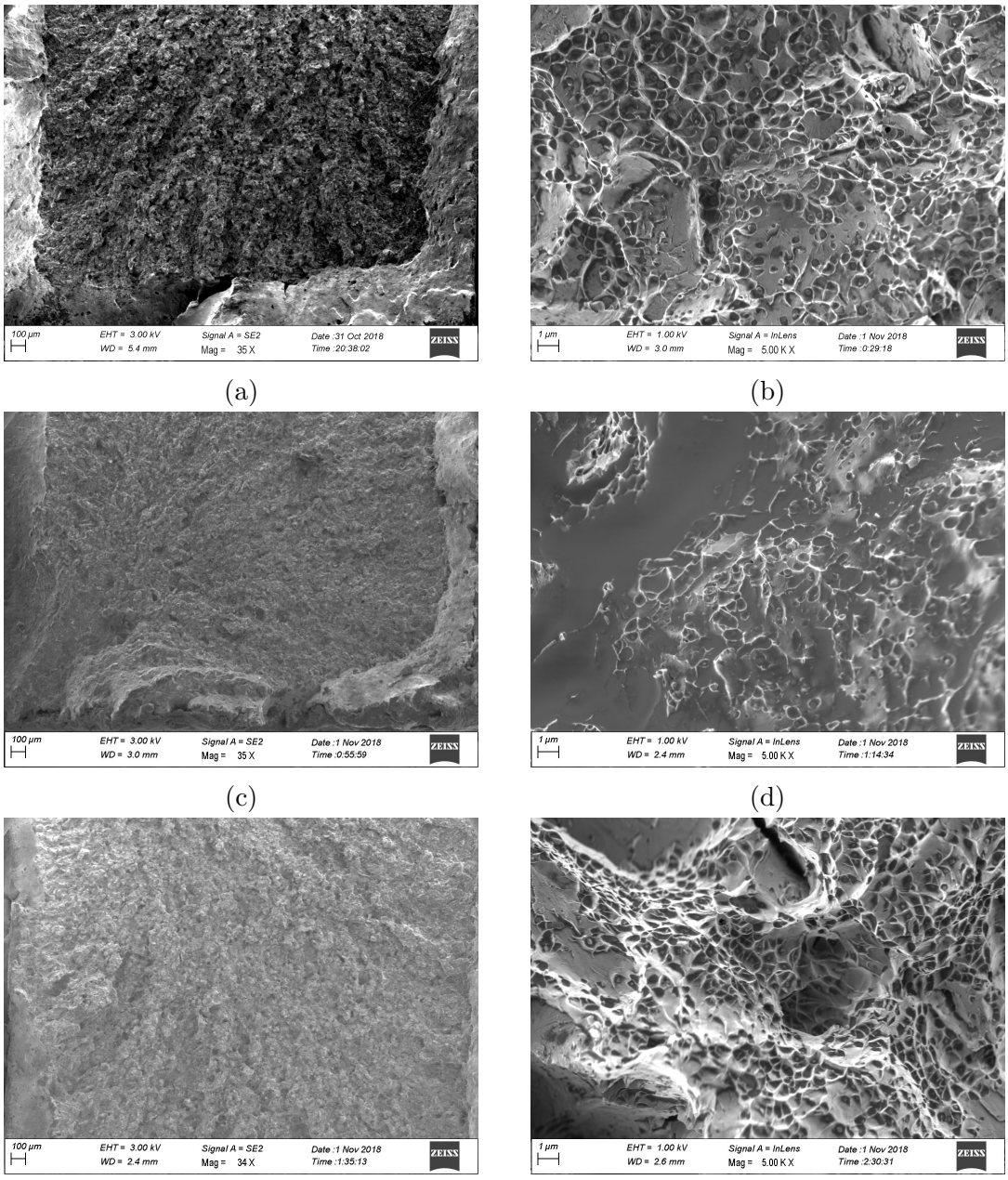

Figure 4.11: SEM fractography of HT1 15-5PH. a) X-building direction at 35X magnification. b) X-building direction at 20KX magnification. c) Y-building direction at 35X magnification. d) Y-building direction at 20KX magnification. e) Z-building direction at 35X magnification. f) Z-building direction at 20KX magnification.

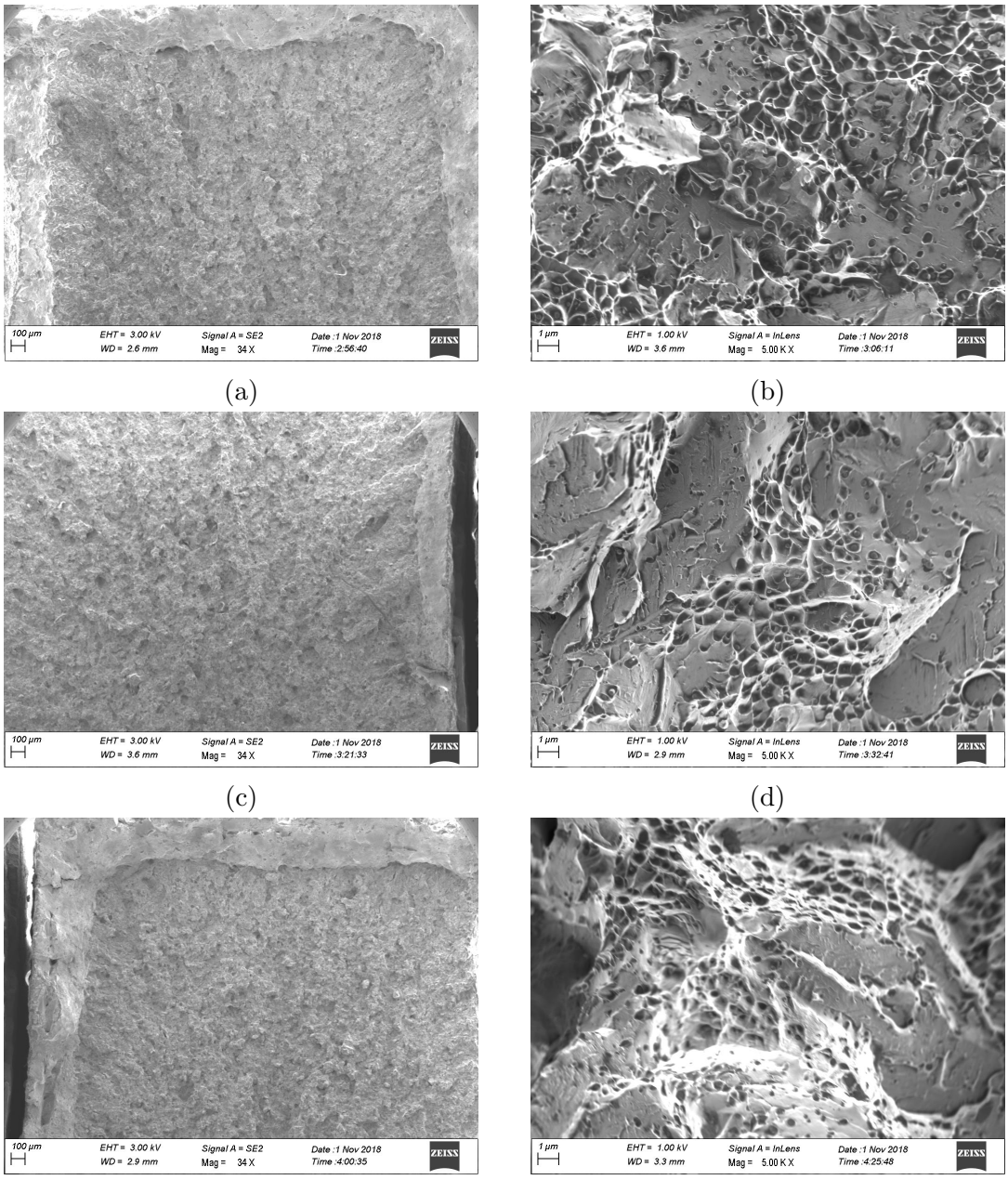

Figure 4.12: SEM fractography of HT2 15-5PH. a) X-building direction at 35X magnification. b) X-building direction at 20KX magnification. c) Y-building direction at 35X magnification. d) Y-building direction at 20KX magnification. e) Z-building direction at 35X magnification. f) Z-building direction at 20KX magnification.

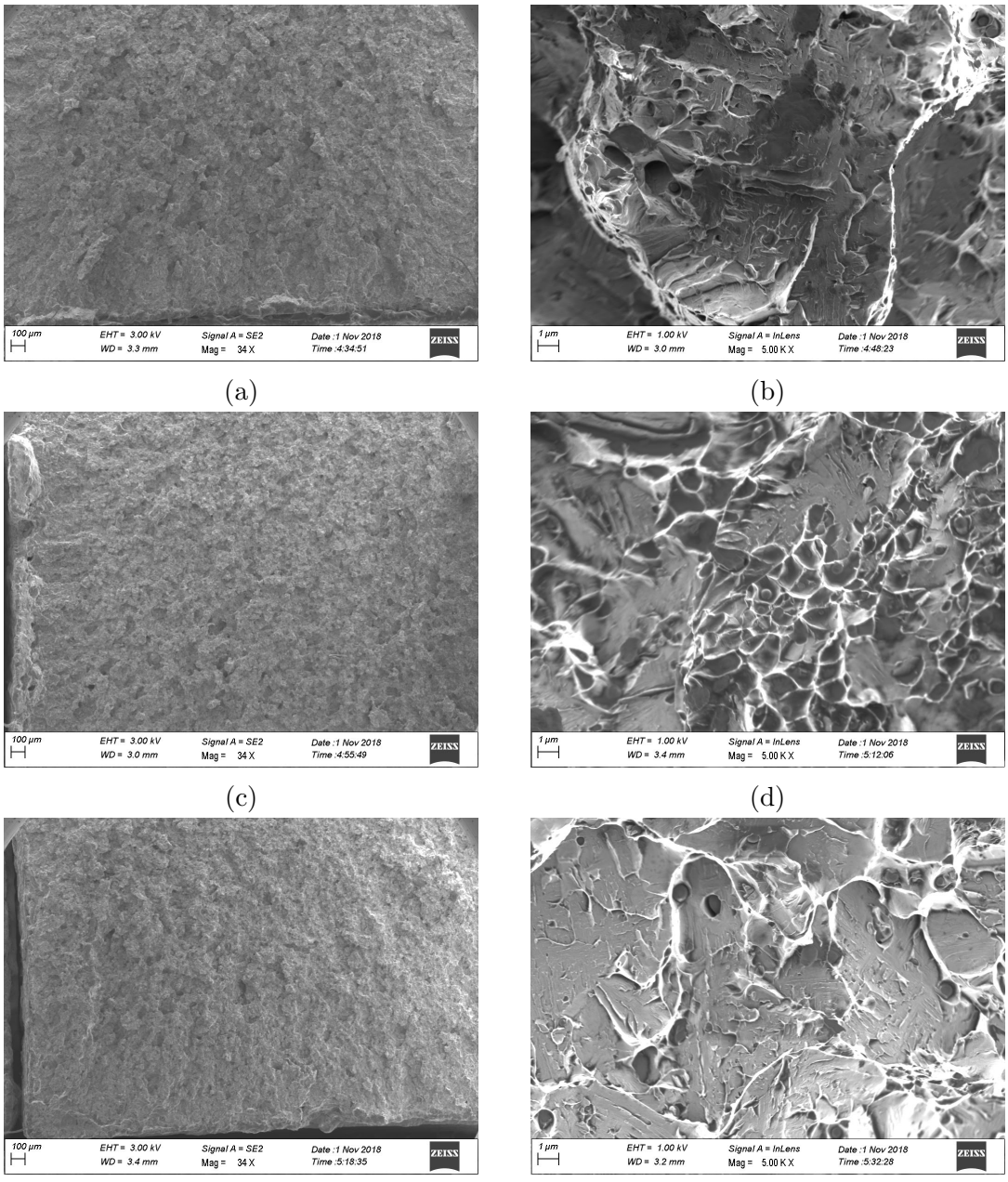

Figure 4.13: SEM fractography of HT3 15-5PH. a) X-building direction at 35X magnification. b) X-building direction at 20KX magnification. c) Y-building direction at 35X magnification. d) Y-building direction at 20KX magnification. e) Z-building direction at 35X magnification. f) Z-building direction at 20KX magnification.

4.3.3 Microstructure analysis

The microstructure analysis of 15-5PH was done using brightfield optical microscopy. The images were taken at magnifications of 100x, 200x, and 500x. In the microstructure of as-built specimens, we can see the effect of the specimens' building direction layer by layer in addition to the fusing of each layer along the laser's scan lines. In Figure 4.14(a) the image shows a stack of layers from right to left, which indicates the building direction. We can also see the cross-section of the overlapping scanning lines, which were scanned in a direction out of the plane. The size of the grains at the center of a scanline is significantly larger than at the border of the scanline cross-section. This can be seen easier in Figure 4.14(b) at 500X magnification. By comparing Figure 4.14(a,b) and Figure 4.14(c,d) we can see that the microstructure on the plane normal to the tensile force for both building directions X and Y share the same pattern. However, the microstructure on the same plane for building direction Z is completely different as can be seen in Figure 4.14(e,f). The scan lines can be seen since they aligned in the plane for the Z-built specimens as opposed to the X and Y-built specimens, where we can only see the cross-sections of the scan lines and melt pools. The grain size at the center of the scanlines in Z-built specimens is slightly larger than at the borders of the scanlines making the grains size in the Z-built specimens more uniform compared to the X and Y-built specimens. In addition, the grain size in the Z-built specimens in the imaged plane is generally smaller than the grain sizes in X and Y-built specimens at the center of the scanlines cross-sections. These patterns are similar to the microstructure revealed in previous studies such as [77, 154, 157, 159] which also reported the microstructure to be mostly martensitic with a small percentage of austenite ranging 4%-15% with a maximum of 20% reported in [154]. In [21] it was shown that martensite BCT is very close to BCC due to the low carbon content, therefore it is hard to distinguish from the ferrite phase using X-ray diffraction alone. In [160] it was shown that instead of the matrix being martensite it is delta ferrite. However, this study was done on 17-4PH stainless steel which is not ferrite free. The similarity in the mechanical properties between the X and Y-built specimens can be explained by the similarity in the microstructure on the planes normal to the tensile force as observed in Figure 4.14(a, c). On the other hand, the different microstructure pattern developed in the Z-built specimens as shown in Figure 4.14(e) explains the difference in Young's modulus and yield strength displayed by the Z-built specimens compared to the X and Y-built specimens. Furthermore, the differences between the X and Y-built specimens mechanical properties can be explained by the different retained austenite percentage, which was shown to depend on the orientation during fabrication [101].

The heat-treated specimens have shown a completely different microstructure than the ones present in the as-built specimens as can be seen from Figure 4.15-Figure 4.17. HT1, HT2, and HT3 have displayed microstructure patterns more resembling to the martensitic microstructure [21, 23] than the as-built specimens.

Also, by comparing panels a, c and e of Figure 4.15 we can see that the microstructure of HT1 specimens is similar regardless of the building orientation during fabrication. Similarly, from Figure 4.16 and Figure 4.17 we can see that the microstructure of HT2 and HT3 does not depend on the orientation during fabrication. This explains the more isotropic behavior of the heat-treated specimens compared to the as-built specimens. Although the microstructure patterns displayed by HT1, HT2, and HT3 are quite similar in shape and there is no obvious size difference in the grains, however, HT3 specimens have shown significantly more brittle behavior than HT1 and HT2 specimens. The higher temperature used for homogenizing the HT3 specimens might be the reason, according to [161] annealing at higher temperatures than the standard will cause delta ferrite to form and lower elongation values, In addition to the possibility of forming carbides during the hardening treatment at the ferrite boundaries. However, [160] suggests that if another solution annealing was conducted at 1050°C followed by air quenching the ferrite should transform to martensite, which will result in the 15-5PH responding in a proper way to the precipitation hardening.

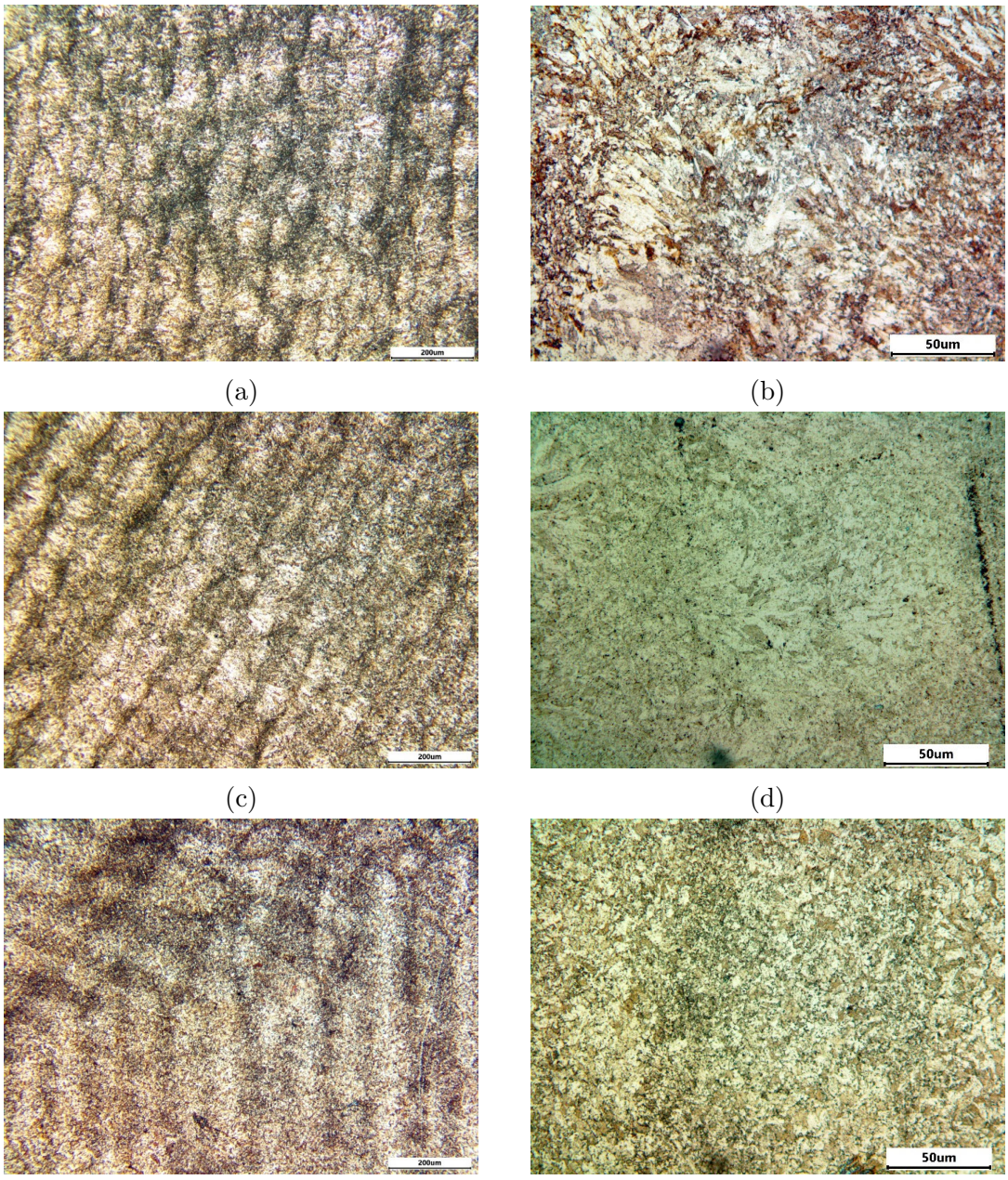

(a) (b)

(c) (d)

(e) (f)

Figure 4.14: Microstructure of as-built DMLS 15-5PH (HT0) imaged on the plane normal to the tensile force. a) X-building direction at 100X magnification, b) X-building direction at 500X magnification, c) Y-building direction at 100X magnification, d) Y-building direction at 500X magnification, e) Z-building direction at 100X magnification, f) Z-building direction at 500X magnification.

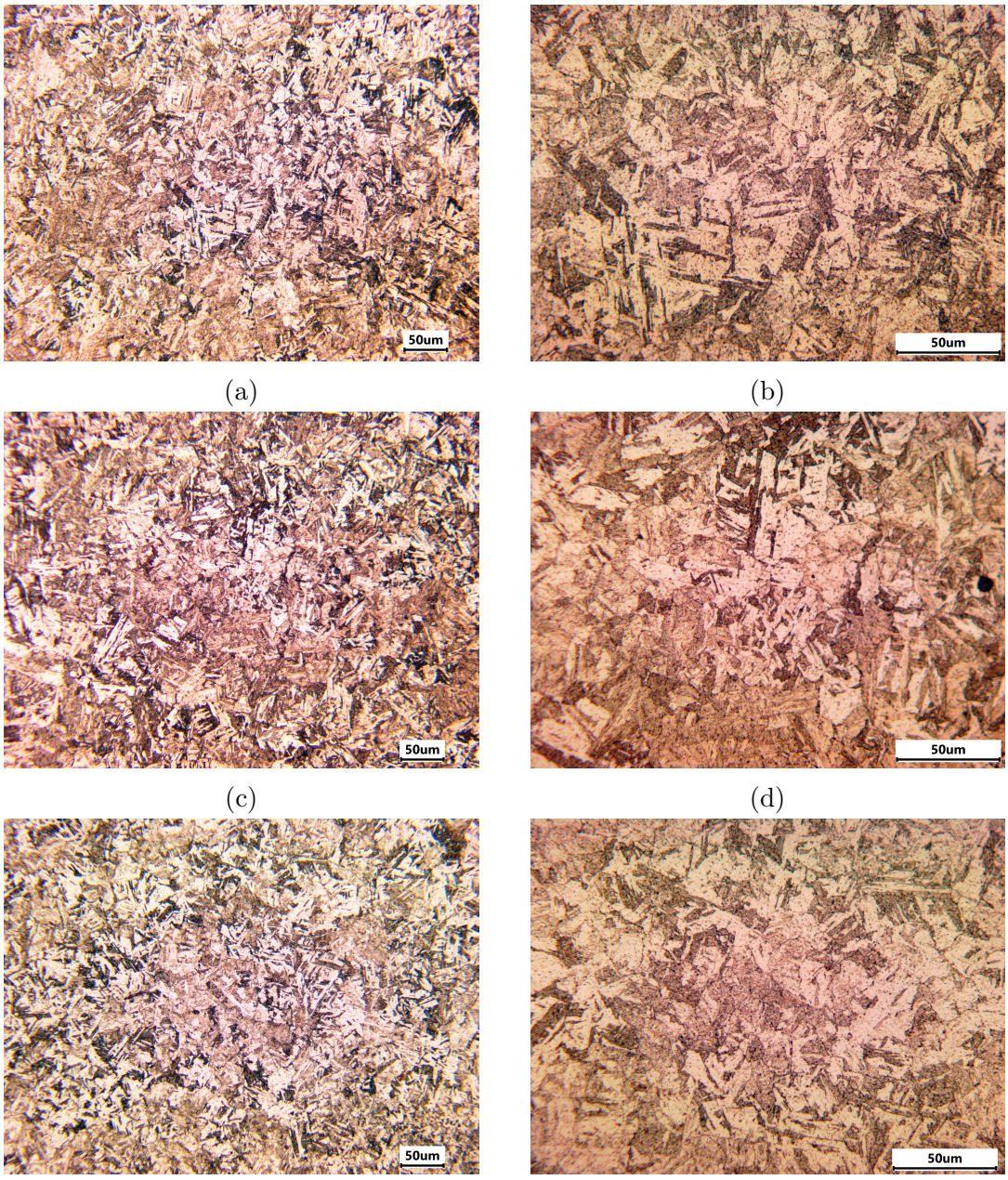

(a) (b) (c) (d) (e) (f)

Figure 4.15: Microstructure of HT1 of DMLS 15-5PH imaged on the plane normal to the tensile force. a) X-building direction at 200X magnification, b) X-building direction at 500X magnification, c) Y-building direction at 200X magnification,d) Y-building direction at 500X magnification, e) Z-building direction at 200X magnification, f) Z-building direction at 500X magnification.

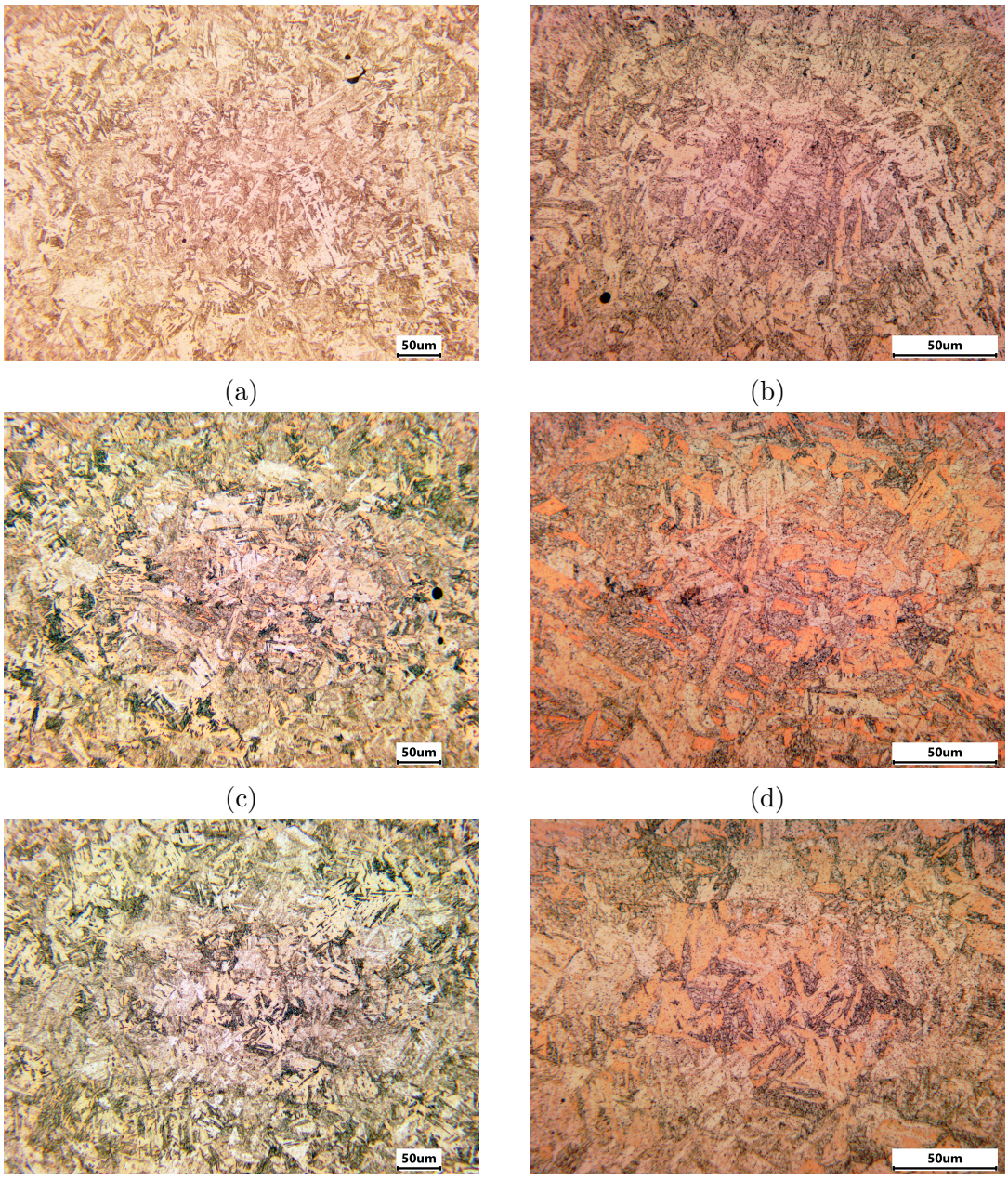

(a) (b) (c) (d) (e) (f)

Figure 4.16: Microstructure of HT2 of DMLS 15-5PH imaged on the plane normal to the tensile force. a) X-building direction at 200X magnification, b) X-building direction at 500X magnification, c) Y-building direction at 200X magnification,d) Y-building direction at 500X magnification, e) Z-building direction at 200X magnification, f) Z-building direction at 500X magnification.

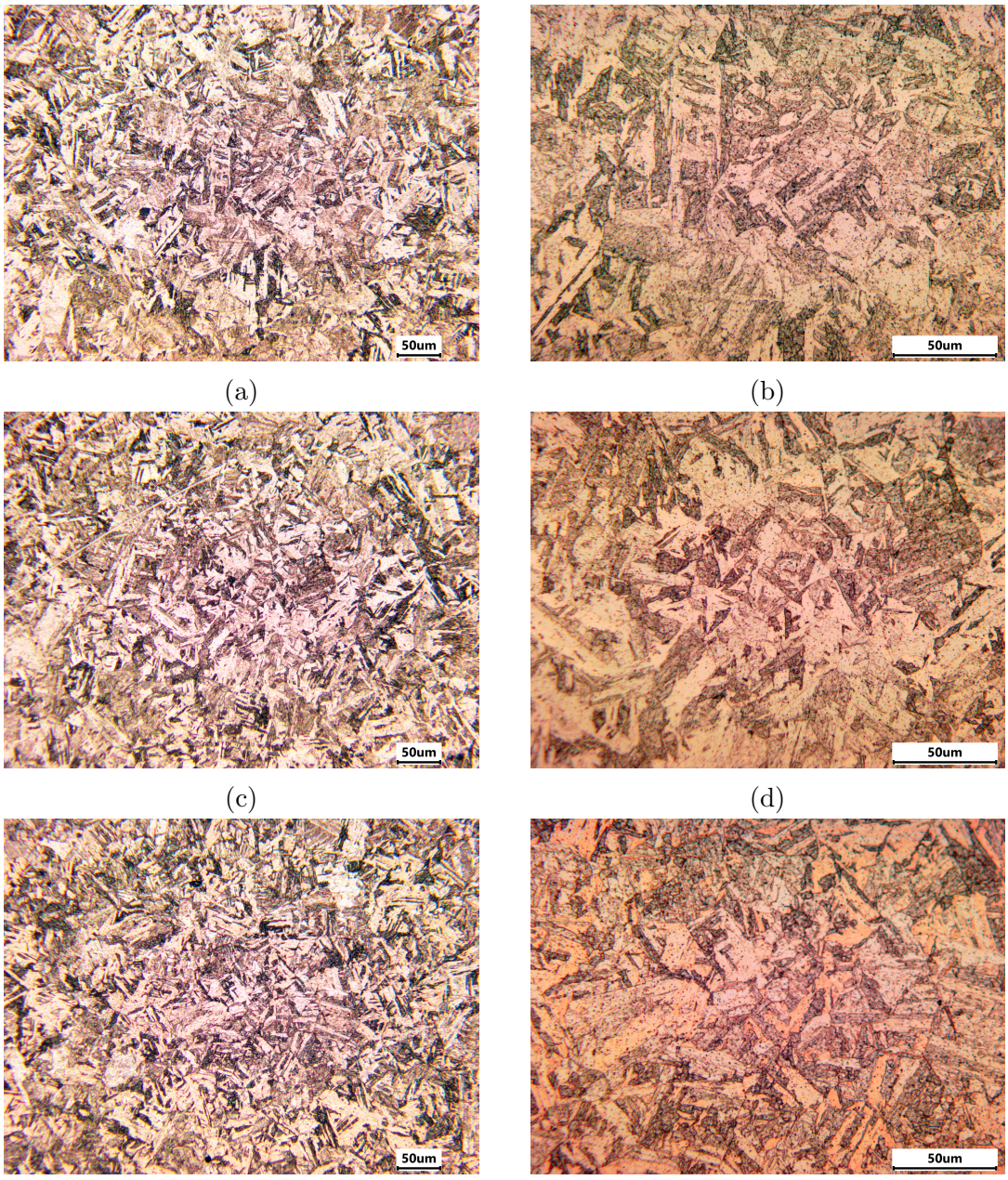

(a) (b) (c) (d) (e) (f)

Figure 4.17: Microstructure of HT3 of DMLS 15-5PH imaged on the plane normal to the tensile force. a) X-building direction at 200X magnification, b) X-building direction at 500X magnification, c) Y-building direction at 200X magnification,d) Y-building direction at 500X magnification, e) Z-building direction at 200X magnification, f) Z-building direction at 500X magnification.

4.4 Coclusions

In this study, the authors presented an investigation on the influence of different solution annealing heat treatments followed by H900 precipitation hardening on the mechanical properties of DMLS 15-5PH samples. The study investigated a total of 12 patches with three different heat treatment conditions in addition to the as-built condition. Each patch of the different heat treatment conditions and building condition was tested using three identical specimens to include repeatability. Specimens were built in different directions relative to the building bed. The microstructure of these specimens has been investigated to explain the mechanical behavior. This study has concluded the following:

- The mechanical properties of DMLS parts such as the tensile strength, yield strength and Young's modulus of as-built specimens depend on the orientation during fabrication. This was explained by the different microstructures developed on the plane normal to the tensile force.

- The mechanical properties of DMLS 15-5PH samples have shown significant improvement after solution annealing and then precipitate hardening. The increase in stiffness, yield, and tensile strengths was at the expense of reducing the ductility of the specimens.

- By increasing the duration of the solution annealing heat treatment from one hour to three hours the yield and tensile strengths were slightly increased at the expense of further reducing the ductility of the specimens. This suggests the opportunity to optimize the duration to improve the homogeneity of the parts and reduce and defects and porosity. In addition, extending the solution annealing heat treatment time resulted in the highest overall repeatability and reduction in anisotropy. This means DMLS parts can be manufactured in the most convenient orientation for fabrication and still obtain similar mechanical properties to parts fabricated in the optimum orientation for the mechanical properties.

- Heat treating 15-5PH specimens fabricated by DMLS at 1200°C and furnace cooling it before solution annealing has proved to be detrimental and caused the specimens to fail suddenly sometimes before yielding and at unpredictable locations.

- Using an extended solution annealing coupled with a different precipitation hardening heat treatment such as H1150 might improve the fatigue life of DMLS 15-5PH parts, which showed better performance over H900 with the standard solution annealing [101].

Chapter 5

MICROSTRUCTURE AND MECHANICAL PROPERTIES OF HEAT TREATED INCONEL 718 DMLS PARTS

5.1 Introduction

The processing parameters of metal-based additive manufacturing can be optimized to produce parts with comparable tensile test mechanical properties to wrought and forged parts. However, it was found that the processing parameters required to optimize the mechanical properties are usually different than the processing parameters required to maximize the relative density [162]. This is due to the rapid cooling required to develop a microstructure with a small grain size, which improves the strength of the material. This, however, does not allow enough time to fully melt the metal powder and produce fully dense parts with minimum porosity. Pores and defects significantly reduce the reliability of the fabricated parts. This issue is more severe for parts under dynamic loading as will be discussed in later chapters. In addition, as-fabricated parts suffer from high anisotropy in their mechanical properties due to the different microstructure during the layer-by-layer fabrication. Therefore, to achieve the absolute optimum part quality, this work adopts processing parameters that maximize the relative density and then proposes different heat treatments that aim at improving the mechanical properties of the completed part. The heat treatments proposed aim at homogenizing the microstructure without increasing the grain size significantly. Standard heat treatments have proven insufficient to homogenize the microstructure and reduce the anisotropy. In addition to that, the standard solution annealing temperature of IN718 is below the solvus temperature of δ and laves phases, therefore, it will fail in dissolving any δ and laves precipitates that might have developed during laser melting. Two proposed heat treatments with temperatures above the solvus temperature of the detrimental phases are investigated and compared with the as-fabricated and standard heat-treated specimens.

5.2 Methodology

5.2.1 Experimental plan

A total of 12 patches of specimens were fabricated to examine the influence of the different solution heat treatments on the mechanical properties of DMLS IN718.

Each patch contained three specimens to check for repeatability. Four patches were fabricated in the XYZ orientation, another four in the YZX orientation, and the last four in the ZXY, as described in the ASTM-F2971-13 standard [1], and abbreviated in this work as X, Y, and Z, respectively. Figure 5.1 shows the orientation of the samples. Three patches were tested in the as-built condition; one patch for each direction and labeled as HT0 in this work. The rest of the patches were subjected to three different solution heat treatments and then aged using the same aging heat treatment. The first investigated solution treatment is the standard solution annealing for IN718, which is done at 980°C ± 14 °C for one hour then water quenched, which is labeled as HT1 in this work. The second solution heat treatment investigated held the specimens at 1200 °C for 20 minutes then furnace cooled to 980 °C and held there for 20 minutes before water quenching. This heat treatment is labeled as HT2 in this paper. The third heat treatment we performed included heating the specimens up to 1270 °C, then furnace cooled before solution annealing using the standard solution annealing method. This heat treatment is labeled as HT3. All performed heat treatments were then followed by standard aging heat treatment at 720 °C for 8 hours then furnaced cooled to 620 °C in 2 hours and held at that temperature for another 8 hours followed by air cooling. Table 5.1 lists the patch number, the assigned building direction, the heat treatments, and the number of tested specimens for each patch. The experiment plan follows a full factorial design of experiments to determine the number of samples by investigating all combinations of heat treatments and build orientations. The goal of the testing plan is to capture the influence of the different solution annealing treatments on the samples' mechanical properties, anisotropy, and microstructure.

5.2.2 Specimens preparation

All the IN718 specimens were fabricated on EOSINT M 270 system using the commercialized powder IN718. Table 5.2 lists the weight percentage by the chemical composition of the raw powders we used for fabricating the DMLS IN718 specimens. Table 5.3 lists the processing parameters used during the additive manufacturing of the specimens such as the laser power, scanning speed, hatch spacing, layer thickness, etc. The specimens were fabricated according to the ASTM-E8/E8M [149] with dimensions, as shown in Figure 5.2.

5.2.3 Mechanical proprieties test

To evaluate the mechanical properties of the DMLS fabricated samples of IN718, the authors performed tensile tests on the heat-treated and as-built specimens using an Instron universal testing machine 3369. We carried the test according to the ASTM E8/E8M standard for axial tension tests of metallic specimens. The testing speed was controlled by an extension rate of 0.48 mm/min, which should maintain a strain rate of 0.015/min in the region before yield in the stress-strain

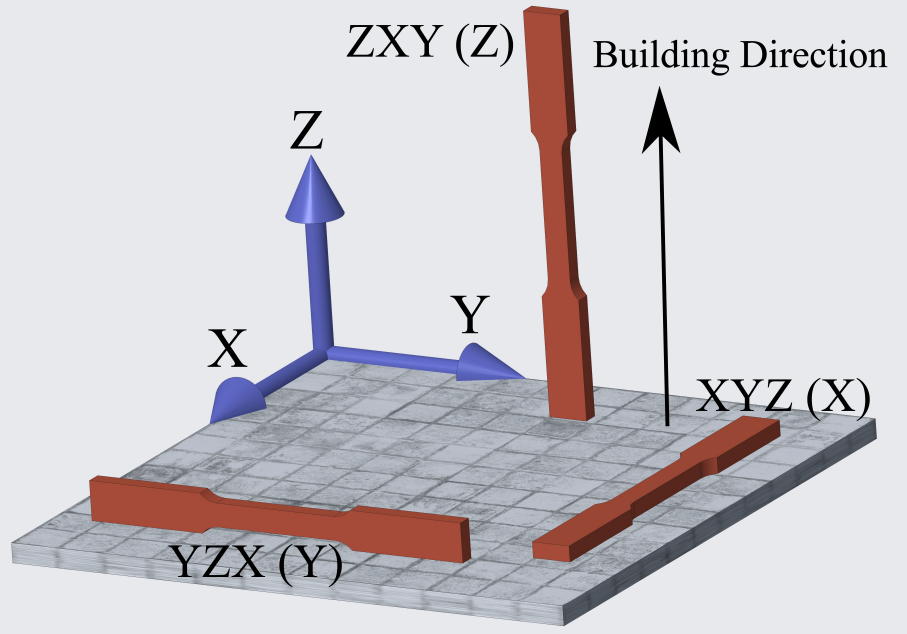

Figure 5.1: The three orientations used in fabricating the specimens

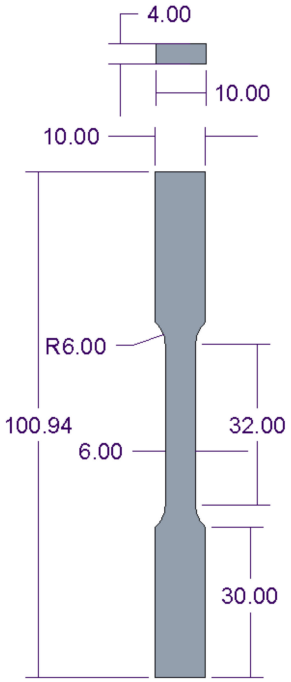

Figure 5.2: The dimensions of the fabricated specimens (all dimensions are in mm)

Table 5.1: IN718 samples and heat treatment specifications

Patch No.	Heat Treatment	Build Direction	Heat Treatment label	Replicas
1	As-built	(X)	HT0 X	3
2	As-built	(Y)	HT0 Y	3
3	As-built	(Z)	HT0 Z	3
4	980 °C for 1 hr then WQ	(X)	HT1 X	3
5	980 °C for 1 hr then WQ	(Y)	HT1 Y	3
6	980 °C for 1 hr then WQ	(Z)	HT1 Z	3
7	1200 °C for 20 min FC to 980 °C and hold for 20 min then WQ	(X)	HT2 X	3
8	1200 °C for 20 min FC to 980 °C and hold for 20 min then WQ	(Y)	HT2 Y	3
9	1200 °C for 20 min FC to 980 °C and hold for 20 min then WQ	(Z)	HT2 Z	3
10	1270 °C for 5 min WQ then 980 °C for 40 min then WQ	(X)	HT3 X	3
11	1270 °C for 5 min WQ then 980 °C for 40 min then WQ	(Y)	HT3 Y	3
12	1270 °C for 5 min WQ then 980 °C for 40 min then WQ	(Z)	HT3 Z	3

Table 5.2: Raw powder chemical composition in weight percentage of the IN718 DMLS Samples

IN718	Ni	Cr	Nb	Mo	Ti	Al	Co	Cu	C	Si, Mn	P, S	B	Fe
wt%	50-55	17.0-21.0	4.75-5.5	2.8-3.3	0.65-1.15	0.20-0.80	1.0 max	0.3 max	0.08 max	0.35 max	0.015 max	0.006 max	Bal

diagram per the ASTM E8/E8M standard. The data collected were time, extension, load, and the strain recorded by an extensometer with a 25 mm gauge length. In addition, a Digital Image Correlation (DIC) system was used during the testing to evaluate Poisson's ratio and observe the breaking patterns and the strain fields associated with them. The DIC system used in this study utilizes two digital cameras that observe the same spot from two different angles, therefore forming a 3D surface of the tested specimens, as can be seen in Figure 5.3. The specimens were painted with white and black patterns to aid the system in measuring the strains as the tensile test progresses. Strains in the vertical (Y) and horizontal (X) directions are measured by tracking the changes in the distances between points aligned in those directions. Distances 1 and 2 are aligned in the X horizontal direction and distance 3 in the Y vertical direction. Two distances are assigned for the X directions to improve the quality of the measurements in this direction due to the smaller

Table 5.3: DMLS processing parameters used to fabricate the IN718 samples

Metal	System	Laser Power	Laser Diameter	Scan Style	Layer Thickness	Inert Gas
IN718	M 290	400 W	100 microns	Alternating Stripes	40 microns	Ar

dimensions associated with these directions as can be seen in Figure 5.3.

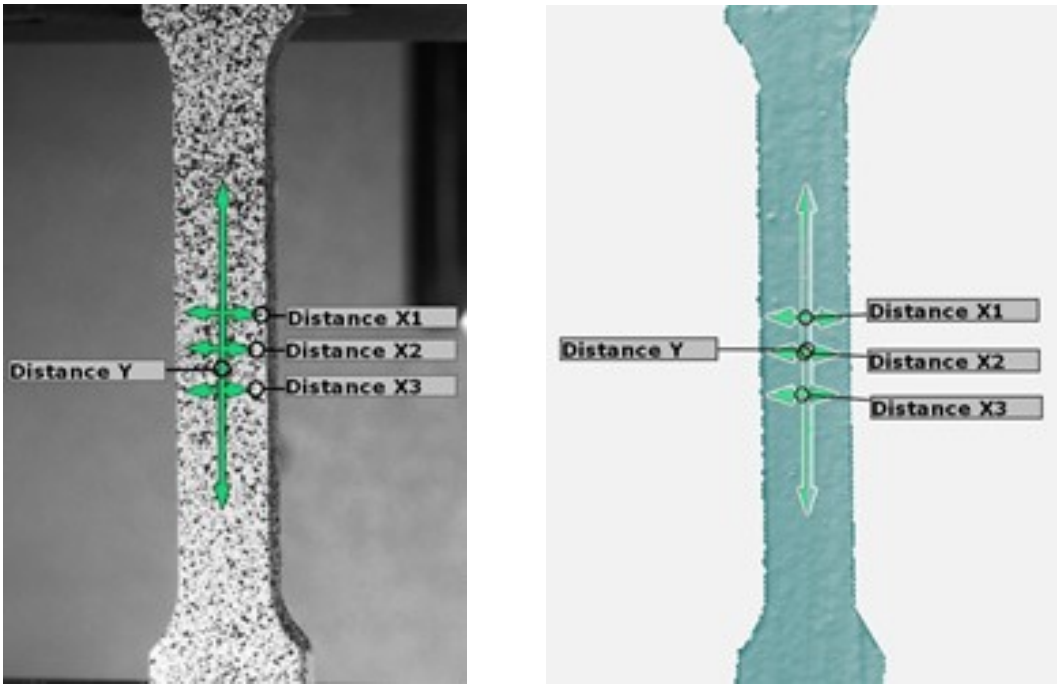

(a) (b)

Figure 5.3: The generated 3D surface using DIC for the tensile specimens. The left image showing the surface imposed on the image of the specimen, while the right image showing the surface by itself.

5.2.4 Imaging analysis

Fractography images of the broken specimens' surfaces were taken using scanning electron microscopy (SEM) to observe the fracture patterns and the presence of porosity and unmolten powder at the surface of the fracture. The microstructure of the as-built and heat-treated specimens were investigated to observe the grain patterns, grain sizes, and the presence of precipitates. The SEM images were taken using a field emission gun SEM-Gemini 500, with Everhart-Thornley secondary electron detector. An acceleration voltage of 3.0 kV for all the images with a working

distance of 3.0-5.5 mm for the microstructure images and 9.4-16.1 mm for the fractography images. The microstructure analysis was done on regions on the specimen's grip section to avoid strain hardening effects on the microstructure. The specimens were cut and mounted in epoxy at room temperature to avoid further exposure to elevated temperature. The specimens were then polished with silicon carbide paper with grit 120 and increased gradually to 1200. Much care was taken not to overheat the samples. Then they were polished using diamond suspensions with particle sizes 1 micron followed by a suspension with particle sizes of 0.25 microns. To reveal the microstructure, waterless Kalling's reagent (2 g CuCl2 + 40 ml HCl + 40 ml methanol) was used. The etchant was applied by swapping for a few seconds up to a minute and then rinsed with deionized water and isopropanol. The microstructure was imaged on the plane that is normal to the tensile force.

5.2.5 X-ray diffraction analysis

Quantitative phase analysis was carried out to aid in explaining the differences in the tensile strength corresponding to different heat treatments. The XRD analysis was done on mirror polished sections of the flat side of the grips of the tensile specimens. The data was collected using PANalytical X'Pert PRO Theta Diffraction system, using a step size 0.002°and starting from 2θ = 20 - 130°with Cobalt target anode of wavelength 1.789 A°. Crystal information files from the inorganic crystal structure database (ICSD) and crystallography open database (COD) were adapted as initial data for the quantitative Rietveld refinement. The analysis included the matrix phase γ, the main strengthening precipitates γ' and γ", in addition to the δ phase precipitates and Laves phase. Table 5.4 lists the initial crystal information of the phases included in the analysis, such as the space group, lattice parameters, and atom positions. Using a predetermined background noise signal, the refinement protocol starts by refining the scale factor, the sample displacement, then the Caglioti coefficients W, V, and U, and finally the preferred orientation. The refinement of the lattice parameters was avoided because of the huge number of parameters required for the refinement, which will reduce the probability of convergence or produce non-physical values only to reduce the sum of squared errors between the calculated spectra and the experimentally observed spectra. Moreover, the lattice parameters used closely match refined data in the literature for IN718 phase quantification, and while the lattice might change due to the different solution heat treatments, the resulting change is marginal [163, 164].

Table 5.4: Crystal information of the phases included in the quantitative XRD analysis

Phase	Space group	Lattice [A°]	Atom	Location	Partial occupancy	Reference code
γ	Fm-3m	a= 3.598	Ni	(0, 0, 0)	0.5	10219-ICSD
			Cr	(0, 0, 0)	0.3	
			Fe	(0, 0, 0)	0.2	
γ'	Pm-3m	a= 3.57	Ni	(0, 0.5, 0.5)	1	58039-ICSD
			Al	(0, 0, 0)	0.63	
			Ti	(0, 0, 0)	0.37	
γ"	I4/mmm	a= 3.62 c= 7.41	Nb	(0, 0, 0)	1	105175-ICSD
			Ni1	(0, 0, 0.5)	1	
			Ni2	(0, 0.5, 0.5)	1	
δ	Pmmn	a= 4.25 b= 5.11 c= 4.54	Nb	(0.25, 1.75, 0.167)	1	COD-1522733
			Ni1	(0.25, 0.25, 0.167)	1	
			Ni2	(0.25, 0, 0.667)	1	
Laves	P63mmc	a= 4.796 c= 15.666	Nb	(0.333, 0.666, 0.563)	1	198050-ICSD
			Fe1	(0.17, 0.34, 0.25)	1	
			Fe2	(0, 0, 0)	1	

5.3 Results and Discussion

5.3.1 Mechanical Properties Test Results

The results of the tensile tests are summarized in Table 5.5, which lists Young's modulus, yield strength, tensile strength, ductility, and Poisson's ratio. These properties were calculated according to each specimens' individual dimensions to avoid variations caused by dimensional errors of the additively manufactured specimens. The influence of the proposed different solution annealing heat treatments on the mechanical properties of DMLS IN718 is better illustrated in Figure 5.4. It shows the relationship between the samples' building orientation and the mechanical properties of as-built specimens (HT0), HT1, HT2, and HT3 heat-treated specimens. Each point showed on the figures is located using the average of the three repeated samples for each testing specimen listed in Table 5.1. Figure 5.4 shows that Young's modulus, the yield strength, the tensile strength, the ductility, and Poisson's ratio of the DMLS IN718 specimens are highly affected by the heat treatment scheme. Generally, all the mechanical properties increased after the solution annealing heat treatments and the aging except for the ductility. Examining Figure 5.4(a), it can be seen that all the solution heat treatments resulted

in a significant increase in Young's modulus for all orientations, especially the Z-built specimens which were significantly lower in the as-built condition (HT0). HT1 resulted in the second-highest modulus for all orientations with HT2 being the highest. HT3 had the third-highest modulus. HT0 had the lowest modulus of elasticity with more than 40 GPa difference compared to the solution annealed specimens. In terms of solution annealed specimens, they all had lower variations in their Young's modulus among the different orientations compared to the as-built condition. It is noticed that the Z-built specimens had significantly lower modulus than the X and Y-built specimens with a difference around 50 GPa, as well. In comparison, the difference in Young's modulus for the solution annealed specimens among different orientations was up to 15 GPa. Results show that the yield strength increased significantly after the solution annealing heat treatments. HT1 showed the highest increase in yield strength with 500 MPa on average, followed by HT3 then HT2 with over 300 MPa increase compared to HT0 as can be seen in Figure 5.4(b). Similarly, the tensile strength increased after the heat treatments, which can be illustrated in Figure 5.4(c). The increase in the tensile strength, however, is less than the one in the yield strength with around 400 MPa for HT1 and 160 MPa for HT2 and HT3. The difference among different orientations for HT0, HT1, HT3 was about 100 MPa for the tensile and yield strengths and about 50 MPa for HT2. It should be noted that while the difference between the X and Y-built specimens is much smaller compared to the difference between them and the Z-built specimens, the X-built specimens had higher stiffness and strength than Y-built specimens in every condition. The ductility of the heat-treated specimens was significantly lower than the as-built specimens as can be seen in Figure 5.4(d). HT1 and HT3 had the lowest ductility with strains ranging between 10-15% at fracture, while HT0 had the maximum ductility with strains ranging between 27-32%. HT2 had the highest ductility among the solution annealed specimens with strains ranging between 16.5-19.0% at fracture. Moreover, we can see that the Z-built specimens have the highest ductility in the ah-built condition and HT1 with the X-built specimens a close second and Y-built specimens showing the lowest ductility. In HT2 and HT3 the variation in the ductility of specimens fabricated in different orientations is reduced and the X-built specimens having slightly higher ductility in both HT2 and HT3. The influence of the heat treatments on Poisson's ratio $v_{xy} = -\frac{d\varepsilon_x}{d\varepsilon_y}$ is presented in Figure 5.4(e). It can be seen that Poisson's ratio for the heat-treated specimens was generally higher than the as-built specimens. In addition, we can see that Poisson's ratio is generally lower for the X-built specimens and that the difference among the different orientations is minimum for HT2, which suggests improved isotropy. Figures 5.5 - 5.8 show the strain fields of tensile specimens just before the fracture. From Figure 5.5 we can see that as-built specimens suffered from high strains before failing. The effect of necking is clear with high strains in the necking area going up to 40% in addition to a large portion of the specimen enduring 20-25% strain as can be seen from the

histograms. HT1 specimens were able to hold significantly less strain before failing and significantly less necking occurred before fracture as can be seen from Figure 5.6. The strain around the necking area dropped to less than 20% for both X and Z-built specimens and about 10% for the Y-built specimens, these results reflect the ductility results in Figure 5.4(d). Also, the strain seems to be more uniformly distributed along the length of the specimens.

HT2 specimens seem to have recovered some of their ductility around 23-29% and slight necking can be observed in Figure 5.7, with more strain concentrated around the failure area. From Figure 5.8 we can see that HT3 strain around the necking area had slightly higher values than HT1, but with less uniform strain distributed along the length of the specimens.

To evaluate the influence of the different solution annealing heat treatments on the anisotropy and repeatability of additively manufactured IN718, an anisotropy index (σ_A) is proposed. The anisotropy index (σ_A) is calculated by taking the standard deviation of the averaged property values for each orientation for a specific heat treatment which means it only calculates the variations of the averaged value for the X orientation, Y orientation, and Z orientation, which are the bar values shown in Figure 5.4, without the error bars. The values for σ_A are summarized in Table 6. The σ_A values indicate that HT2 has the lowest variations in the mechanical properties of specimen fabricated in different orientations for all the mechanical properties except for Young's modulus, where it was a close second after HT1, and for the ductility, where HT2 was a close second after HT3. A similar observation can be made by calculating the standard deviation for all specimens belonging to a specific heat treatment, without averaging them for each orientation before taking their standard deviation. This indicates that HT2 has the lowest anisotropy resulting from manufacturing the specimens in different orientations. In addition to that, HT2 has the highest reliability as the standard deviations for all of the specimens belonging to HT2 showed the lowest variations in their mechanical properties overall.

Table 5.5: Mechanical properties test results for DMLS samples of IN718 materials. Each row results are the average of three repeated specimens

Condition / orientation	Modulus [GPa]	Yield [MPa]	Tensile Strength [MPa]	Ductility [mm/mm]	Vxy
HT0 X-1	161.3	713.2	1039.2	39.01	0.31
HT0 X-2	138.5	696.0	1022.1	27.84	0.32
HT0 X-3	141.1	727.2	1040.1	28.96	0.3
HT0 Y-1	164.8	665.7	991.5	27.32	0.41
HT0 Y-2	128.7	654.5	976.0	27.79	0.43
HT0 Y-3	114.1	647.1	1005.5	27.05	0.39
HT0 Z-1	102.5	580.0	882.9	30.97	0.37
HT0 Z-2	83.1	615.6	930.4	33.63	0.36
HT0 Z-3	84.9	629.3	948.3	34.41	0.39
HT1 X-1	184.8	1208.3	1433.1	13.74	0.25
HT1 X-2	186.4	1214.8	1444.8	14.14	0.25
HT1 X-3	186.8	1216.4	1445.1	13.48	0.3
HT1 Y-1	179.0	1150.5	1361.9	9.07	0.27
HT1 Y-2	185.5	1162.5	1372.3	8.48	0.37
HT1 Y-3	182.5	1154.1	1369	8.86	0.34
HT1 Z-1	174.3	1114.5	1346.7	14.61	0.34
HT1 Z-2	169.1	1102.1	1319.2	14.53	0.37
HT1 Z-3	168.9	1102.0	1329	14.33	0.36
HT2 X-1	189.8	949.2	1203	18.08	0.31
HT2 X-2	196.1	945.2	1207.6	19.17	0.32
HT2 X-3	191.4	1014.8	1248.5	20	0.25
HT2 Y-1	187.6	940.6	1182.2	19.24	0.29
HT2 Y-2	193.6	960.0	1188.6	16.45	0.34
HT2 Y-3	187.2	979.3	1193.8	16.10	0.31
HT2 Z-1	174.6	908.7	1146.8	19.49	0.31
HT2 Z-2	174.4	908.5	1125.5	14.56	0.34
HT2 Z-3	180.3	980.4	1192.1	16.07	0.32
HT3 X-1	189.2	1060.3	1261.0	12.09	0.32
HT3 X-2	186.0	1055.8	1252.7	11.84	0.31
HT3 X-3	186.5	1050.2	1255.6	11.95	0.31
HT3 Y-1	179.0	965.7	1183.2	9.98	0.37
HT3 Y-2	173.1	956.4	1188.0	10.18	0.36
HT3 Y-3	175.5	959.9	1180.1	10.11	0.39
HT3 Z-1	170.9	1044.8	1213.7	11.4	0.4
HT3 Z-2	169.3	1035.2	1201.3	11.51	0.38
HT3 Z-3	171.2	1039.1	1211.4	11.55	0.36

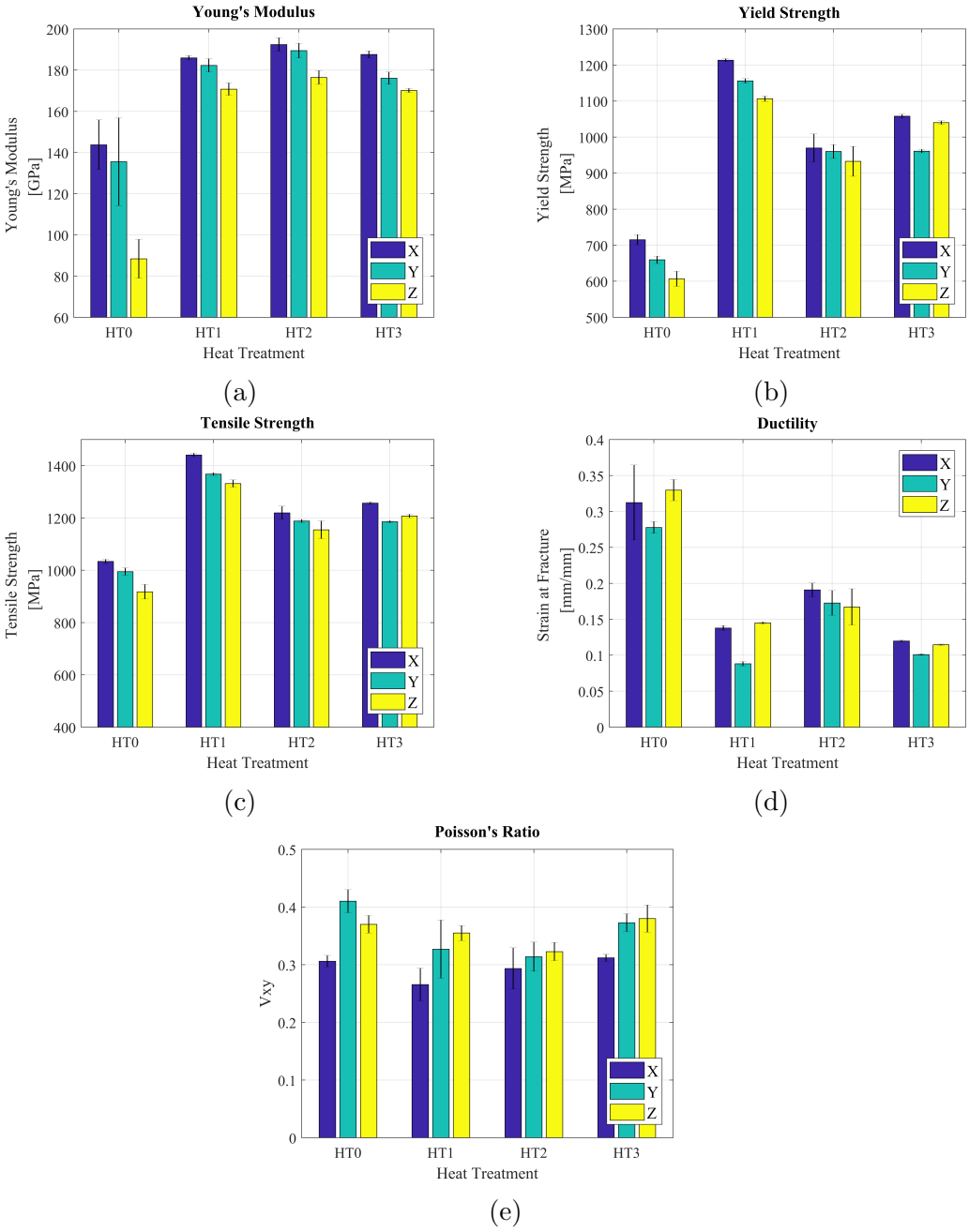

Figure 5.4: Tensile test mechanical properties of DMLS IN718 fabricated in different orientations X,Y, and Z and post processed with different solution annealing heat treatments HT1, HT2, HT3 in addition to the as-built condition HT0. a) Young's modulus, b) Yield strength, c) Tensile strength, d) Ductility, e) Poisson's ratio

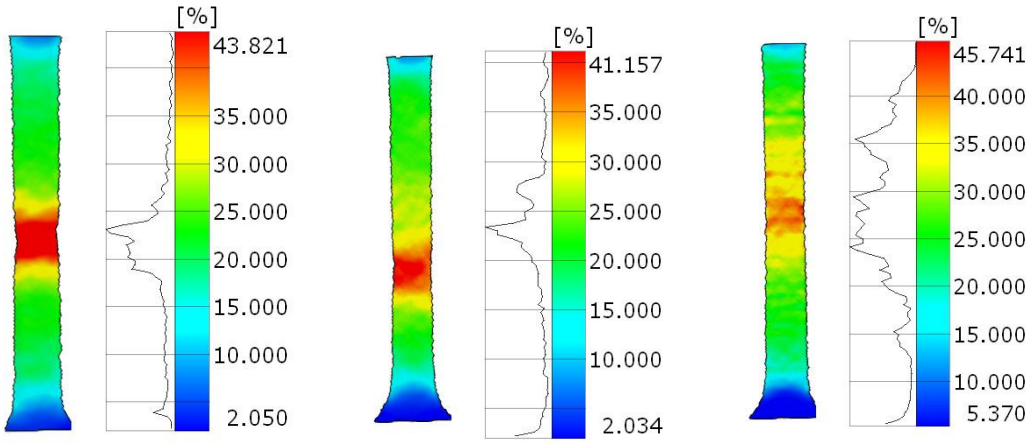

(a) (b) (c)

Figure 5.5: Strain fields of as-built (HT0) DMLS IN718 specimens generated by the DIC system. a) X-built specimen just before fracture. b) Y-built specimen just before fracture. c) Z-built specimen just before fracture.

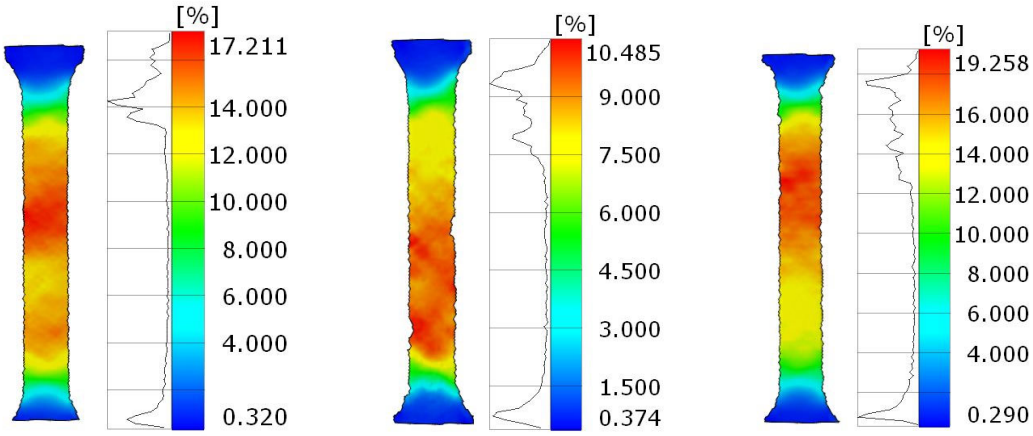

(a) (b) (c)

Figure 5.6: Strain fields of HT1 DMLS IN718 specimens generated by the DIC system. a) X-built specimen just before fracture. b) Y-built specimen just before fracture. c) Z-built specimen just before fracture.

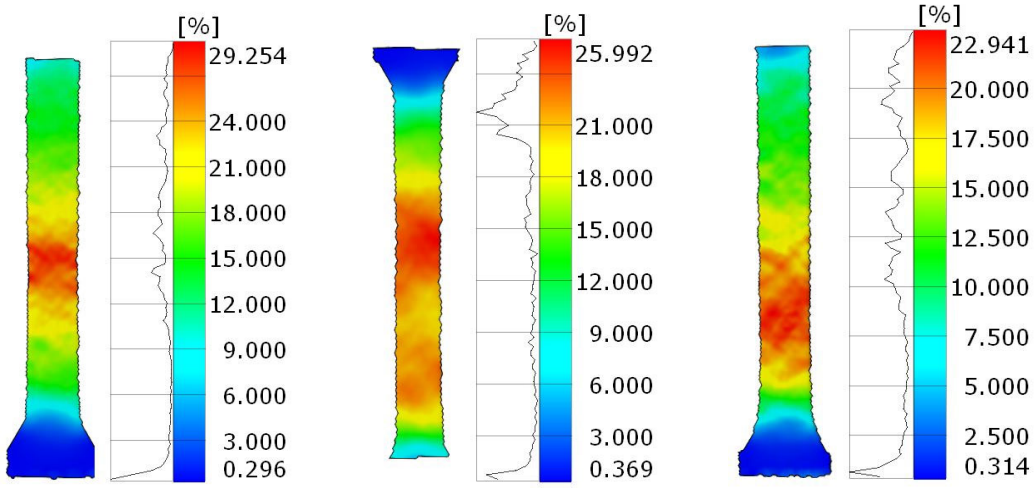

(a) (b) (c)

Figure 5.7: Strain fields of HT2 DMLS IN718 specimens generated by the DIC system. a) X-built specimen just before fracture. b) Y-built specimen just before fracture. c) Z-built specimen just before fracture.

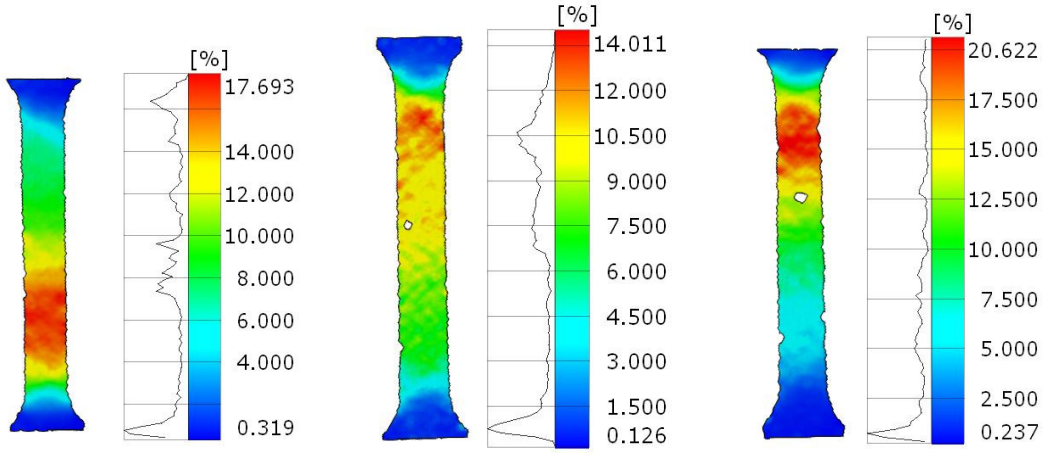

(a) (b) (c)

Figure 5.8: Strain fields of HT3 DMLS IN718 specimens generated by the DIC system. a) X-built specimen just before fracture. b) Y-built specimen just before fracture. c) Z-built specimen just before fracture

Table 5.6: Standard deviation of the resulting mechanical properties for different heat treatments

Heat treatment	Young's Modulus	Yield Strength	Tensile Strength	Ductility	Vxy
	σ_A [GPa]	σ_A [MPa]	σ_A [MPa]	σ_A [mm/mm]	σ_A [dex/dey]
HT0	± 29.87	± 54.26	± 58.88	± 0.026	± 0.052
HT1	± 7.93	± 53.54	± 55.74	± 0.031	± 0.046
HT2	± 8.53	± 19.26	± 32.48	± 0.012	± 0.015
HT3	± 8.89	± 51.59	± 36.50	± 0.010	± 0.037

5.3.2 SEM Fractography

The fractured surfaces of the IN718 specimens are presented in Figure 5.9-Figure 5.12. From Figure 5.9 we can see that the topography of as-built specimens is very prominent and rise high from the surface. Also, from the high magnification images in Figure 5.9(b,d,f) we can see clear topography. No clear distinction in the high magnification fractography can be discerned of the as-built condition of different orientations. For the HT1 and HT2 heat-treated specimens, the fractured surfaces were mostly flat in the center, but had high changes in topograph at the edges as can be seen in Figure 5.10(a,c,e) and Figure 5.11(a,c,e). However, the lips of the HT2 specimens are thicker, describing more ductile fracture than HT1 specimens. The topography observed in the high magnification images of HT1 is more similar to the ones observed in the as-built specimens than in HT2. The HT2 topography in the high magnification images shows wider pools and less deep than in the as-built condition specimens. HT3 specimens' fractured surfaces are almost completely flat, even at the edges. In addition, the holes are more sparse as can be seen in the high magnification images in Figure 5.12(b,d,f), which could be caused by the much lower ductility shown by the HT3 specimens.

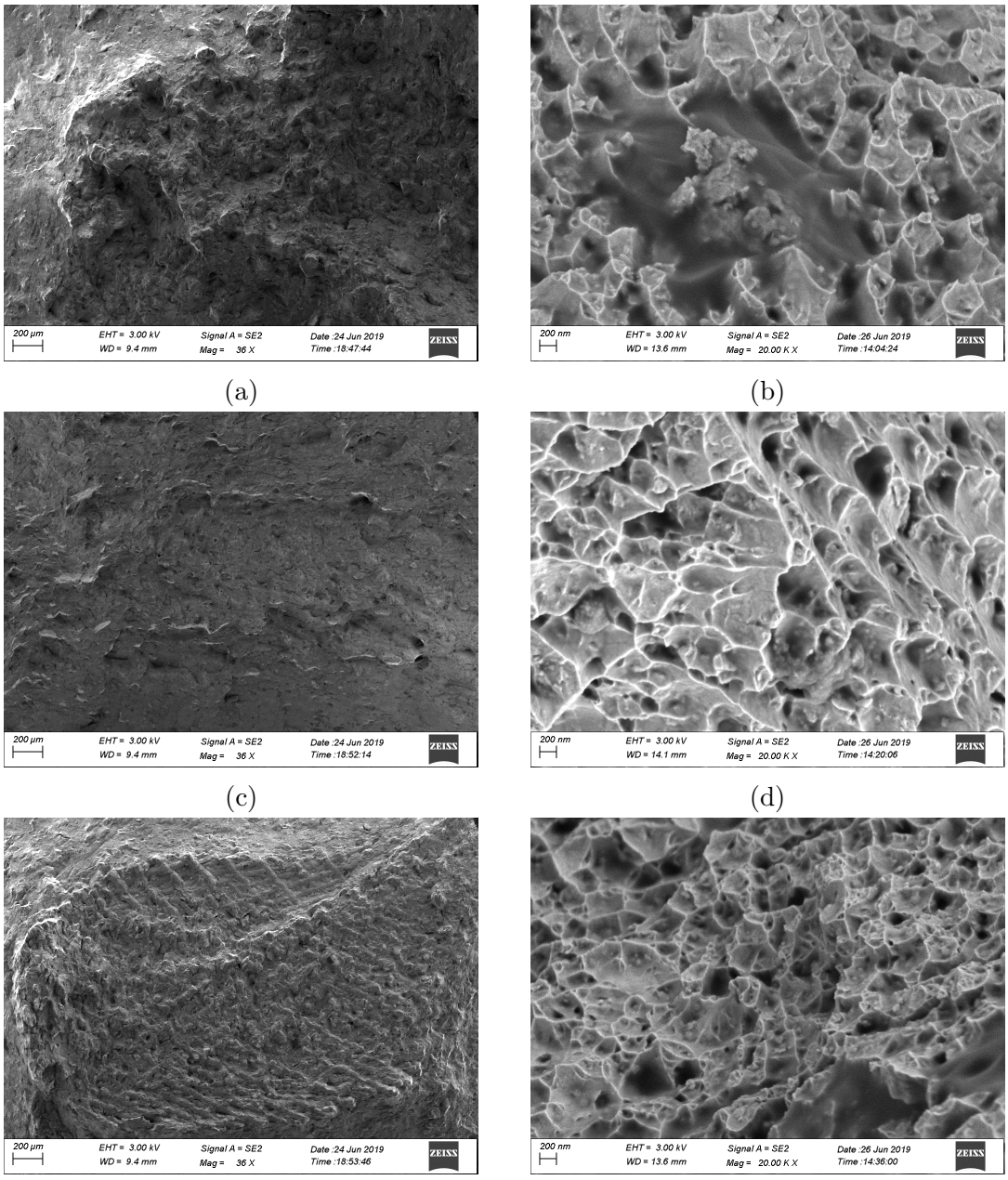

Figure 5.9: SEM fractography of as-built IN718 (HT0). a) X-building direction at 36X magnification. b) X-building direction at 20KX magnification. c) Y-building direction at 36X magnification. d) Y-building direction at 20KX magnification. e) Z-building direction at 36X magnification. f) Z-building direction at 20KX magnification.

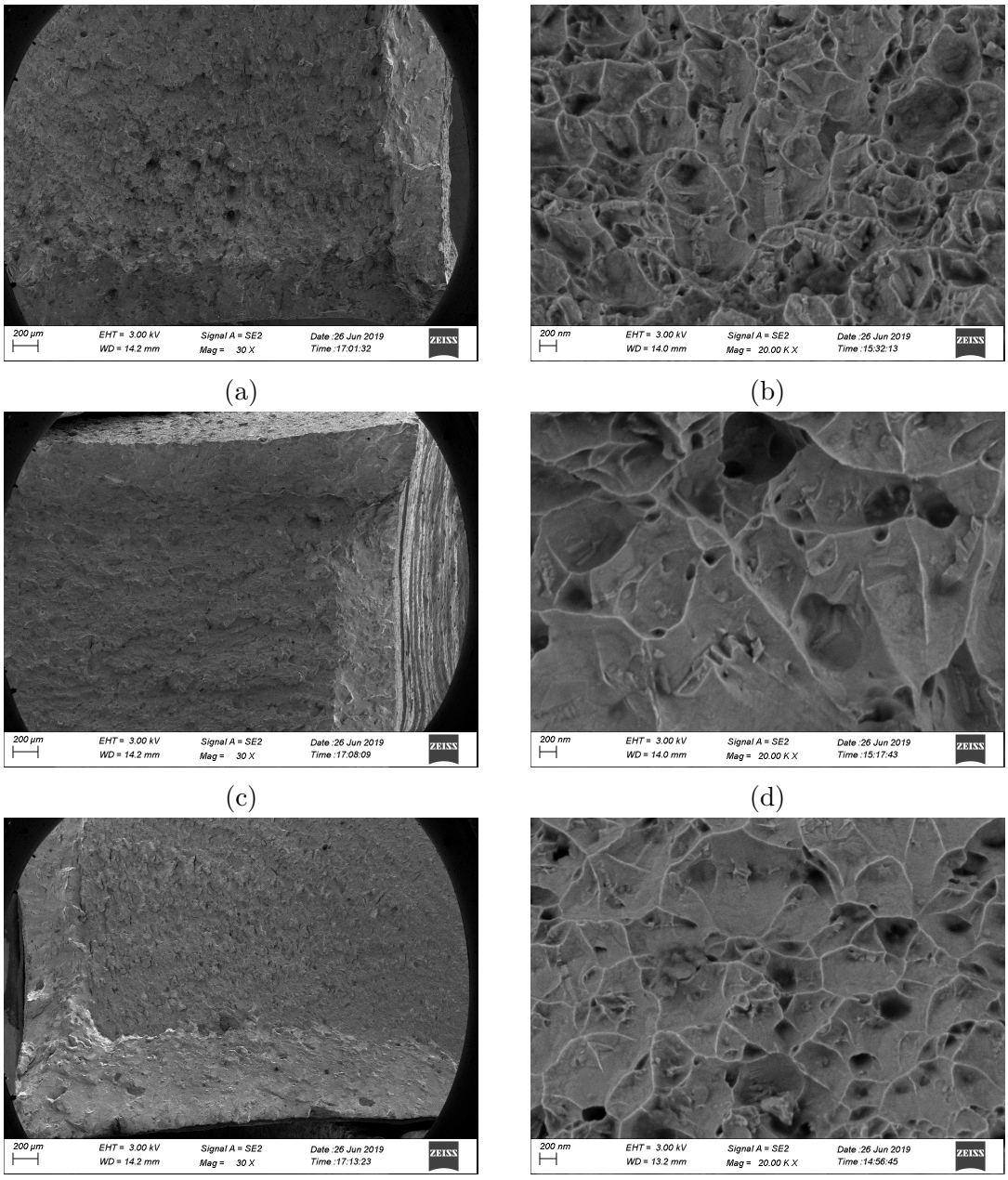

Figure 5.10: SEM fractography of HT1 IN718. a) X-building direction at 30X magnification. b) X-building direction at 20KX magnification. c) Y-building direction at 30X magnification. d) Y-building direction at 20KX magnification. e) Z-building direction at 30X magnification. f) Z-building direction at 20KX magnification.

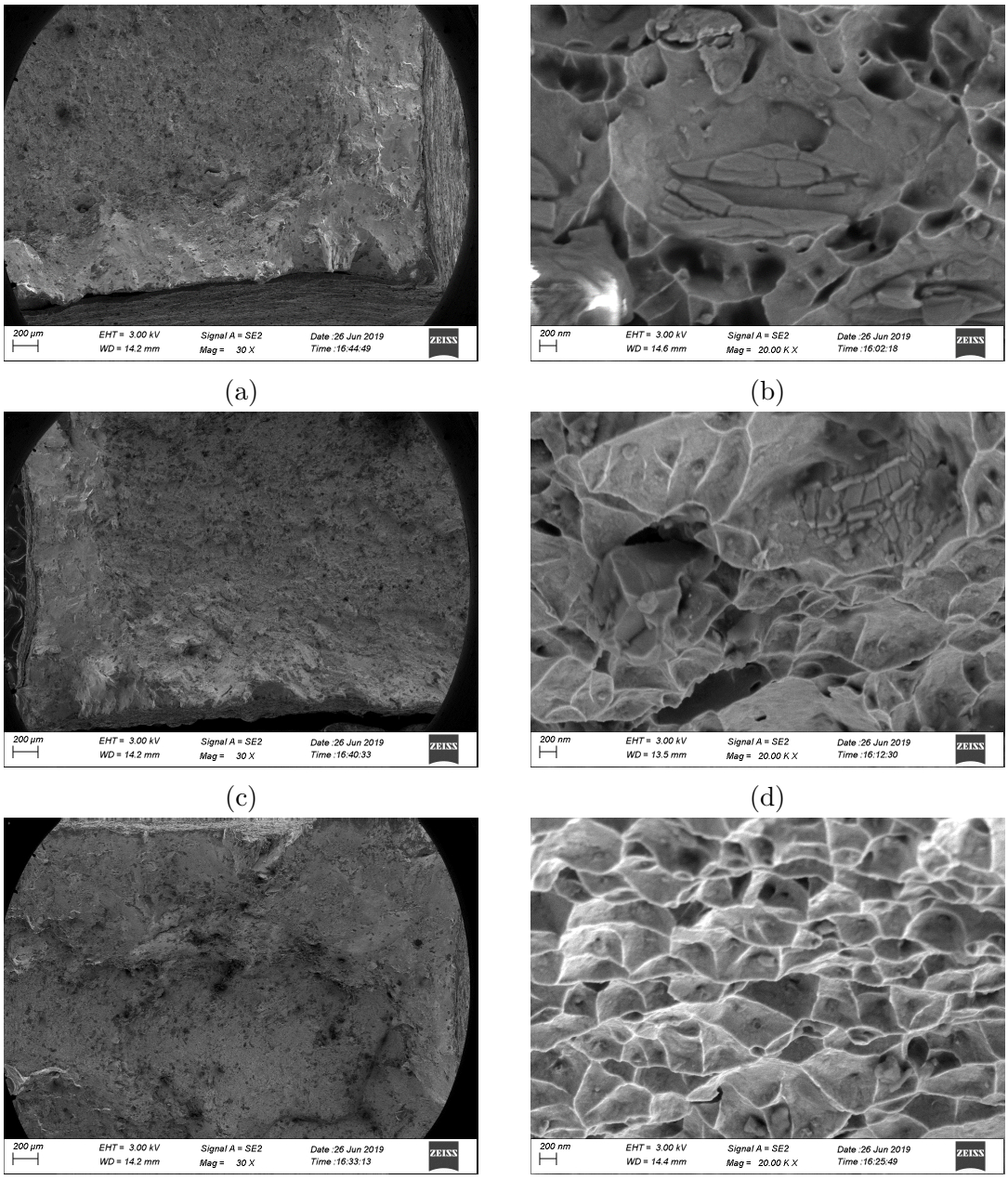

Figure 5.11: SEM fractography of HT2 IN718. a) X-building direction at 30X magnification. b) X-building direction at 20KX magnification. c) Y-building direction at 30X magnification. d) Y-building direction at 20KX magnification. e) Z-building direction at 30X magnification. f) Z-building direction at 20KX magnification.

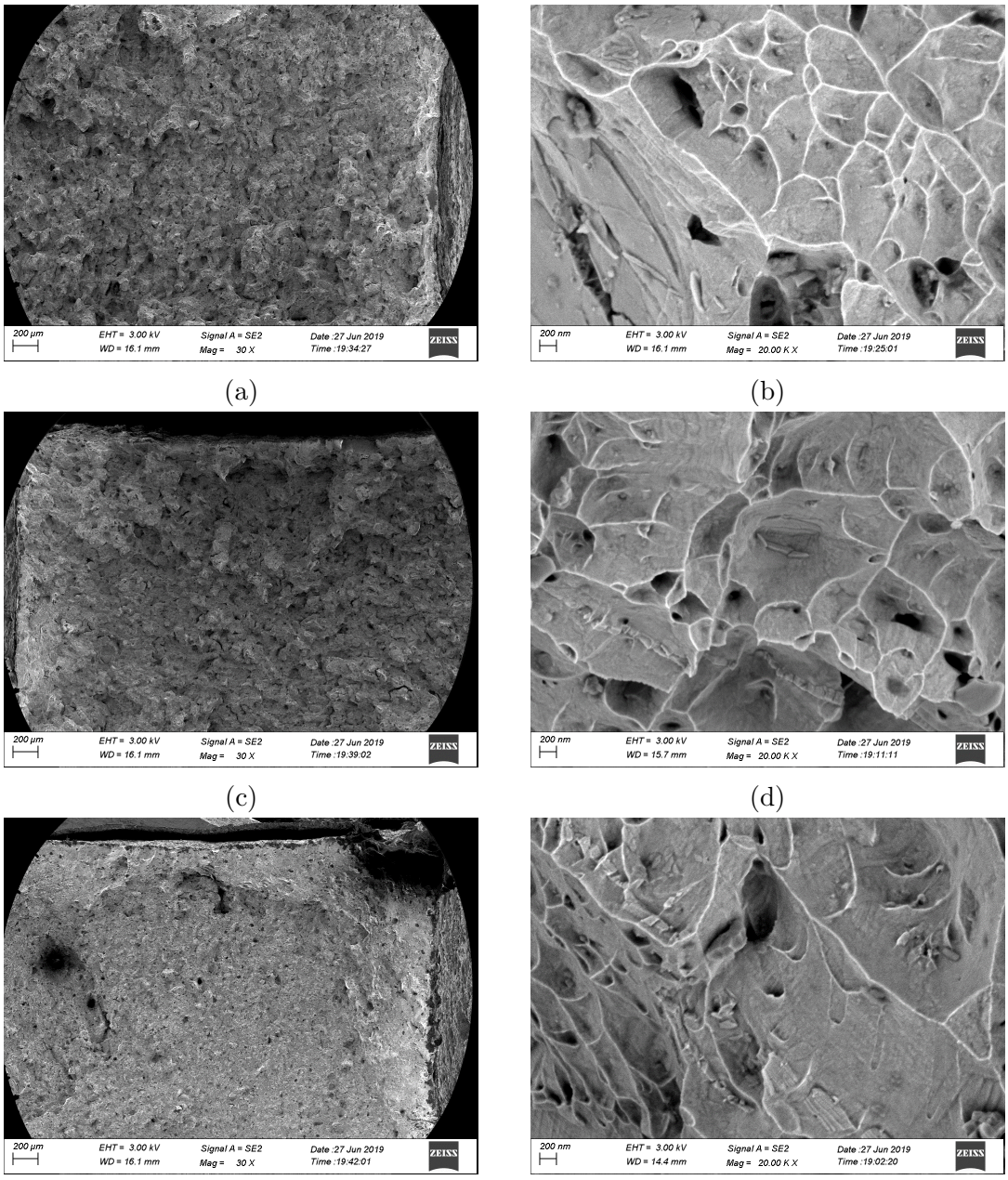

Figure 5.12: SEM fractography of HT3 IN718. a) X-building direction at 30X magnification. b) X-building direction at 20KX magnification. c) Y-building direction at 30X magnification. d) Y-building direction at 20KX magnification. e) Z-building direction at 30X magnification. f) Z-building direction at 20KX magnification.

5.3.3 Microstructure analysis

The microstructure of as-built specimens and heat-treated specimens is presented in Figures 5.13 - 5.17. We can see the effect of the specimens' building direction layer by layer in addition to the fusing of each layer along the laser's scan lines on the microstructure of the as-built specimens. In Figure 5.13(a) the image shows a stack of layers from the bottom to the top, which indicates the building direction. We can also see the cross-section of the overlapping melt pools, which were scanned in a direction out of the plane. The needle-like microstructure can be observed in the X-built specimens. The needle-like microstructure seems to be aligned in some preferred orientations. This can be seen easier in Figure 5.13(b) at 5kX magnification, where small spherical particles are aligned to create the needle-like patterns in the low magnification micrographs. By comparing Figure 5.13(a,b) and Figure 5.13(c,d) we can see that the microstructure on the plane normal to the tensile force for both building directions X and Y share the same pattern. However, the microstructure on the same plane for building direction Z is completely different as can be seen in Figure 5.13(e, f). The top of scan lines can be seen since they are aligned in the plane for the Z-built specimens as opposed to the X and Y-built specimens, where we can only see the cross-sections of the scan lines and melting pools. No needle-like microstructure can be observed on the Z-built specimens, as shown in Figure 5.13(e). Also, the high magnification micrograph of the Z-built specimens Figure 5.13(f), shows that the particles are evenly distributed without preferred orientation, thus eliminating the needle-like patterns.

The similarity in the mechanical properties between the X and Y-built specimens can be explained by the similarity in the microstructure on the planes normal to the tensile force, as observed in Figure 5.13(a, c). On the other hand, the different microstructure pattern developed in the Z-built specimens as shown in Figure 5.13(e) explains the difference in Young's modulus and yield strength displayed by the Z-built specimens compared to the X and Y-built specimens.Texture is one of the most important factors influencing the lattice strain during loading [165].Figure 5.14 highlights the difference in texture between the X and Z-built parts by thresholding the microstructure image to facilitate the estimation of the area fraction of the dendritic γ.

HT1 specimens have shown similar microstructure in the low magnification images to the as-built (HT0) specimens. The melt pools in the X and Y-built specimens can be observed in Figure 5.15(a,c), and the top of the scan lines can be seen in Figure 5.15(e). However, needle-like patterns are not present. The high magnification micrographs show completely different plate-like particles than the ones present in the as-built specimens, as can be seen from Figure 5.15(b, d, and f). These precipitates are one of the strengthening mechanisms of IN718, which resulted in the high yield and tensile strengths of the HT1 specimens. Plate-like particles, that were not observed in the as-built condition, can be seen from Figure 5.15(b,d

and f). The shape and size of these precipitates perfectly match the δ precipitates of IN718. These precipitates appear to be uniformly distributed with orientations of $\pm 45^{\circ}$with respect to the building direction. The difference in the patterns in the low magnification images explains the different mechanical properties of X and Y-built specimens compared to the Z-built specimens.

Figure 5.16 shows the micrographs of HT2 specimens. As can be seen from the low magnification images. In Figure 5.16(a, c and e) the melting pools and laser scan lines are completely replaced by a more homogenous microstructure with defined grain grains. This explains the more isotropic behavior of HT2 specimens. The high magnification micrographs Figure 5.16(b, d, and e) reveal the absence of precipitates even at the grain boundaries, which explains the lower tensile and yield strength of the HT2 specimens compared to the HT1 specimens. HT3 micrographs show similar grains to HT2 specimens; however, with more defined grain boundaries due to the large plate-like precipitates present along the grain boundaries as can be seen in Figure 5.17. The high magnification images in panels b and f show a high abundance of these plate-like precipitates along the grain boundaries. Figure 5.17(d), on the other hand, shows less presence of these precipitates, which explains the slightly lower strength of the Y-built specimens compared to the X and Z-built specimens.

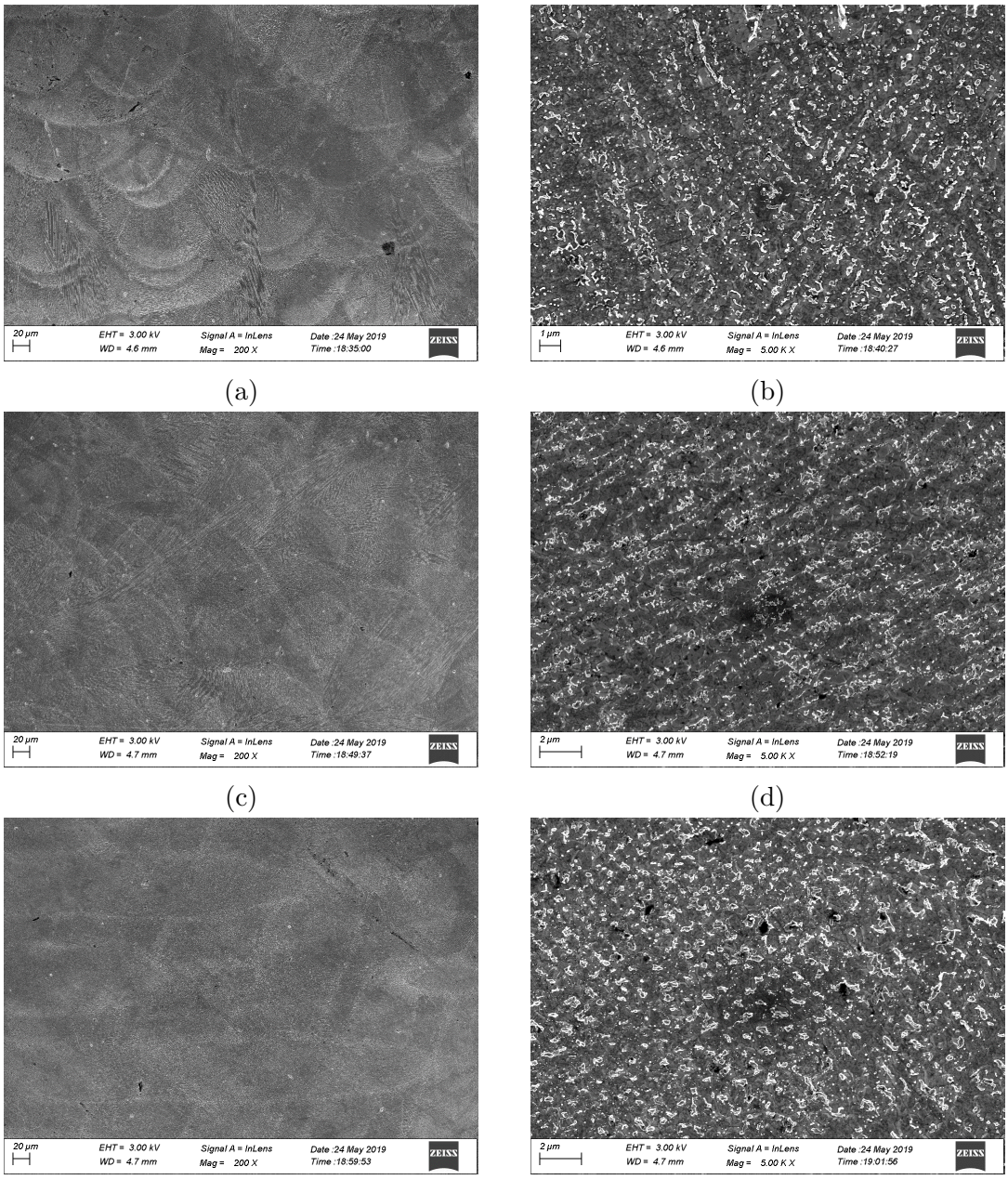

Figure 5.13: Microstructure of as-built DMLS IN718 (HT0) imaged on the plane normal to the tensile force. a) X-building direction at 200X magnification, b) X-building direction at 5kX magnification, c) Y-building direction at 200X magnification, d) Y-building direction at 5kX magnification, e) Z-building direction at 200X magnification, f) Z-building direction at 5kX magnification.

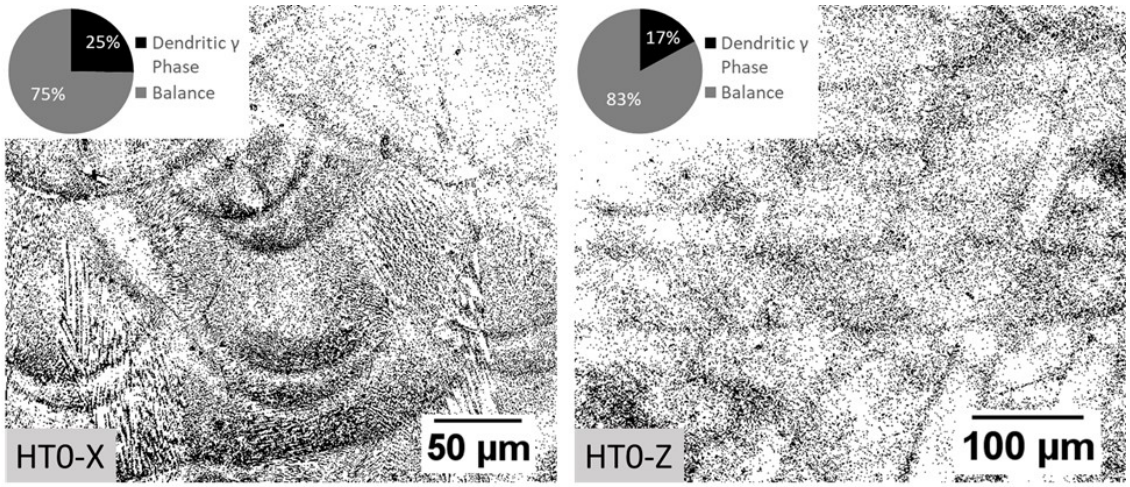

Figure 5.14: Thresholded as-built condition microstructure images highlighting the dendritic γ phase, left X-orientation and right Z-orientation.

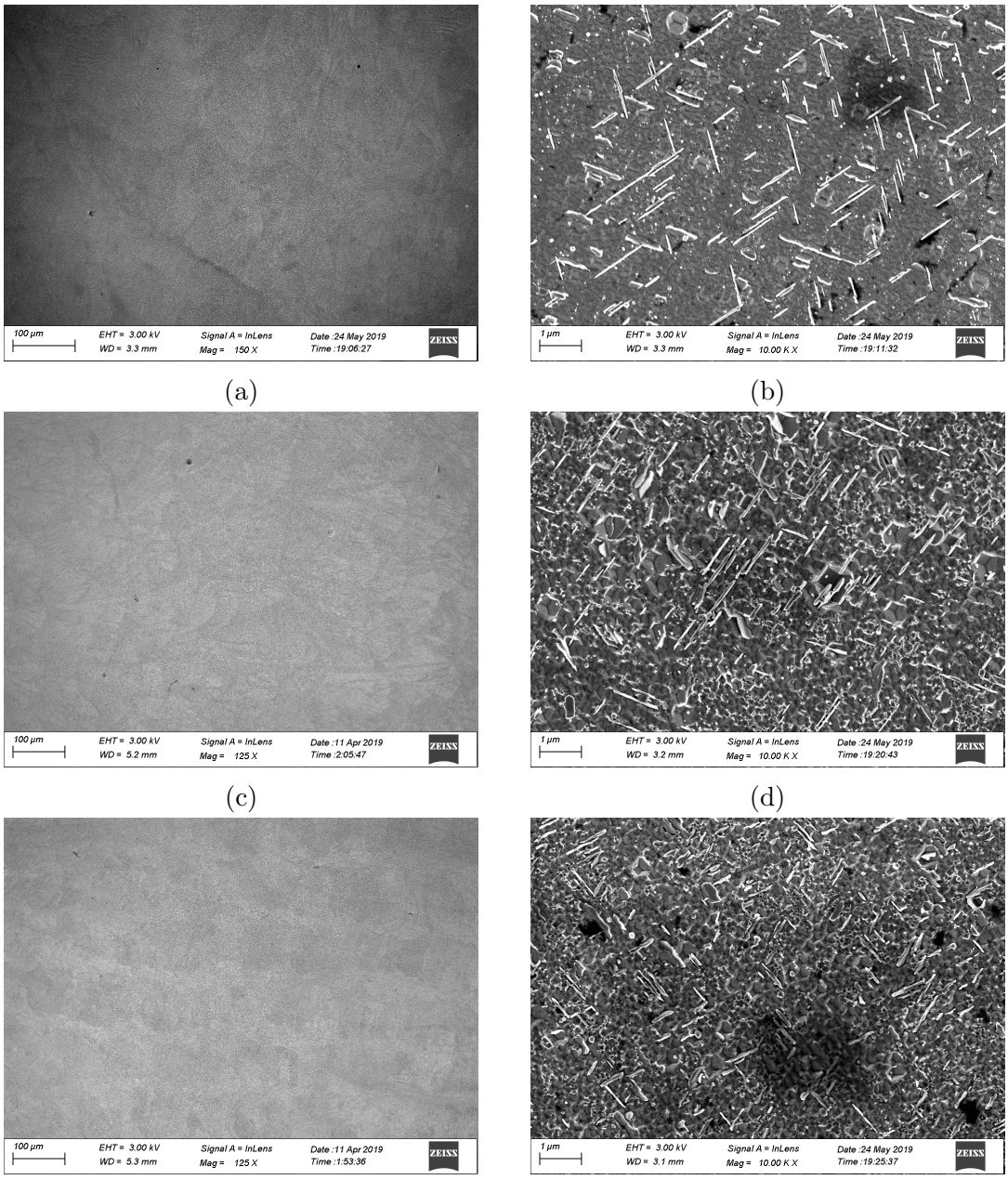

Figure 5.15: Microstructure of HT1 of DMLS IN718 imaged on the plane normal to the tensile force. a) X-building direction at 150X magnification, b) X-building direction at 10kX magnification, c) Y-building direction at 125X magnification,d) Y-building direction at 10kX magnification, e) Z-building direction at 125X magnification, f) Z-building direction at 10kX magnification.

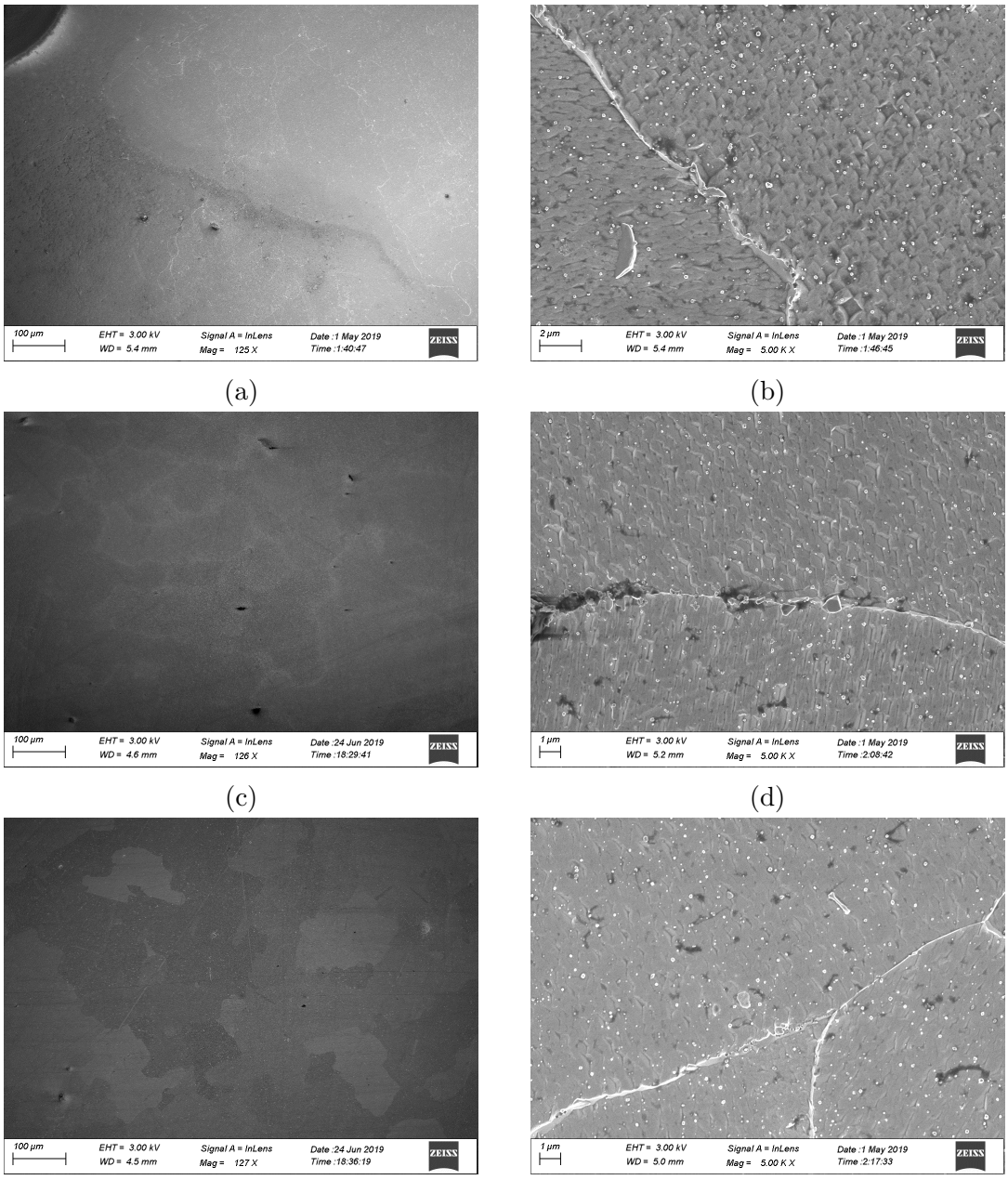

Figure 5.16: Microstructure of HT2 of DMLS IN718 imaged on the plane normal to the tensile force. a) X-building direction at 125X magnification, b) X-building direction at 5kX magnification, c) Y-building direction at 126X magnification,d) Y-building direction at 5kX magnification, e) Z-building direction at 127X magnification, f) Z-building direction at 5kX magnification.

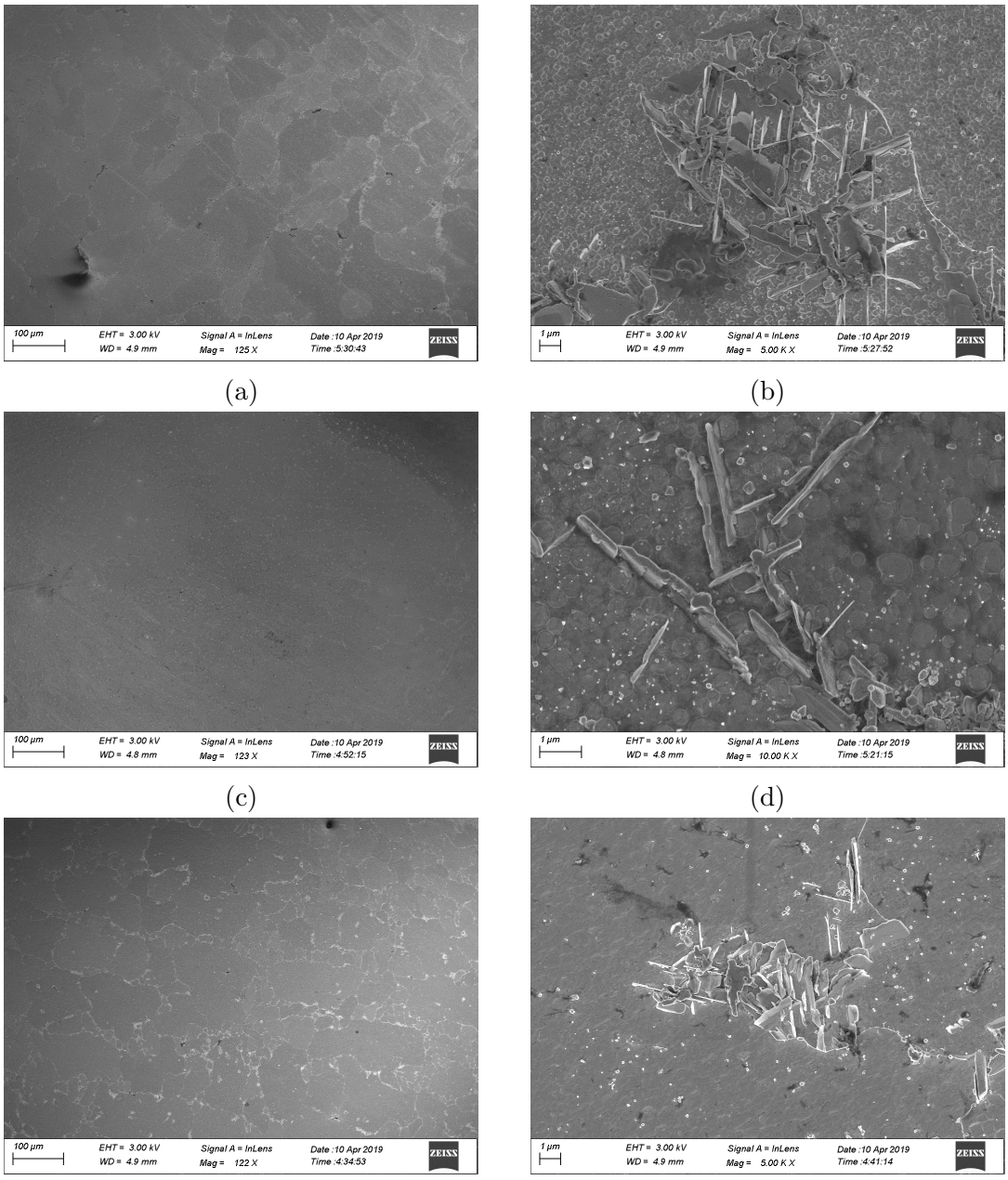

Figure 5.17: Microstructure of HT3 of DMLS IN718 imaged on the plane normal to the tensile force. a) X-building direction at 125 magnification, b) X-building direction at 5kX magnification, c) Y-building direction at 123X magnification,d) Y-building direction at 10kX magnification, e) Z-building direction at 122X magnification, f) Z-building direction at 5kX magnification

5.3.4 XRD quantitative analysis

The Rietveld refinement of the γ, γ', γ'' and δ phases was completed successfully. However, the refinement failed to detect the presence of the Laves phase. Figure 5.18 shows the experimentally observed X-ray spectra, the Rietveld refinement calculated X-ray spectra, and the intensity difference between the observed and calculated spectra for the different heat treatment conditions of the DMLS IN718. The difference plots show that most of the fitting error is caused by the low diffraction angle peaks especially at $2\theta = 51°$which corresponds to the 111 of the matrix phase, which could be due to small changes in the lattice of the phases. The results of the quantitative analysis, in addition to the Rietveld profile fitting indices, are summarized in Table 7. The Rietveld refinement has shown that the as-built condition, HT0, has a minimal amount of precipitates, which included 6% for γ'' and 3.6 for the δ phase. This explains the low tensile strength of HT0. The standard heat treatment has shown a significant amount of γ'' in addition to 3.6% of γ' and the maximum amount of δ precipitates, which explains the increase in the tensile strength. HT2, on the other hand, showed the maximum volume fraction of γ' and small amounts of γ'' and δ precipitates. This increase in γ' explains the improvement in the tensile strength over the as-built condition and due to smaller amounts of γ'' and δ HT2 showed less degradation in its ductility compared to HT1. HT3 showed comparable amounts of precipitates for γ', γ'', and δ phases. This makes HT3 the heat treatment with the highest amount of precipitates overall. This confirms the abundance of the plate-like δ found in the grain boundary of HT3. Therefore, HT3 showed an increase in yield strength over HT2. However, it suffered from low ductility comparable to HT1. This means that the grain boundary δ precipitates acted as stress concentration regions and led to an intergranular fracture. An additional heat treatment, labeled HT4, was explored where the dwelling time of the first step of the solution annealing heat treatment at 1270 °C was increased to 10 minutes instead of 5 minutes with the rest of the heat treatment kept exactly as HT3. The result was a further increase in the δ phase to 18.6% and a decrease in the γ'' precipitates to 8.6%. The γ' remained similar to HT3 with 11.2% instead of 10.3%. The specimens post-processed with this heat treatment performed very poorly and fractured before reaching the yield. The amount of δ precipitates was confirmed by thresholding the SEM micrographs and calculating the highlighted areas. Figure 5.19 shows the thresholded micrographs and the calculated areas occupied by the δ phase. This indicates that the morphology of the δ precipitates has a significant impact on the mechanical properties. The faction volume of the δ phase in HT1 is between HT3 and HT4 but the tensile strength and fracture behavior were significantly different than both, which proves that the different morphology of the δ phase in HT1 is the reason and not just the fraction volume. Increasing the homogenization temperature and increased the growth rate of the δ phase at the grain boundaries. This indicates that depending on the heat treatment, different modes of strengthening

will be involved. Furthermore, if the mode of failure is anticipated during the design process, then proper heat treatment can be chosen.

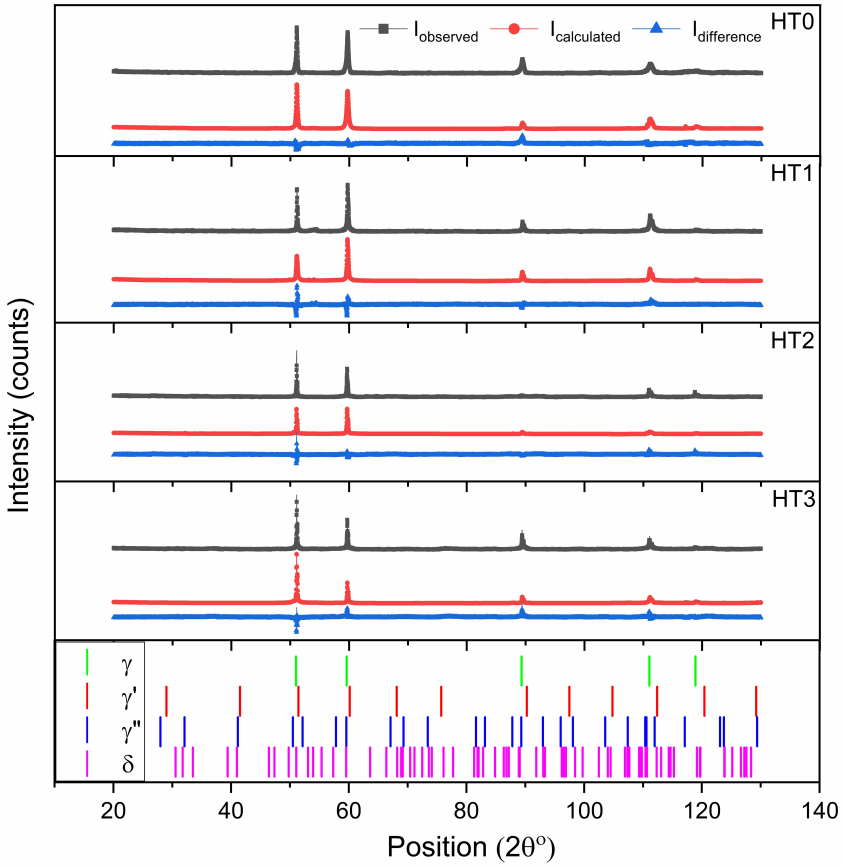

Figure 5.18: Observed and calculated X-ray data using Rietveld refinement for different heat treatments of IN718 using a Co target with a wavelength of 1.789 A°

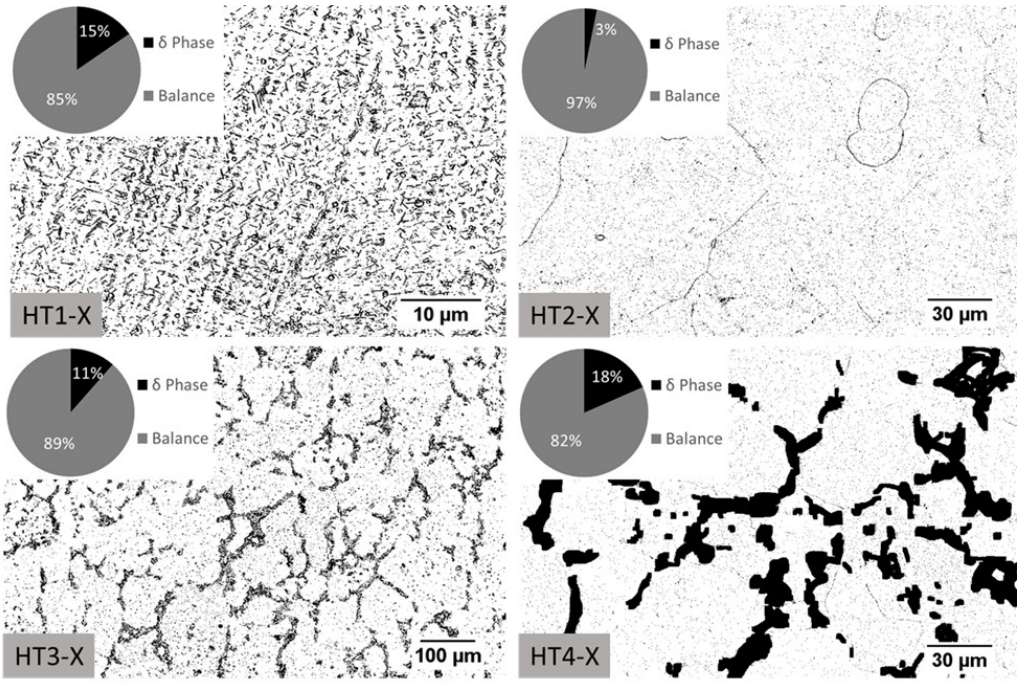

Figure 5.19: Thresholded SEM microstructure images highlighting the δ phase plate-like precipitates area fraction in the heat treated specimens

Table 5.7: Rietveld refinement results summary

Heat treatment	Volume fraction [%]				Rietveld Refinement agreement		
	γ	γ '	γ "	δ	R expected	R weighted	Goodness of fit
HT0	90.4	0.0	6.0	3.6	3.106	6.606	4.523
HT1	71.7	4.4	9.1	14.8	3.118	4.77	2.348
HT2	75.9	16.7	4.6	2.8	3.086	5.885	3.636
HT3	65.9	10.3	12.9	11.0	2.972	6.989	5.529

5.4 Coclusions

In this study, two solution annealing heat treatments were proposed and investigated to understand their influence on the phase composition of precipitates, microstructure, and tensile mechanical properties of the additively manufactured IN718. The as-built condition and standard heat treatment were also investigated

for comparison. To study the effect of the heat treatments on the anisotropy, samples were fabricated in three different orientations, namely X, Y, Z, for each heat treatment. To account for repeatability, three identical specimens were tested for each heat treatment and building direction. This work demonstrated that:

- The mechanical properties such as tensile strength, yield strength, and Young's modulus of as-built DMLS IN718 and standard heat treatment condition depend on the orientation of the specimens, which demonstrates high anisotropy. The microstructure exposed on the surfaces normal to the tensile stress showed different patterns depending on the orientation of the specimen. The similarity in the microstructure in the as-built condition and the standard heat treatment demonstrates the failure of the standard heat treatment to homogenize the microstructure and reduce the anisotropy in the mechanical properties.

- The proposed modifications to the solution annealing heat treatments by including an initial step at 1200 or 1270°C for less than 20 minutes and shorting the duration of the 980°C step to 20-40 minutes instead of one hour resulted in homogenizing the microstructure and making it similar to heat-treated wrought or cast IN718. This reduced the anisotropy and improved the repeatability of the mechanical properties regardless of the specimen's orientation.

- The XRD analysis and Rietveld refinement have proved that changing the solution annealing heat treatment by including an additional step prior to the 980°C has a significant impact on the phases that can precipitate during aging. In the standard heat treatment γ'' is usually 3-4 times the volume fraction of γ' but for additively manufactured IN718 the volume fraction of γ'' was larger than γ' by a factor of 2, in addition to 15% δ. By adding the 1200°C step the volume fraction γ' is four times the volume fraction of γ'' precipitates. This change in the volume fraction of the strengthening phases has shown a good combination of high strength and ductility in comparison to the standard heat treatment which has higher strength but lower ductility. This can be correlated to the volume fraction of the strengthening precipitates, in which γ'' provides superior strength in comparison to γ' but reduces the ductility. Replacing the 1200°C step with 1270°C resulted in a significant increase in the δ phase precipitates in the grain boundaries which resulted in reducing the ductility without significant improvement to the strength.

- This work demonstrates that adding prior heating steps at 1200°C or 1270°C and limiting the dwelling time to 5-20 minutes has proved effective in limiting the grain growth of the microstructure, while effectively homogenizing the microstructure. In comparison, work in the literature has shown significant

grain growth when homogenization is done by increasing the dwelling time to 3 hours or by including a hot isostatic pressing treatment. Furthermore, reducing the duration of the initial step and the 980°C step to 20-40 minutes reduces the energy cost and the total post-processing time.

- Homogenizing the microstructure at 1200°C prior to solution annealing (HT2) is a suitable heat treatment program for parts in low-cycle fatigue application, which requires good ductility and HT2 provides a good combination of strength and ductility. HT1 provides the maximum tensile strength which makes it a suitable candidate for high-cycle fatigue applications.

Chapter 6

MODELING THE EFFECT OF HEAT TREATING DMLS PARTS

This chapter describes the methodology used to model the influence of different post-processing heat treatments on the tensile strength of additively manufactured parts.

6.1 Introduction

Due to the layering nature of additive manufacturing, additively manufactured parts have a unique microstructure and are more susceptible to defects such as trapped gasses and unmolten powder. In addition to that, due to non-uniform cooling additively manufactured parts suffer from residual stresses. These characteristics cause the mechanical properties of as-built additively manufactured parts to be inferior to traditionally manufactured parts []. Heat treatment is a common post-processing technique used to modify the microstructure and mechanical behavior of the material. Post-processing heat treatments of additively manufactured parts have shown great promise in improving their quality and reliability. However, the previous studies presented here demonstrated that additively manufactured parts respond to heat treatments differently compared to their traditional counterparts. This has motivated researchers to investigate modified heat treatments to improve the quality of additively manufactured parts. This demonstrates a need for models that can predict the influence of different heat treatments on the mechanical behavior of additively manufactured parts. This work focuses on Inconel 718 because it is one of the most studied additively manufactured alloys which resulted in producing more data that can be used to model its behavior.

6.2 Physical and Data-based Hybrid Modeling

The tensile strength of heat-treated Inconel 718 is modeled using a hybrid approach that combines known physical models with data-based models. The total tensile strength of Inconel 718 is assumed to be the sum of the strength of the γ matrix phase, the added strength of the grain boundaries, and the precipitates δ, γ', and γ''. The total strength can be written as in Equation 6.1. The following sections will discuss how each of these terms is modeled.

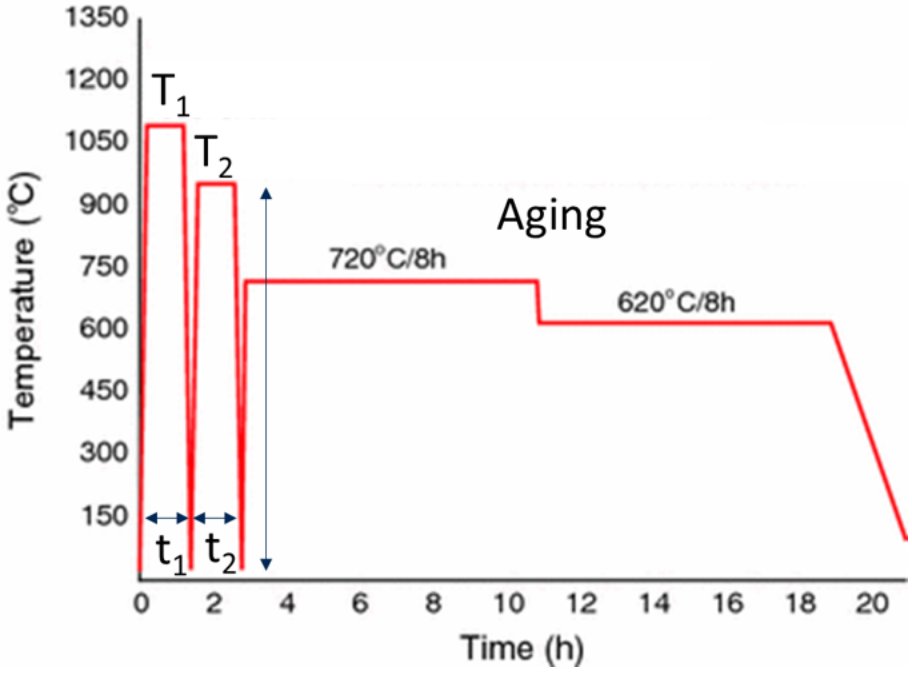

Figure 6.1: Heat treatment parameters

The hybrid model is capable of handling two-step heat treatments, usually, the first step aims to homogenize the microstructure and dissolve undesired phases. The second step prepares the alloy for the precipitation hardening heat treatment. Finally, the model predicts the influence of applying double aging treatment. The heat treatment parameters are described in Figure 6.1. T_1 and t_1 are the temperature and duration of the first step of the heat treatment usually called the homogenization treatment. T_2 and t_2 are the temperature and duration of the second heat treatment and are usually called the solution annealing. Both of the steps are followed by rapid cooling usually water quenching. Finally, the aging step is fixed at 720°C for 8 hours followed by another 8 hours at 620°C. The decision to fix the aging step temperature and duration was made because most of the work in the literature either used the aging parameters described or did not apply the aging step. Therefore, the aging treatment is handled as a switch input parameter that can be either on or off. The model also handles the influence of the part's orientation during the LPBF process in addition to the environment temperature at which the strength of the part is evaluated.

$$\sigma_{tot} = \sigma_{\gamma} + \sigma_{GB} + \sigma_{\delta} + \sigma_{\gamma'} + \sigma_{\gamma''} \tag{6.1}$$

6.2.1 Effect of grain size

The grain size has an inverse relationship with the required shear stress to allow a dislocation to flow $\Delta\tau = \frac{k}{d^x}$. The relationship between the yield strength and mean grain size is described by the Hall-Petch equation in Equation 6.2[]. This means that the x exponent in the previous equation is substituted by x=0.50. The effect of the grain size on the strength σ_{GS} can be written as in Equation 6.3. The grain size d depends on the duration of the heat treatment and the growth rate k which depends on the temperature of the heat treatment T as described in Equations 6.4 and 6.5. The activation energy Q, k_y,gas constant R, and k_0 can be combined and replaced by c_2 and c_3. The added strength due to the grain boundaries is a function of the grain size and can be modeled by knowing the heat treatment's temperature T, time t, initial grain size d_0, and the alloy specific constants n, c_1, c_2, and c_3 as shown in Equation 6.6. In one approach the initial grain size was given the average value reported by different works in literature 100 μm, the second approach was to consider the initial grain size as another adaptive parameter to be learned from the data collected from the literature. The exponent n=2 fits well for pure metals, however, for highly alloyed metals the exponent n is was found to have a significantly lower value [166]. Constants c_1, c_2, and c_3 are model parameters.

The grain size is highly affected by the thermal history of the part. However, the aging heat treatment temperature is low enough to ignore its effects on the grain size, and only the homogenization and solution annealing heat treatments are considered for modeling the grain size effect on the tensile strength.

$$\sigma_y = \sigma_0 + \frac{k_y}{\sqrt{d}} \tag{6.2}$$

$$\sigma_{GS} = \frac{c_1}{\sqrt{d}} \tag{6.3}$$

$$d^n - d_0^n = kt \tag{6.4}$$

$$k = k_0 exp\left(\frac{-Q}{RT}\right) \;\rightarrow\; k = c_1 \exp\left(-\frac{c_2}{T}\right) \tag{6.5}$$

$$\sigma_{GS} = \sigma_{GS}\left(d\right) = \sigma_{GS}\left(T, t, c_1, c_2, c_3, d_0, n\right) \tag{6.6}$$

6.2.2 Effect of δ precipitates

The strengthening effect of precipitates in an alloy depends on the size and distance between the precipitates. If the precipitates are relatively small or distributed closely, the dislocations flow by cutting the precipitates. If the precipitates are large and strong or sparsely distributed in the matrix, dislocations flow by bowing the dislocation line around the precipitates. The strengthening effect of the

precipitates depends on the dislocation flow mechanism as described by Equation 6.7.In this equation, r is the radius of the precipitates and r_c is the critical precipitate radius at which the dislocation flow mechanism changes. The size of the precipitates and their number density in the matrix is a function of the temperature since it affects the diffusion rate of the Nb atoms and the duration of the heat treatment as it controls the time for the precipitates to grow. The growth rate of the precipitates can be described by Equation 6.8. The rate of nucleation can be described by Equation 6.9. By combining these equations the volume fraction of the precipitates can be evaluated.

Furthermore, the strength contribution by the precipitates is a function of the volume fraction of the precipitates. The volume fraction can be predicted by Avrami's equation as described in Equation 6.10, where the time exponent n_δ ranges between 1-4 depending on the shape of the precipitate, and k_v is the precipitation rate and takes the form of Equation 6.5.

Finally, the strength of the δ precipitates can be modeled by Equation 6.11, a simplified version of the equation used in [167], where the first term accounts for cutting strength and the second term accounts for Orowan bowing strength.

$$\sigma_{bowing} \propto \frac{1}{r} \;\; for \;\; r < r_c \qquad \sigma_{cut} \propto \sqrt{r} \;\; for \;\; r > r_c \tag{6.7}$$

$$r \propto exp\left(\frac{-b_1}{T_1}\right) \cdot \left(1 - \exp\left(\frac{-b_2}{T_1}\right)\right) \cdot t_1^n \tag{6.8}$$

$$I_{nuc} \propto b_3 \exp\left(\frac{b_4}{T_1}\right) \cdot \exp\left(\frac{-b_5}{T_1\left(T_m - T_1\right)^2}\right) \tag{6.9}$$

$$f_\delta = 1 - exp(-k_v t^{n_\delta}) \tag{6.10}$$

$$\sigma_\delta\left(C_{cut}, C_{bow}, b_1, b_2, b_3, b_4, b_5, n_\delta, t, T\right) = \sigma_\delta = C_{cut1} f_\delta^{C_{cut2}} r_\delta^{0.5} + \; C_{bow1} f_\delta^{C_{bow2}} \tag{6.11}$$

6.2.3 Effect of γ'' and γ' precipitates

The strengthening effect of γ' and γ'' take similar forms to the δ precipitates. However, since most of the data from literature used the same precipitation heat treatment, the influence of the aging heat treatment on the precipitation of γ' and γ'' can be modeled as a switch factor (on or off). This switch factor, however, does not take into account the influence of the homogenization and solution annealing heat treatments. In addition to that, γ'' and δ precipitates share the same chemical composition. This means that some of the alloying atoms necessary to form the γ'' precipitates may be consumed during the solution annealing heat treatment to form the δ precipitates. Furthermore, the grain size and the distribution of the alloying

atoms are influenced by the homogenization and solution annealing heat treatments, which may have an impact on the diffusion and precipitation of the γ' and γ'' during the precipitation (aging) heat treatment.

In this work, the effect of the homogenization and solution annealing heat treatments on the γ'' growth rate during aging is modeled by Equation 6.12. Since prior knowledge of the influence of the solution annealing heat treatment duration and temperature on the aging heat treatment precipitation rate is limited the constant $C_{\gamma''}$ and time exponent $n_{\gamma''}$ were allowed to take values from negative infinity to positive infinity. The volume fraction of the γ'' was also adjusted by the volume fraction already taken by the δ phase. Therefore, the γ'' contribution to the tensile strength of IN718 due can be modeled by Equation 6.13, which takes into account strength due to Order and Coherency (Orowan bowing is negligible [168]). The $1.1 - f_\delta$ multiplier is added to account for the amount of alloying atoms consumed in the δ precipitates, and Age is the switch factor that indicates whether the aging heat treatment was applied or not.

Similar to γ'', the strength contribution of γ' precipitates takes the form of Equation 6.14 without the volume fraction correction factor since γ' does not sure the same chemical composition as the δ precipitates.

$$R_{\gamma''} = R_{\gamma''_0} \cdot exp\left(\frac{-C_{\gamma''}}{T}\right) \cdot t^{n_{\gamma''}} \tag{6.12}$$

$$\begin{aligned} &\sigma_{\gamma''}\left(t, T, C_{\gamma''_{cut}}, C_{\gamma''_{bow}}, f_\delta, Age, C_{\gamma''}, n^{\gamma''}\right) \\ &\quad = \left(a_1 \left(f_{\gamma''} R_{\gamma''}\right)^{0.5} - a_2 f_{\gamma''}\right) \cdot Age \\ &\quad = a_1 \left(\left(1.1 - f_\delta\right) \cdot R_{\gamma''}\right)^{0.5} - a_2 \left(1.1 - f_\delta\right) \cdot Age \end{aligned} \tag{6.13}$$

$$\sigma_{\gamma'}\left(t, T, C_{\gamma'_{cut}}, C_{\gamma'_{bow}}, Age, C_{\gamma'}, n^{\gamma'}\right) = \left(a_1 \left(f_{\gamma'} R_{\gamma'}\right)^{0.5} - a_2 f_{\gamma'}\right) \cdot Age \tag{6.14}$$

6.2.4 Effect of preferred orientation

Due to the layering nature of laser-based additive manufacturing, a temperature grandaunt usually develops parallel to the building direction. This temperature gradient affects the preferred orientation of the grains in addition to the growth direction of the γ dendrites. This affects the effective grain size of the matrix γ in direction of loading. This intern has an impact on strength of the part depending on the angle between the loading vector and the building direction.

To model the influence of the part's orientation during the LPBF process, two angles that describe the part's orientation are proposed as inputs. The first angle, θ, describes the angle between the width of the specimen and the substrate (build plate). The second angle, ϕ, describes the angle between the length of the part and the substrate.

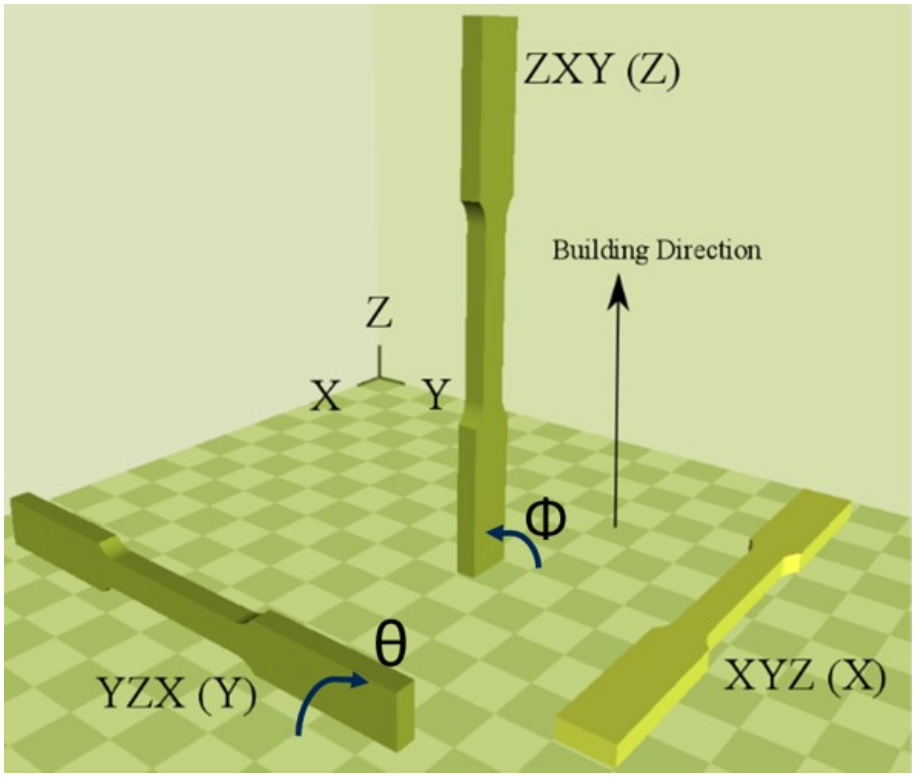

Figure 6.2: Two input angles describing the part's orientation during the LPBF

The proposed model uses sinusoidal functions multiplied by the intrinsic strength of γ and the grain boundary contribution to the strength as described in Equation 6.15. The constants $C_{\theta 1}$ and $C_{\phi 1}$ describe the significance of the input angles θ and ϕ respectively, while $C_{\theta 2}$ and $C_{\phi 2}$ are phase shift constants to allow the model more degrees of freedom. The exponential term at the end of Equation 6.15 is added to evaluate the dampening impact of the homogenization and solution annealing heat treatments on the anisotropy.

$$\sigma_{\gamma_{adj}} = (\sigma_\gamma + \sigma_{GB}) \cdot [1 + (C_{\theta 1} \sin(\theta + C_{\theta 2}) + C_{\phi 1} \sin(\phi + C_{\phi 2})) \cdot \exp(c_{or} T)] \quad (6.15)$$

6.2.5 Effect of environmental temperature

Inconel 718 is a Nickel superalloy suitable for applications with environmental temperatures up to 600°C. At environmental temperatures higher than 600°C the γ'' precipitates start transforming to the more stable phase, δ. In addition to that, the elevated temperature reduces the energy required for dislocations to move which reduces the strength of the alloy. Therefore, it is important to evaluate the influence

of the environmental temperature in combination with the different heat treatments which influence the significance of each of the strengthening mechanisms.

Several models were investigated, however, the model shown in Equation 6.16, a modified version of the Johnson-Cook model [169], was chosen due to its ability to handle normalized values of strength. The strength $\sigma_{Elevated}$ represents the strength contribution of a phase at the environmental temperature $T_{Environment}$, where σ_{Room} represents the strength contribution of the phase at room temperature, T_m the solvus temperature of the phase, and C_{ev1} and C_{ev2} are model parameters.

$$\sigma_{Elevated} = \sigma_{Room} \cdot exp\left(-C_{ev1}\left(\frac{T_{Environment} - T_{Room}}{T_m - T_{Room}}\right)^{C_{ev2}}\right) \tag{6.16}$$

6.3 Methodology

Physics-Data driven hybrid modeling requires data to train the model and evaluate the model's constants. The data was collected from relevant work in literature [82, 83, 112, 170–182]. The data was also complemented by experimental data presented in this dissertation. The total number of independent data points used to train the model is 97. The model has 33 constants that need training. This implies that 33 carefully selected data points should be sufficient to train the model. Using the design of experiment practice would be an efficient method to accomplish this. However, due to the cost of PBF, the data was collected from the literature. Furthermore, since the data was collected from different publications in literature, the tensile strength of the heat-treated specimens was normalized by the tensile strength of the as-built condition reported in that publication. This was done to reduce measurement errors, variance due to the specimens' shape and size, and tensile testing settings.

The least-square error algorithm was used to train the model and evaluate the constants. The error minimization problem has proved to be non-convex with multi-local minimum points. To avoid non-physical values for the constants, constraint conditions were applied to the optimization problem. The intrinsic strength of annealed γ phase σ_γ, Hall-Petch constant ky Equation 6.2, and all Arrhenius equations constants Equation 6.8, were constrained to positive values. The time exponent for the δ precipitate size models and Avrami equations 6.8-6.10 were also constrained to positive values. Due to the limited information about the effect of the solution annealing and homogenization heat treatments on the precipitation during the aging treatment, the time exponent in Equation 6.12 was allowed positive and negative values to explore the effect of the solution annealing heat treatment more thoroughly. The coefficients of the cutting and Orowan bowing strengthening effects due to precipitates C_{cut}, C_{bow} in Equations 6.11, 6.13, and 6.14 as well as constants

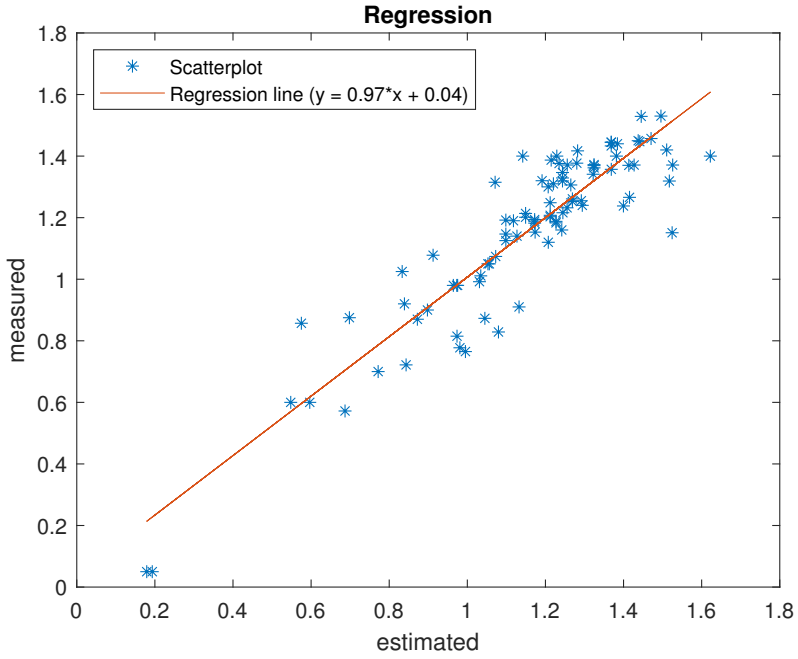

Figure 6.3: Regression correlation plot

C_{ev1} and C_{ev2} in Equation 6.16 were constrained to positive values. No constraints were placed on the constants in Equation 6.15.

The constrained least square error minimization problem resulted in a fitness index $R^2 = 0.88$, which was considered acceptable considering the scarcity of data and the fact it was collected from different publications in the literature. Figure 6.3 demonstrates the correlation plot of the model with observed data. In comparison, an unconstrained minimization resulted with $R^2 = 0.9$, this demonstrates that the model does not have sufficient degrees of freedom and more complex models of the precipitation strength might be necessary. However, due to the limited data, simpler versions of these equations were adopted in this work.

6.4 Results and Discussion

6.4.1 Effect of homogenization

The influence of the temperature and duration of the homogenization heat treatments are illustrated in Figures 6.4-6.8. The model demonstrates that the strength of fully annealed IN718 is around 355 MPa. This value is lower than the reported value in [183] for annealed IN718 with coarse grains with a tensile strength of 524 MPa. The strength added due to the grain boundaries ranges between 120

MPa and 200 MPa. From Figure 6.4 it can be seen that at higher elevated temperatures less time is required to increase the grain size significantly resulting in a reduction in the grain boundary contribution to the tensile strength. The Hall-Petch coefficient reported by the model is $K_{Hall-Petch} = 882.4$ MPa $\cdot \mu m^{1/2}$, which is comparable to values reported in [168] (710 MPa $\cdot \mu m^{1/2}$). The larger value reported by the model could be explained due to not including dislocation density in the analysis. Additionally, the time exponent in Equation 6.4 was found to be $n = 0.19$ which is in the range reported by [166] (n=0.067-0.206) with the exponent increasing toward the upper range at higher temperatures in the range 1050-1200 K in which homogenization and solution annealing are usually performed.

The influence of the homogenization heat treatment on the strength contribution by the γ' appears to be negligible as can be seen by Figure 6.5. However, it could be that the effect of homogenization heat treatment on the γ' strength is hidden and included in either the γ" or the δ strength contribution. More data might be needed to de-confound the effects.

Figure 6.6 show that the homogenization heat treatment has an impact on the strength contribution by γ". The model shows that the strength decreases slightly as the duration of the homogenization heat treatment increases. This could be due to the increase in the δ volume fraction which depletes the alloying atoms required to precipitate γ". The temperature appears to have a limited effect in the window of homogenization and solution annealing heat treatments.

The duration of the homogenization heat treatment has a significant impact on the tensile strength contributed by the δ phase. At most homogenization temperatures the maximum strength increase to the IN718 alloy appears after 25 minutes of homogenization. The maximum contribution appears at 1200 °C and 25 minutes. After 55 minutes, however, a significant drop in strength is observed. At lower temperatures, the drop in strength is observed earlier only after 35 minutes as can be seen in Figure 6.7. The time exponent n_δ in Equation 6.10 was found to be $n_\delta = 0.34$. This value is smaller than the values expected for the Avrami exponent were usually $1 < n < 4$. However, it matches well with reported values in the literature focused on the precipitation kinetics of the δ phase in Inconel alloys [184, 185]. It should be noted that the precipitation mechanism of the δ phase is controlled by the diffusion rate of Nb in the matrix γ therefore non-integral values for the exponent n are expected.

The total influence of the homogenization heat treatment on the tensile strength is illustrated in 6.8. The surface plot shows that the combined effect of the grain boundary, γ", and δ strengths results in the strength reaching a maximum value after 30 minutes of homogenization. The value of the maximum strength decreases as the temperature increases.

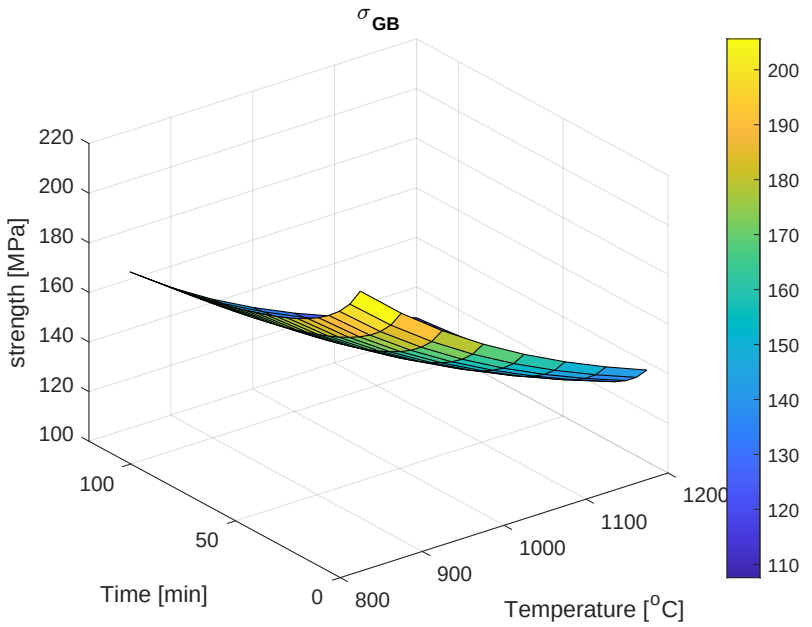

Figure 6.4: Influence of the homogenization heat treatment on the strength contributed by the grain boundaries in additively manufacture IN718

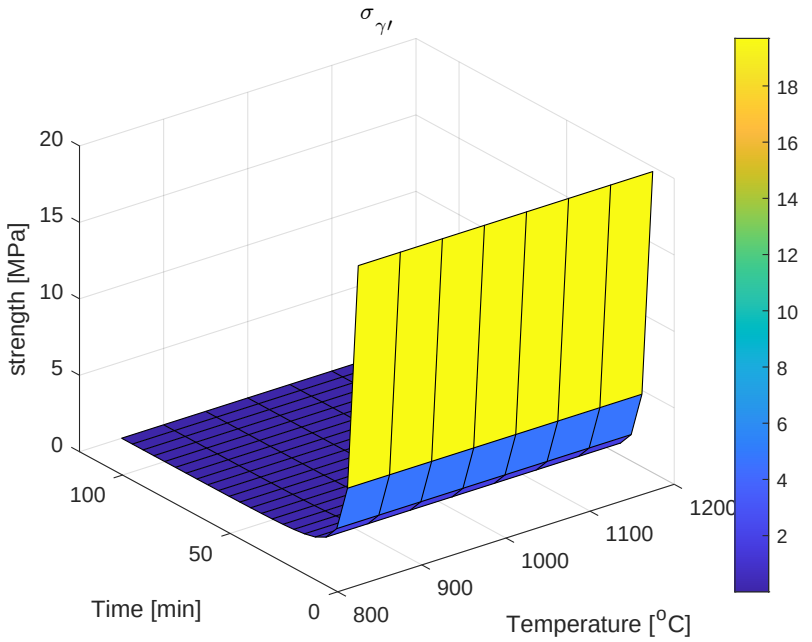

Figure 6.5: Influence of the homogenization heat treatment on the strength of γ' in additively manufacture IN718

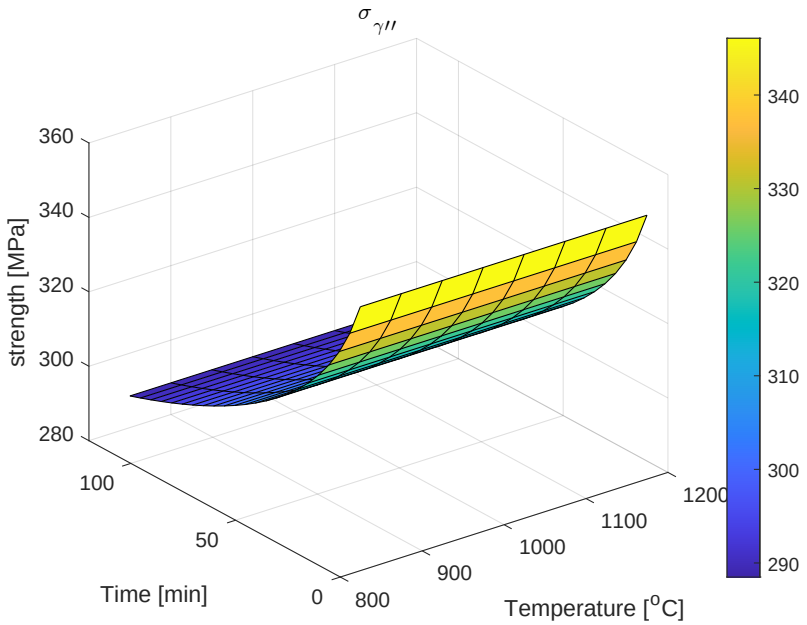

Figure 6.6: Influence of the homogenization heat treatment on the strength of γ" in additively manufacture IN718

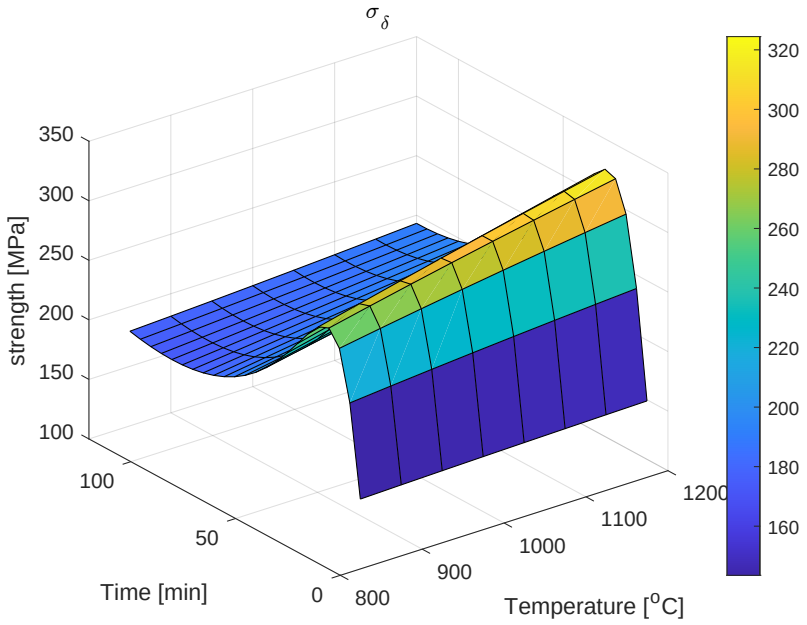

Figure 6.7: Influence of the homogenization heat treatment on the strength of δ in additively manufacture IN718

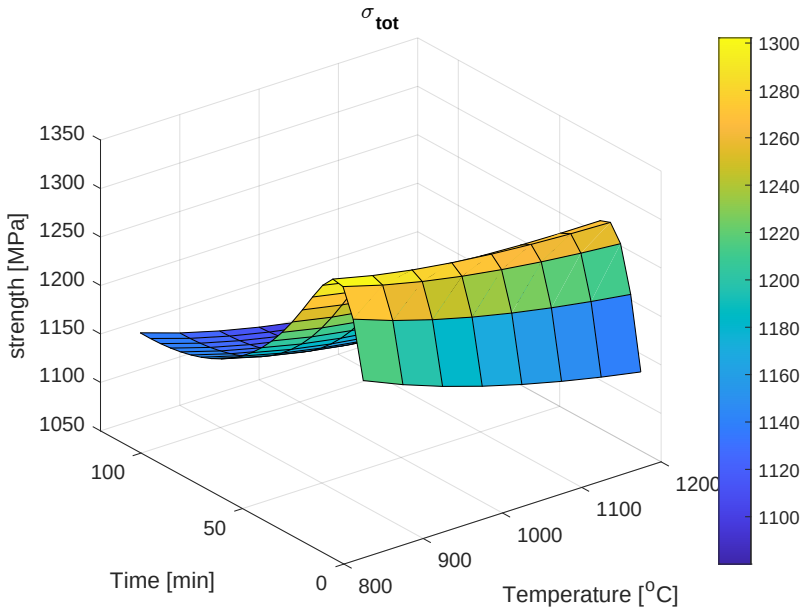

Figure 6.8: Influence of the homogenization heat treatment on the total strength of additively manufacture IN718

6.4.2 Effect of solution annealing

The solution annealing heat treatment has a similar impact on the grain boundary, γ', and δ phase strengths as can be seen in Figures 6.9-6.11. The grain boundary strength is reduced by further heat treating the alloy. The strength of γ' phase is independent of the solution annealing temperature and duration. The additional energy provided by the solution annealing increases the strength contribution of the δ phase even further with a similar pattern as observed in the homogenization heat treatment. The solution annealing heat treatment increases the γ" strength as the duration increases as can be seen in Figure 6.12. This could be a result of the improved diffusion causing the precipitates to grow further and increasing their shear strength, since by the time the solution annealing occurs most of the impact of the δ phase consuming the alloying material from the γ" already occurred during the homogenization heat treatment.

The combined impact on the total strength of solution annealed IN718 has a similar pattern as the homogenization heat treatment. However, the duration has less impact compared to the homogenization heat treatment. After reaching the maximum value approximately at 50 minutes the tensile strength decreases less compared to the homogenization heat treatment.

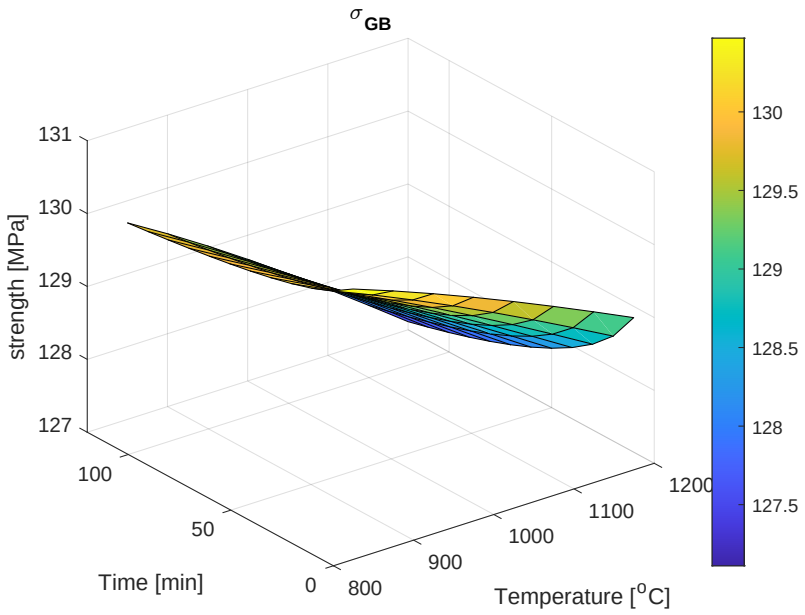

Figure 6.9: Influence of the solution annealing heat treatment on the strength contributed by the grain boundaries in additively manufacture IN718

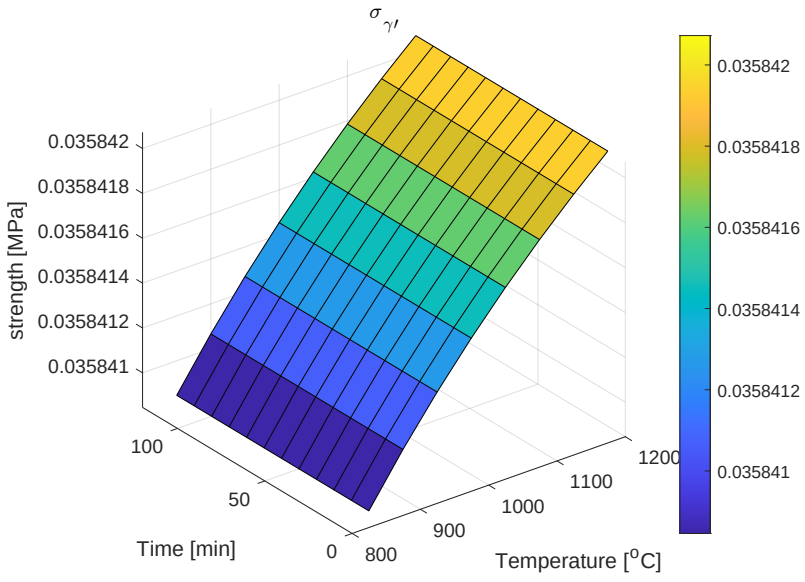

Figure 6.10: Influence of the solution annealing heat treatment on the strength of γ' in additively manufacture IN718

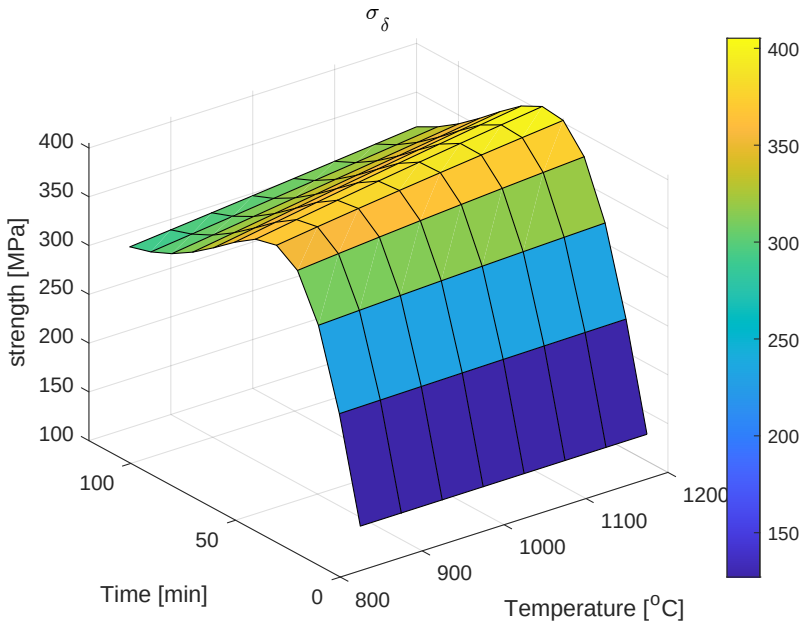

Figure 6.11: Influence of the solution annealing heat treatment on the strength of δ in additively manufacture IN718

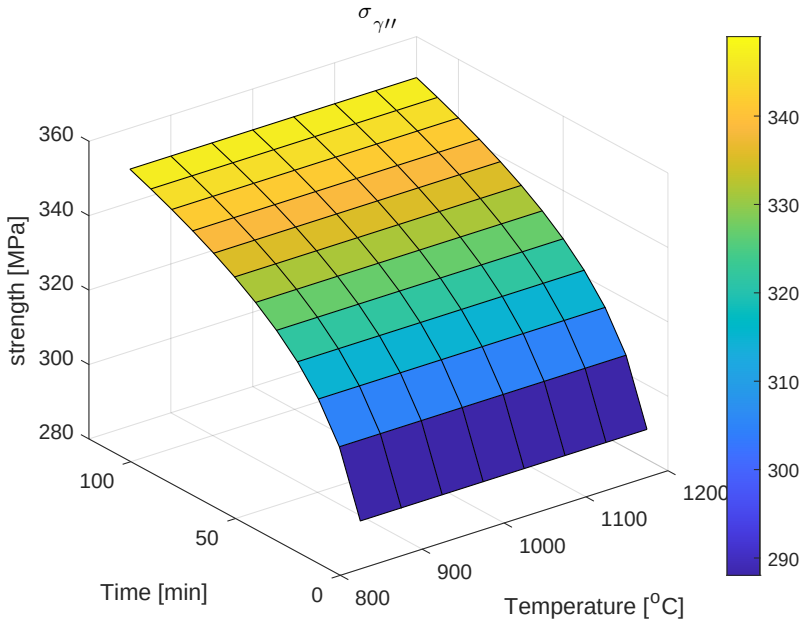

Figure 6.12: Influence of the solution annealing heat treatment on the strength of γ" in additively manufacture IN718

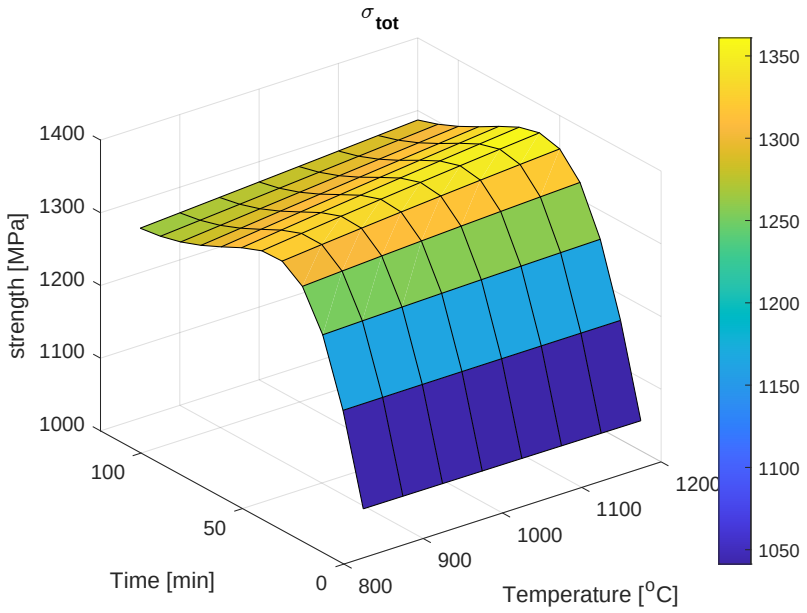

Figure 6.13: Influence of the solution annealing heat treatment on the total strength of additively manufacture IN718

6.4.3 Effect of part orientation

The effect of the part's orientation on the tensile strength of additively manufactured IN718 is illustrated in Figure 6.14. The effect of the angle between the length of the specimen and the build plate, ϕ, is more significant than the effect of the angle between the width of the specimen and the build plate, θ. It is clear that parts with a large ϕ, in a vertical orientation, have lower tensile strength. The maximum $\Delta\sigma$ due to orientation for a part after two steps of heat treatment is around 130 MPa, which is mostly due to ϕ. In comparison, the maximum variation due to θ is about 18 MPa.

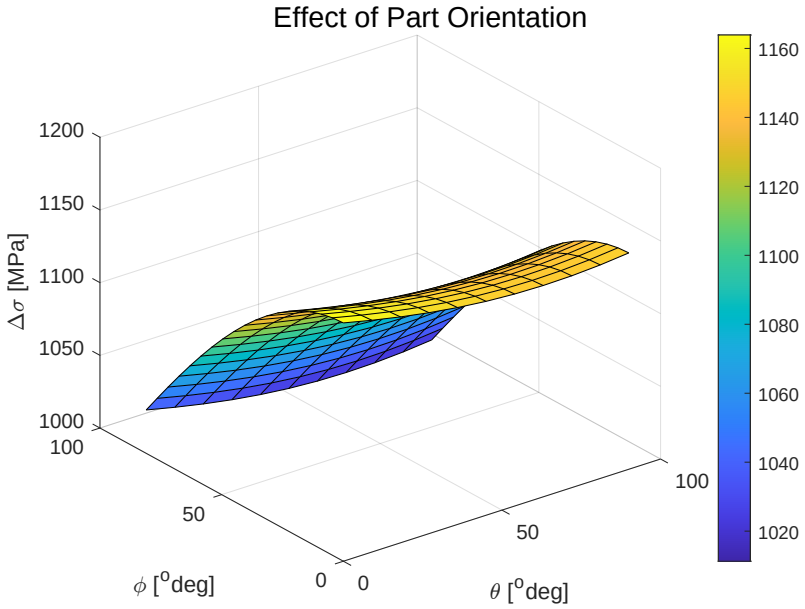

Figure 6.14: Influence of the part's orientation during PBF on the tensile strength

6.4.4 Effect of environmental temperature

The effect of the environmental temperature on the tensile strength of IN718 is presented in Figure 6.15. The curve representing the total tensile strength closely resembles that reported by SpecialMetals [186] and illustrated in Figure 6.16. The individual effect of the environmental temperature on the γ, γ', γ", and δ phases should not be interpreted directly as the degrees of freedom allowed for the effect environmental temperature on their strength might be confounded. However, it is clear that the tensile strength contributed by the δ phase decreases significantly as the temperature approaches its solvus temperature. The decrease in the γ phase before its melting temperature is explained by the increase in the grain size and reduction in the dislocation density.

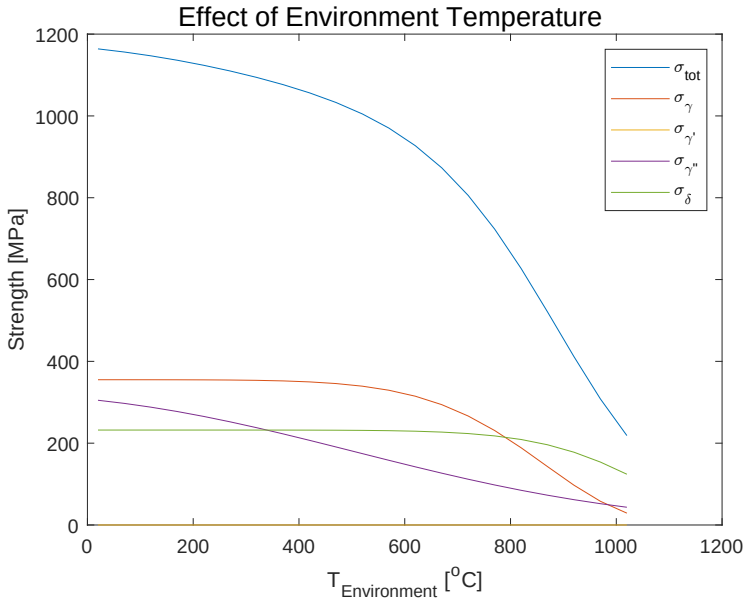

Figure 6.15: Effect of the environment temperature on the tensile strength of additively manufacture IN718

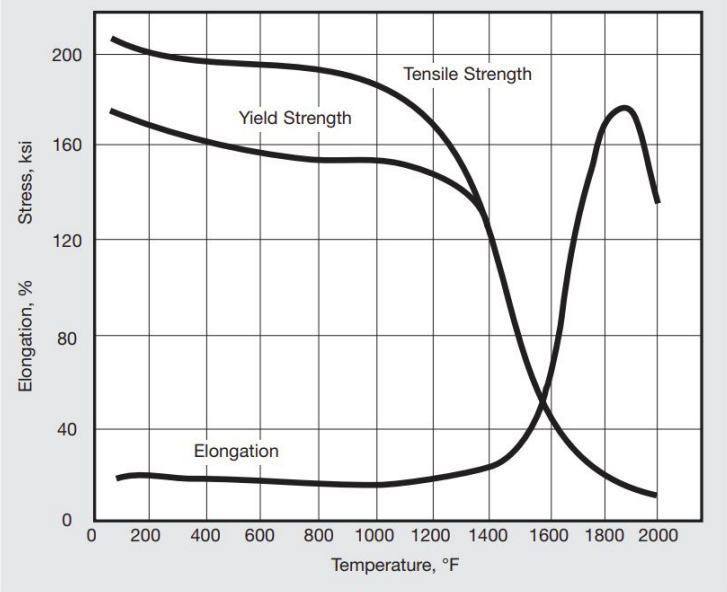

Figure 6.16: The tensile strength of IN718 at elevated temperatures reported by SpecialMetals for solution annealed and aged hot-rolled bars

6.5 Conclusions

In this study, the influence of the homogenization and solution annealing heat treatments on the tensile strength of additively manufactured IN718 parts is modeled using a hybrid machine learning approach. The influence of the part's orientation during the PBF process and environmental temperatures were considered in the model. The model uses physically derived information and enforces constraints on the model's constants so that the model report physically meaningful values.

- Hybrid modeling using physically derived equations and physically informed constraints can model the influence of heat treatments on the tensile strength of additively manufactured IN718. The results show great potential in using hybrid modeling to achieve accurate models with relatively small data. The model presented here achieved a fitness index of $R^2 = 0.88$. However, a totally unconstrained model achieved a fitness index of $R^2 = 0.90$. The higher index of fitness, however, is achieved at the cost of losing physical meaning to the different strengthening mechanisms in the IN718 alloy. The improvement in R^2, however, indicates room for improvement in the constrained model.

- The strength contribution from the grain boundary drops significantly after the homogenization heat treatment. The solution annealing heat treatment further reduces that contribution but to a significantly less degree. Also, the contribution of the grain boundary closely matches results from experimental work in literature.

- The strength of the γ' does not appear to be affected by the solution annealing and homogenization heat treatments. However, the effect on γ' might be confounded and hidden in the effects on the γ" or δ phases. Additional experimental work might be necessary to separate the effects on the different phases. The effect on the δ and γ" phases are more observable and their contribution significantly affects the total strength of IN718.

- The model simulating the influence of the orientation of the parts during powder bed fusion (DMLS/SLM) successfully demonstrates experimentally observed results. However, the impact of the homogenization and solution annealing heat treatments on the anisotropy was only modeled on the grain size and intrinsic strength of the matrix γ. The preferred orientation due to the thermal gradient may cause the precipitates to form in preferred orientations. A more complex model might be necessary to further improve the accuracy of the model.

- The environmental temperature influence on the total tensile strength of IN718 was closely modeled using the proposed model. The impact on the environmental temperature on the individual phases, while closely matching the

expected behavior near their respective solvus temperatures might be confounded and additional data might be necessary before they can be interpreted numerically.

Chapter 7

CONCLUSIONS

The research conducted in this dissertation investigated the microstructure and mechanical properties of additively manufactured 15-5PH and Inconel 718 in their as-built condition. Then proposed modified heat treatments that can improve the reliability of these parts in structure and load-bearing applications. Finally, a hybrid model was developed to understand the influence of solution annealing, homogenization heat treatment, and part orientation in the tensile strength of Inconel 718 at room and elevated temperatures. The following summarizes the most important conclusions of the work presented here:

- As-built additively manufactured 15-5PH and Inconel 718 can be used in applications with environmental temperatures up to 350°C without any permanent changes to the microstructure. However, reductions in the modulus of elasticity, strength, and ductility are observed at these temperatures.

- The difference in the microstructure patterns (texture) in parts fabricated in different orientations during the DMLS process is a major factor in the anisotropy in the modulus of elasticity, strength, and ductility.

- Solution annealing the DMLS 15-5PH parts before the precipitation hardening significantly improves the modulus of elasticity, yield strengths, and tensile strength. This improvement is achieved, however, at the cost of reducing the ductility.

- The standard solution annealing heat treatment of 15-5PH steel, usually called Condition A, is not sufficient to eliminate the anisotropy observed in the DMLS as-built condition. By extending the duration of this heat treatment from 1 hour to 3 hours a slight improvement in the tensile and yield strength is observed at the cost of further reduction in the ductility. However, this results in further reducing the anisotropy. This means DMLS parts can be manufactured in the most convenient orientation for fabrication and still obtain similar mechanical properties to parts fabricated in the optimum orientation for the mechanical properties.

- Heat treating 15-5PH specimens fabricated by DMLS at 1200°C and furnace cooling it before solution annealing has proved to be detrimental and caused the specimens to fail suddenly sometimes before yielding and at unpredictable locations.

- Using an extended solution annealing coupled with a different precipitation hardening heat treatment such as H1150 might improve the fatigue life of DMLS 15-5PH parts, which showed better performance over H900 with the standard solution annealing.

- The mechanical properties such as tensile strength, yield strength, and Young's modulus of as-built DMLS IN718 and standard heat treatment condition (as described by AMS 5662) depend on the orientation of the specimens, which demonstrates high anisotropy. The microstructure exposed on the surfaces normal to the tensile stress showed different patterns depending on the orientation of the specimen. The similarity in the microstructure in the as-built condition and the standard heat treatment demonstrates the failure of the standard heat treatment to homogenize the microstructure and reduce the anisotropy in the mechanical properties.

- The proposed modifications to the solution annealing heat treatments by including an initial step at 1200 or 1270°C for less than 20 minutes and shorting the duration of the 980°C step to 20-40 minutes instead of one hour resulted in homogenizing the microstructure and making it similar to heat-treated wrought or cast IN718. This reduced the anisotropy and improved the repeatability of the mechanical properties regardless of the specimen's orientation.

- The XRD analysis and Rietveld refinement have proved that changing the solution annealing heat treatment by including an additional step prior to the 980°C has a significant impact on the phases that can precipitate during aging. In the standard heat treatment, γ'' is usually 3-4 times the volume fraction of γ' but for additively manufactured IN718 the volume fraction of γ'' was larger than γ' by a factor of 2, in addition to 15% δ. By adding the 1200°C step the volume fraction γ' is four times the volume fraction of γ'' precipitates. This change in the volume fraction of the strengthening phases has shown a good combination of high strength and ductility in comparison to the standard heat treatment which has higher strength but lower ductility. This can be correlated to the volume fraction of the strengthening precipitates, in which γ'' provides superior strength in comparison to γ' but reduces the ductility. Replacing the 1200°C step with 1270°C resulted in a significant increase in the δ phase precipitates in the grain boundaries which resulted in reducing the ductility without significant improvement to the strength.

- This work demonstrates that adding prior heating steps at 1200°C or 1270°C and limiting the dwelling time to 5-20 minutes has proved effective in limiting the grain growth of the microstructure, while effectively homogenizing the microstructure. In comparison, work in the literature has shown significant grain growth when homogenization is done by increasing the dwelling time to 3 hours or by including a hot isostatic pressing treatment. Furthermore, reducing the duration of the initial step and the 980°C step to 20-40 minutes reduces the energy cost and the total post-processing time.

- Homogenizing the microstructure at 1200°C prior to solution annealing (HT2) is a suitable heat treatment program for parts in low-cycle fatigue application, which requires good ductility and HT2 provides a good combination of strength and ductility. HT1 provides the maximum tensile strength which makes it a suitable candidate for high-cycle fatigue applications.

Future work

This research can be extended in the following areas/direction.

- Utilize Electron Backscatter Diffraction (EBSD) to characterize the microstructure-grain size, preferred orientation, and precipitates volume fraction of additively manufactured Inconel 718 with different solution annealing heat treatments. This will lead to a better understanding of the mechanisms that control the volume fraction of the precipitates after the aging heat treatment.

- Investigate the influence of DMLS processing parameters and heat treatments on the tetragonality degree (c/a) of the Martensite in 15-5PH parts. Due to the low Carbon wt% in 15-5PH steel, Martensite is usually described with a body-centered cubic (BCC) structure instead of a body-centered tetragonal (BCT) structure. This knowledge will lead to a better understanding of the strengthening mechanisms in 15-5PH, which can lead to the development of application tailored heat treatments.

- Investigate the influence of homogenization and different solution annealing heat treatments on the fatigue strength and life of additively manufactured 15-5PH and Inconel 718 parts. DMLS 15-5PH and Inconel 718 in their as-built condition and respective standard heat treatment condition showed orders of magnitude inferior fatigue life compared to traditionally manufactured parts. The heat treatments proposed in this work show potential in improving the fatigue life and reliability of Inconel 718 and 15-5PH parts.

- Improve the accuracy of the hybrid model predicting the tensile strength of heat-treated Inconel 718 by implementing more complex models for evaluating

the strengthening effect of $\gamma\prime$ and $\gamma\prime\prime$ precipitates in additively manufactured Inconel 718. This will require additional experimental data to evaluate the additional constants needed in these models.

BIBLIOGRAPHY

[1] ASTM, F2921 - Standard Terminology for Additive Manufacturing — Coordinate Systems and Test, American Society for Testing and Materials i (2012) 12.
URL www.astm.org

[2] D. L. Naik, R. Kiran, On anisotropy, strain rate and size effects in vat photopolymerization based specimens, Additive Manufacturing 23 (2018) 181–196.
URL https://linkinghub.elsevier.com/retrieve/pii/S221486041730235X

[3] D. C. Aduba, E. D. Margaretta, A. E. Marnot, K. V. Heifferon, W. R. Surbey, N. A. Chartrain, A. R. Whittington, T. E. Long, C. B. Williams, Vat photopolymerization 3D printing of acid-cleavable PEG-methacrylate networks for biomaterial applications, Materials Today Communications 19 (2019) 204–211.
URL https://linkinghub.elsevier.com/retrieve/pii/S2352492818304069

[4] Y. L. Tee, P. Tran, M. Leary, P. Pille, M. Brandt, 3D Printing of polymer composites with material jetting: Mechanical and fractographic analysis, Additive Manufacturing 36 (2020) 101558.
URL https://linkinghub.elsevier.com/retrieve/pii/S2214860420309301

[5] A. Pugalendhi, R. Ranganathan, S. Ganesan, Impact of process parameters on mechanical behaviour in multi-material jetting, Materials Today: Proceedings.
URL https://linkinghub.elsevier.com/retrieve/pii/S2214785319341173

[6] T. Dahmen, N. Henriksen, K. Dahl, A. Lapina, D. Pedersen, J. Hattel, T. Christiansen, M. Somers, Densification, microstructure, and mechanical properties of heat-treated MAR-M247 fabricated by Binder Jetting, Additive Manufacturing 39 (2021) 101912.

URL https://linkinghub.elsevier.com/retrieve/pii/S2214860421000774

[7] J.-H. Ahn, J. Kim, G. Han, D. Kim, K.-H. Cheon, H. Lee, H.-E. Kim, Y.-J. Kim, T.-S. Jang, H.-D. Jung, 3D-printed biodegradable composite scaffolds with significantly enhanced mechanical properties via the combination of binder jetting and capillary rise infiltration process, Additive Manufacturing 41 (2021) 101988.
URL https://linkinghub.elsevier.com/retrieve/pii/S2214860421001536

[8] A. Alafaghani, A. Qattawi, J. Truong, M. S. Jaman, J.-Q. Sun, Optimizing Fused Deposition Modeling Processing Parameters Using Response Surface Method for Strong Parts, in: Volume 1: Additive Manufacturing; Advanced Materials Manufacturing; Biomanufacturing; Life Cycle Engineering; Manufacturing Equipment and Automation, American Society of Mechanical Engineers, Virtual, Online., 2020.
URL https://asmedigitalcollection.asme.org/MSEC/proceedings/MSEC2020/84256/Virtual,Online/1095631

[9] D. Rahmatabadi, M. Tayyebi, R. Hashemi, G. Faraji, Microstructure and mechanical properties of Al/Cu/Mg laminated composite sheets produced by the ARB proces, International Journal of Minerals, Metallurgy, and Materials 25 (5) (2018) 564–572.
URL http://link.springer.com/10.1007/s12613-018-1603-x

[10] X. Zhang, Y. Yu, B. Liu, J. Ren, Mechanical properties and tensile fracture mechanism investigation of Al/Cu/Ti/Cu/Al laminated composites fabricated by rolling, Journal of Alloys and Compounds 805 (2019) 338–345.
URL https://linkinghub.elsevier.com/retrieve/pii/S0925838819325617

[11] K. Aleksandr, S. Ferdinando, R. Joel, C. Joel, M. Jordan, J. Thomas, Effect of direct energy deposition parameters on morphology, residual stresses, density, and microstructure of 1.2709 maraging steel, The International Journal of Advanced Manufacturing Technology 117 (3-4) (2021) 1287–1301.
URL https://link.springer.com/10.1007/s00170-021-07635-w

[12] W. J. Oh, W. J. Lee, M. S. Kim, J. B. Jeon, D. S. Shim, Repairing additive-manufactured 316L stainless steel using direct energy deposition, Optics & Laser Technology 117 (2019) 6–17.
URL https://linkinghub.elsevier.com/retrieve/pii/S0030399218321960

[13] J. S. Panchagnula, S. Simhambhatla, Feature based Weld-Deposition for Additive Manufacturing of Complex Shapes, Journal of The Institution of Engineers (India): Series C 99 (3) (2018) 285–292.
URL https://link.springer.com/article/10.1007/s40032-016-0339-5

[14] T. F. Lam, Y. Xiong, A. G. Dharmawan, S. Foong, G. S. Soh, Adaptive process control implementation of wire arc additive manufacturing for thin-walled components with overhang features, The International Journal of Advanced Manufacturing Technology 108 (4) (2020) 1061–1071.
URL http://link.springer.com/10.1007/s00170-019-04737-4

[15] A. Alafaghani, A. Qattawi, M. S. Jaman, M. A. Ablat, Microstructure and mechanical properties of direct metal laser–sintered 15-5PH steel with different solution annealing heat treatments, The International Journal of Advanced Manufacturing Technology 105 (7-8) (2019) 3499–3520.
URL http://link.springer.com/10.1007/s00170-019-04404-8

[16] A. Alafaghani, A. Qattawi, M. A. G. Castañón, Effect of manufacturing parameters on the microstructure and mechanical properties of metal laser sintering parts of precipitate hardenable metals, The International Journal of Advanced Manufacturing Technology 99 (9-12) (2018) 2491–2507.
URL http://link.springer.com/10.1007/s00170-018-2586-5

[17] A. Qattawi, D. Ulutan, A. A. Alafaghani, Prediction of Mechanical Properties of Direct Metal Laser Sintered 15-5PH Steel Parts Using Bayesian Inference: A Preliminary Study, in: Volume 2: Processes; Materials, Vol. 2, American Society of Mechanical Engineers, 2019.
URL https://asmedigitalcollection.asme.org/MSEC/proceedings/MSEC2019/58752/Erie,Pennsylvania,USA/1070754

[18] S. Singh, S. Ramakrishna, R. Singh, Material issues in additive manufacturing: A review, Journal of Manufacturing Processes 25 (2017) 185–200.
URL http://dx.doi.org/10.1016/j.jmapro.2016.11.006

[19] D. Bourell, J. P. Kruth, M. Leu, G. Levy, D. Rosen, A. M. Beese, A. Clare, Materials for additive manufacturing, CIRP Annals - Manufacturing Technology 66 (2017) 659–681.
URL http://dx.doi.org/10.1016/j.cirp.2017.05.009

[20] A. Abad, M. Hahn, O. S. Es-Said, Corrosion of 15-5PH H1025 stainless steel due to environmental conditions, Engineering Failure Analysis 17 (1) (2010) 208–212.
URL http://dx.doi.org/10.1016/j.engfailanal.2009.06.004

[21] L. Couturier, F. De Geuser, M. Descoins, A. Deschamps, Evolution of the microstructure of a 15-5PH martensitic stainless steel during precipitation hardening heat treatment, Materials & Design 107 (2016) 416–425.
URL https://linkinghub.elsevier.com/retrieve/pii/S0264127516308206

[22] M. Abdelshehid, K. Mahmodieh, K. Mori, L. Chen, P. Stoyanov, D. Davlantes, J. Foyos, J. Ogren, R. Clark, O. S. Es-Said, On the correlation between fracture toughness and precipitation hardening heat treatments in 15-5PH Stainless Steel, Engineering Failure Analysis 14 (4) (2007) 626–631.

[23] X.-y. Peng, X.-l. Zhou, X.-z. Hua, Z.-w. Wei, H.-y. Liu, Effect of aging on hardening behavior of 15-5 PH stainless steel, Journal of Iron and Steel Research International 22 (7) (2015) 607–614.
URL http://linkinghub.elsevier.com/retrieve/pii/S1006706X15300479

[24] N. Fang, Q. Wu, A comparative study of the cutting forces in high speed machining of Ti-6Al-4V and Inconel 718 with a round cutting edge tool, Journal of Materials Processing Technology 209 (9) (2009) 4385–4389.

[25] R. S. Pawade, S. S. Joshi, P. K. Brahmankar, M. Rahman, An investigation of cutting forces and surface damage in high-speed turning of Inconel 718, Journal of Materials Processing Technology 192-193 (2007) 139–146.

[26] F. Ning, W. Cong, J. Qiu, J. Wei, S. Wang, Additive manufacturing of carbon fiber reinforced thermoplastic composites using fused deposition modeling, Composites Part B: Engineering.

[27] L. Chen, W. Zhu, Stochastic jump and bifurcation of Duffing oscillator with fractional derivative damping under combined harmonic and white noise excitations, International Journal of Non-Linear Mechanics 46 (10) (2011) 1324–1329.

[28] A. K. Parida, K. Maity, Comparison the machinability of Inconel 718, Inconel 625 and Monel 400 in hot turning operation, Engineering Science and Technology, an International Journal 21 (3) (2018) 364–370.

[29] M. A. Arie, A. H. Shooshtari, S. V. Dessiatoun, M. M. Ohadi, Performance characterization of an additively manufactured titanium (Ti64) heat exchanger for an air-water cooling application, in: ASME 2016 Heat Transfer Summer Conference, HT 2016, collocated with the ASME 2016 Fluids Engineering Division Summer Meeting and the ASME 2016 14th International Conference

on Nanochannels, Microchannels, and Minichannels, Vol. 2, American Society of Mechanical Engineers, 2016.

[30] C. Yan, L. Hao, A. Hussein, P. Young, D. Raymont, Advanced lightweight 316L stainless steel cellular lattice structures fabricated via selective laser melting, Materials and Design 55 (2014) 533–541.
URL http://dx.doi.org/10.1016/j.matdes.2013.10.027

[31] M. K. Thompson, G. Moroni, T. Vaneker, G. Fadel, R. I. Campbell, I. Gibson, A. Bernard, J. Schulz, P. Graf, B. Ahuja, F. Martina, Design for Additive Manufacturing: Trends, opportunities, considerations, and constraints, CIRP Annals 65 (2) (2016) 737–760.
URL https://linkinghub.elsevier.com/retrieve/pii/S0007850616301913

[32] N. Gardan, A. Schneider, Topological optimization of internal patterns and support in additive manufacturing, Journal of Manufacturing Systems 37 (2015) 417–425.

[33] J. Allen, An Investigation into the Comparative Costs of Additive Manufacture vs. Machine from Solid for Aero Engine Parts, Cost Effective Manufacture via Net-Shape Processing (2006) 17–1 – 17–10.
URL http://www.dtic.mil/docs/citations/ADA521730

[34] J. Parthasarathy, B. Starly, S. Raman, A design for the additive manufacture of functionally graded porous structures with tailored mechanical properties for biomedical applications (aug 2011).

[35] S. M. Thompson, L. Bian, N. Shamsaei, A. Yadollahi, An overview of Direct Laser Deposition for additive manufacturing; Part I: Transport phenomena, modeling and diagnostics, Additive Manufacturing 8 (2015) 36–62.
URL https://www.sciencedirect.com/science/article/pii/S2214860415000317

[36] N. Hopkinson, P. Dickens, Rapid prototyping for direct manufacture, Rapid Prototyping Journal 7 (4) (2001) 197–202.

[37] S. H. Khajavi, J. Partanen, J. Holmström, Additive manufacturing in the spare parts supply chain, Computers in Industry 65 (1) (2014) 50–63.

[38] M. Salmi, J. Tuomi, K. S. Paloheimo, R. Björkstrand, M. Paloheimo, J. Salo, R. Kontio, K. Mesimäki, A. A. Mäkitie, Patient-specific reconstruction with 3D modeling and DMLS additive manufacturing, Rapid Prototyping Journal 18 (3) (2012) 209–214.

[39] J. A. Slotwinski, E. J. Garboczi, P. E. Stutzman, C. F. Ferraris, S. S. Watson, M. A. Peltz, No Title, Journal of Research of the National Institute of Standards and Technology 119 (2014) 460–493.

[40] H. P. Tang, M. Qian, N. Liu, X. Z. Zhang, G. Y. Yang, J. Wang, Effect of Powder Reuse Times on Additive Manufacturing of Ti-6Al-4V by Selective Electron Beam Melting, Jom 67 (3) (2015) 555–563.
URL http://link.springer.com/10.1007/s11837-015-1300-4

[41] J. K. Watson, K. M. Taminger, A decision-support model for selecting additive manufacturing versus subtractive manufacturing based on energy consumption, Journal of Cleaner Production 176 (2018) 1316–1322.

[42] C. Klahn, B. Leutenecker, M. Meboldt, Design for additive manufacturing - Supporting the substitution of components in series products, Procedia CIRP 21 (2014) 138–143.
URL http://dx.doi.org/10.1016/j.procir.2014.03.145

[43] D. S. Thomas, S. W. Gilbert, Costs and Cost Effectiveness of Additive Manufacturing, Tech. rep., National Institute of Standards and Technology, Gaithersburg, MD (dec 2014).
URL http://dx.doi.org/10.6028/NIST.SP.1176https://nvlpubs.nist.gov/nistpubs/SpecialPublications/NIST.SP.1176.pdf

[44] G. N. Levy, R. Schindel, J. P. Kruth, Rapid manufacturing and rapid tooling with layer manufacturing (LM) technologies, state of the art and future perspectives, CIRP Annals - Manufacturing Technology 52 (2) (2003) 589–609.

[45] N. P. Karapatis, J. P. Van Griethuysen, R. Glardon, Direct rapid tooling: A review of current research, Rapid Prototyping Journal 4 (2) (1998) 77–89.

[46] K. Coffy, Microstructure and chemistry evaluation of direct metal laser sintered 15-5 PH stainless steel, Electronic Theses and Dissertations Paper 4756 (2014) 160.

[47] J. L. Dossett, H. E. Boyer, Practical Heat Treating, 2nd Edition, 2006.

[48] phase diagram iron carbon — Metallurgy for Dummies.
URL https://www.metallurgyfordummies.com/tag/iron-carbon-phase-diagram.html

[49] R. Smallman, A. Ngan, Physical Metallurgy and Advanced Materials Engineering, 2007.
URL http://www.sciencedirect.com/science/article/pii/B9780750669061500159

[50] K.-E. THELNING, Steel and its Heat Treatment, Elsevier, 1975.
URL https://linkinghub.elsevier.com/retrieve/pii/C20130042405

[51] S. Sakhawat, M. N. Baig, A. Falahati, H. P. Degischer, M. Dománková, A. Mahmood, Investigations of precipitation in two different types of precipitation hardening stainless steels, The Bulletin of the National R&D Institute for Welding and Material Testing (2015) 13–18.

[52] H. Habibi Bajguirani, The effect of ageing upon the microstructure and mechanical properties of type 15-5 PH stainless steel, Materials Science and Engineering: A 338 (1-2) (2002) 142–159.
URL http://www.sciencedirect.com/science/article/pii/S092150930200062X

[53] Special Metals Corporation, Inconel Alloy 718 (2020).
URL https://www.specialmetals.com/assets/smc/documents/inconel{_}alloy{_}718.pdf

[54] M. J. Donachie, Superalloys: A Technical Guide, 2nd Edition, America (2002) 1–409.
URL www.asminternational.org

[55] H. Wang, K. Ikeuchi, M. Takahashi, A. Ikeda, Microstructures of Inconel 718 alloy subjected to rapid thermal and stress cycle – joint performance and its controlling factors in friction welding of Inconel 718 alloy, Welding International 23 (9) (2009) 662–669.
URL https://www.tandfonline.com/doi/abs/10.1080/09507110902842851

[56] L. E. Murr, E. Martinez, S. M. Gaytan, D. A. Ramirez, B. I. MacHado, P. W. Shindo, J. L. Martinez, F. Medina, J. Wooten, D. Ciscel, U. Ackelid, R. B. Wicker, Microstructural architecture, microstructures, and mechanical properties for a nickel-base superalloy fabricated by electron beam melting, in: Metallurgical and Materials Transactions A: Physical Metallurgy and Materials Science, Vol. 42, 2011, pp. 3491–3508.

[57] G. F. V. Voort, G. M. Lucas, E. P. Manilova, Metallography and Microstructures of Heat-Resistant Alloys, ASM Handbook : Metallography and Microstructures 9 (2004) 820–859.
URL http://www.google.fr/url?sa=t{&}rct=j{&}q={&}esrc=s{&}source=web{&}cd=1{&}ved=0CDQQFjAA{&}url=http://www.georgevandervoort.com/mic{_}met{_}pdf/HeatResistingAlloys{_}Vol{_}9{_}MetalsHandbook.pdf{&}ei=7qzDULveJdCZ0QWdh4CIAg{&}usg=AFQjCNEd1{_}EKdyYVbivkA2mHoQk8nmSQeA

[58] T. M. Pollock, S. Tin, Nickel-Based Superalloys for Advanced Turbine Engines: Chemistry, Microstructure and Properties, Journal of Propulsion and Power 22 (2) (2006) 361–374.
URL http://arc.aiaa.org/doi/10.2514/1.18239

[59] J. Radavich, The Physical Metallurgy of Cast and Wrought Alloy 718, Superalloys 718 Metallurgy and Applications (1989) (2004) 229–240.
URL http://www.tms.org/Superalloys/10.7449/1989/Superalloys{_}1989{_}229{_}240.pdf

[60] A. Mostafa, I. Picazo Rubio, V. Brailovski, M. Jahazi, M. Medraj, Structure, Texture and Phases in 3D Printed IN718 Alloy Subjected to Homogenization and HIP Treatments, Metals 7 (6) (2017) 196.
URL http://www.mdpi.com/2075-4701/7/6/196https://www.mdpi.com/2075-4701/7/6/196/htmhttps://www.mdpi.com/2075-4701/7/6/196

[61] S. Azadian, L.-Y. Y. Wei, R. Warren, Delta phase precipitation in inconel 718, Materials Characterization 53 (1) (2004) 7–16.
URL https://www.sciencedirect.com/science/article/pii/S1044580304001603

[62] R. C. Reed, The Superalloys fundamentals and applications, Vol. 9780521859, 2006.

[63] A. Devaux, L. Nazé, R. Molins, A. Pineau, A. Organista, J. Y. Guédou, J. F. Uginet, P. Héritier, Gamma double prime precipitation kinetic in Alloy 718, Materials Science and Engineering A 486 (1-2) (2008) 117–122.

[64] B. Geddes, H. Leon, X. Huang, Superalloys: Alloying and Performance, 2010.
URL http://books.google.ca/books/about/Superalloys.html?id=UCiHLGu4uGUC{&}pgis=1

[65] K. Kulawik, P. A. Buffat, A. Kruk, A. M. Wusatowska-Sarnek, A. Czyrska-Filemonowicz, Imaging and characterization of Y' and Y" nanoparticles in Inconel 718 by EDX elemental mapping and FIB-SEM tomography, Materials Characterization 100 (2015) 74–80.

[66] Z. Hu, H. Zhu, H. Zhang, X. Zeng, Experimental investigation on selective laser melting of 17-4PH stainless steel, Optics & Laser Technology 87 (2017) 17–25.
URL https://linkinghub.elsevier.com/retrieve/pii/S0030399216302833

[67] K. Subramanian, N. Vail, J. Barlow, H. Marcus, Selective laser sintering of alumina with polymer binders, Rapid Prototyping Journal 1 (2) (1995) 24–35.

[68] J. P. Kruth, X. Wang, T. Laoui, L. Froyen, Lasers and materials in selective laser sintering, Assembly Automation 23 (4) (2003) 357–371.

[69] H. H. Zhu, L. Lu, J. Y. H. Fuh, Development and characterisation of direct laser sintering Cu-based metal powder, in: Journal of Materials Processing Technology, Vol. 140, 2003, pp. 314–317.

[70] Y. P. Kathuria, Microstructuring by selective laser sintering of metallic powder, Surface and Coatings Technology 116-119 (1999) 643–647.

[71] M. Islam, T. Purtonen, H. Piili, A. Salminen, O. Nyrhilä, Temperature Profile and Imaging Analysis of Laser Additive Manufacturing of Stainless Steel, Physics Procedia 41 (2013) 835–842.
URL http://www.sciencedirect.com/science/article/pii/S1875389213001703

[72] T. M. Mower, M. J. Long, Mechanical behavior of additive manufactured , powder-bed laser-fused materials, Materials Science & Engineering A 651 (2016) 198–213.
URL https://www.sciencedirect.com/science/article/pii/S092150931530530X

[73] W. J. Sames, F. A. List, S. Pannala, R. R. Dehoff, S. S. Babu, The metallurgy and processing science of metal additive manufacturing, International Materials Reviews 6608 (March) (2016) 1–46.
URL http://www.tandfonline.com/doi/full/10.1080/09506608.2015.1116649

[74] Q. Jia, D. Gu, Selective laser melting additive manufacturing of Inconel 718 superalloy parts: Densification, microstructure and properties, Journal of Alloys and Compounds 585 (2014) 713–721.
URL http://www.sciencedirect.com/science/article/pii/S0925838813023451

[75] H. Gong, K. Rafi, H. Gu, T. Starr, B. Stucker, Analysis of defect generation in Ti-6Al-4V parts made using powder bed fusion additive manufacturing processes, Additive Manufacturing 1 (2014) 87–98.
URL http://dx.doi.org/10.1016/j.addma.2014.08.002

[76] S. Pal, H. Reddy, I. Drstvenšek, C. Siva, H. R. Tiyyagura, I. Drstvenšek, C. S. Kumar, The effect of post-processing and machining process parameters

on properties of Stainless Steel PH1 product produced by Direct Metal Laser, Procedia Engineering 149 (June) (2016) 359–365.
URL https://www.sciencedirect.com/science/article/pii/S1877705816311894

[77] E. Lum, A. N. Palazotto, A. Dempsey, Analysis of the Effects of Additive Manufacturing on the Material Properties of 15-5PH Stainless Steel, in: 58th AIAA/ASCE/AHS/ASC Structures, Structural Dynamics, and Materials Conference, no. January, American Institute of Aeronautics and Astronautics, Reston, Virginia, 2017.
URL http://arc.aiaa.org/doi/10.2514/6.2017-1142

[78] T. Vilaro, C. Colin, J. Bartout, L. Nazé, M. Sennour, Microstructural and mechanical approaches of the selective laser melting process applied to a nickel-base superalloy, Materials Science and Engineering: A 534 (2012) 446–451.
URL https://linkinghub.elsevier.com/retrieve/pii/S0921509311013311

[79] K. Amato, S. Gaytan, L. Murr, E. Martinez, P. Shindo, J. Hernandez, S. Collins, F. Medina, Microstructures and mechanical behavior of Inconel 718 fabricated by selective laser melting, Acta Materialia 60 (5) (2012) 2229–2239.
URL http://www.sciencedirect.com/science/article/pii/S1359645411008949

[80] D. H. Smith, J. Bicknell, L. Jorgensen, B. M. Patterson, N. L. Cordes, I. Tsukrov, M. Knezevic, Microstructure and mechanical behavior of direct metal laser sintered Inconel alloy 718, Materials Characterization 113 (2016) 1–9.
URL http://dx.doi.org/10.1016/j.matchar.2016.01.003

[81] X. Wang, T. Keya, K. Chou, Build Height Effect on the Inconel 718 Parts Fabricated by Selective Laser Melting, Procedia Manufacturing 5 (2016) 1006–1017.
URL https://www.sciencedirect.com/science/article/pii/S2351978916301019?dgcid=raven{_}sd{_}recommender{_}email

[82] Z. Wang, K. Guan, M. Gao, X. Li, X. Chen, X. Zeng, The microstructure and mechanical properties of deposited-IN718 by selective laser melting, Journal of Alloys and Compounds 513 (2012) 518–523.
URL http://dx.doi.org/10.1016/j.jallcom.2011.10.107https://linkinghub.elsevier.com/retrieve/pii/S0925838811020767

[83] T. Trosch, J. Strößner, R. Völkl, U. Glatzel, Microstructure and mechanical properties of selective laser melted Inconel 718 compared to forging and casting, Materials Letters 164 (2016) 428–431.
URL https://www.sciencedirect.com/science/article/pii/S0167577X15307850

[84] C. Koch, L. Van Hulle, N. Rudolph, Investigation of mechanical anisotropy of the fused filament fabrication process via customized tool path generation, Additive Manufacturing 16 (2017) 138–145.
URL https://linkinghub.elsevier.com/retrieve/pii/S2214860417300465

[85] A. Alafaghani, A. Qattawi, B. Alrawi, A. Guzman, Experimental Optimization of Fused Deposition Modelling Processing Parameters: A Design-for-Manufacturing Approach, Procedia Manufacturing 10 (2351-9789) (2017) 791–803.
URL https://linkinghub.elsevier.com/retrieve/pii/S2351978917302615

[86] A. Boschetto, V. Giordano, F. Veniali, Modelling micro geometrical profiles in fused deposition process, The International Journal of Advanced Manufacturing Technology 61 (9-12) (2012) 945–956.
URL http://link.springer.com/10.1007/s00170-011-3744-1

[87] A. Alafaghani, A. Qattawi, M. A. Ablat, Design Consideration for Additive Manufacturing: Fused Deposition Modelling, Open Journal of Applied Sciences 07 (06) (2017) 291–318.
URL http://www.scirp.org/journal/doi.aspx?DOI=10.4236/ojapps.2017.76024

[88] F. Rayegani, G. C. Onwubolu, Fused deposition modelling (fdm) process parameter prediction and optimization using group method for data handling (gmdh) and differential evolution (de), International Journal of Advanced Manufacturing Technology 73 (1-4) (2014) 509–519.
URL http://dx.doi.org/10.1007/s00170-014-5835-2

[89] P. T. Lan, S. Y. Chou, L. L. Chen, D. Gemmill, Determining fabrication orientations for rapid prototyping with stereolithography apparatus, CAD Computer Aided Design 29 (1) (1997) 53–62.

[90] M. Masoomi, N. Shamsaei, R. A. Winholtz, J. L. Milner, T. Gnäupel-Herold, A. Elwany, M. Mahmoudi, S. M. Thompson, Residual stress measurements via neutron diffraction of additive manufactured stainless steel 17-4 PH, Data

in Brief 13 (2017) 408–414.
URL https://linkinghub.elsevier.com/retrieve/pii/S2352340917302718

[91] A. S. Johnson, S. Shao, N. Shamsaei, S. M. Thompson, L. Bian, Microstructure, Fatigue Behavior, and Failure Mechanisms of Direct Laser-Deposited Inconel 718, JOM 69 (3) (2017) 597–603.
URL http://link.springer.com/10.1007/s11837-016-2225-2

[92] R. Konečná, G. Nicoletto, L. Kunz, A. Bača, Microstructure and directional fatigue behavior of Inconel 718 produced by selective laser melting, Procedia Structural Integrity 2 (2016) 2381–2388.
URL https://linkinghub.elsevier.com/retrieve/pii/S2452321616303092

[93] S. Gribbin, J. Bicknell, L. Jorgensen, I. Tsukrov, M. Knezevic, Low cycle fatigue behavior of direct metal laser sintered Inconel alloy 718, International Journal of Fatigue 93 (2016) 156–167.
URL https://linkinghub.elsevier.com/retrieve/pii/S0142112316302614

[94] R. Konečná, L. Kunz, G. Nicoletto, A. Bača, Long fatigue crack growth in Inconel 718 produced by selective laser melting, International Journal of Fatigue 92 (2016) 499–506.
URL https://linkinghub.elsevier.com/retrieve/pii/S0142112316300172

[95] H. Masuo, Y. Tanaka, S. Morokoshi, H. Yagura, T. Uchida, Y. Yamamoto, Y. Murakami, Influence of defects, surface roughness and HIP on the fatigue strength of Ti-6Al-4V manufactured by additive manufacturing, International Journal of Fatigue 117 (2018) 163–179.
URL https://linkinghub.elsevier.com/retrieve/pii/S0142112318303050

[96] H. K. Rafi, T. L. Starr, B. E. Stucker, A comparison of the tensile, fatigue, and fracture behavior of Ti–6Al–4V and 15-5 PH stainless steel parts made by selective laser melting, The International Journal of Advanced Manufacturing Technology 69 (5-8) (2013) 1299–1309.
URL http://link.springer.com/10.1007/s00170-013-5106-7

[97] A. Spierings, T. Starr, K. Wegener, Fatigue performance of additive manufactured metallic parts, Rapid Prototyping Journal 19 (2) (2013) 88–94.
URL https://www.emerald.com/insight/content/doi/10.1108/13552541311302932/full/html

[98] A. Yadollahi, J. Simsiriwong, S. M. Thompson, N. Shamsaei, Data demonstrating the effects of build orientation and heat treatment on fatigue behavior of selective laser melted 17–4 PH stainless steel, Data in Brief 7 (2016) 89–92.
URL https://linkinghub.elsevier.com/retrieve/pii/S235234091630035X

[99] S. Sarkar, C. S. Kumar, A. K. Nath, Effects of different surface modifications on the fatigue life of selective laser melted 15–5 PH stainless steel, Materials Science and Engineering: A 762 (2019) 138109.
URL https://linkinghub.elsevier.com/retrieve/pii/S0921509319308950

[100] A. Yadollahi, S. M. Thompson, A. Elwany, L. Bian, N. Shamsaei, S. M. Thompson, A. Elwany, L. Bian, N. Shamsaei, S. M. Thompson, A. Elwany, L. Bian, Effects of building orientation and heat treatment on fatigue behavior of selective laser melted 17-4 PH stainless steel, International Journal of Fatigue 94 (2017) 218–235.
URL http://www.sciencedirect.com/science/article/pii/S0142112316300202

[101] S. Sarkar, C. S. Kumar, A. K. Nath, Effects of heat treatment and build orientations on the fatigue life of selective laser melted 15-5 PH stainless steel, Materials Science and Engineering: A 755 (2019) 235–245.
URL https://www.sciencedirect.com/science/article/abs/pii/S0921509319304496

[102] S. Sarkar, C. S. Kumar, A. K. Nath, Investigation on the mode of failures and fatigue life of laser-based powder bed fusion produced stainless steel parts under variable amplitude loading conditions, Additive Manufacturing 25 (2019) 71–83.
URL https://linkinghub.elsevier.com/retrieve/pii/S2214860417303172

[103] I. Choudhury, M. El-Baradie, Machinability of nickel-base super alloys: a general review, Journal of Materials Processing Technology 77 (1-3) (1998) 278–284.
URL https://linkinghub.elsevier.com/retrieve/pii/S0924013697004299

[104] B. Clausen, D. Brown, J. Carpenter, K. Clarke, A. Clarke, S. Vogel, J. Bernardin, D. Spernjak, J. Thompson, Deformation behavior of additively manufactured GP1 stainless steel, Materials Science and Engineering: A 696 (February) (2017) 331–340.

URL https://linkinghub.elsevier.com/retrieve/pii/S092150931730549X

[105] H. D. Carlton, A. Haboub, G. F. Gallegos, D. Y. Parkinson, A. A. MacDowell, Damage evolution and failure mechanisms in additively manufactured stainless steel, Materials Science and Engineering: A 651 (2016) 406–414.
URL https://linkinghub.elsevier.com/retrieve/pii/S0921509315305347

[106] L. Facchini, N. Vicente, I. Lonardelli, E. Magalini, P. Robotti, A. Molinari, Metastable Austenite in 17-4 Precipitation-Hardening Stainless Steel Produced by Selective Laser Melting, Advanced Engineering Materials 12 (3) (2010) 184–188.
URL https://onlinelibrary.wiley.com/doi/10.1002/adem.200900259

[107] S. Cheruvathur, E. A. Lass, C. E. Campbell, Additive Manufacturing of 17-4 PH Stainless Steel: Post-processing Heat Treatment to Achieve Uniform Reproducible Microstructure, JOM 68 (3) (2016) 930–942.
URL http://link.springer.com/10.1007/s11837-015-1754-4

[108] D. Croccolo, M. De Agostinis, S. Fini, G. Olmi, N. Bogojevic, S. Ciric-Kostic, Effects of build orientation and thickness of allowance on the fatigue behaviour of 15-5 PH stainless steel manufactured by DMLS, Fatigue & Fracture of Engineering Materials & Structures 41 (4) (2018) 900–916.
URL https://onlinelibrary.wiley.com/doi/10.1111/ffe.12737

[109] H. K. Rafi, D. Pal, N. Patil, T. L. Starr, B. E. Stucker, Microstructure and Mechanical Behavior of 17-4 Precipitation Hardenable Steel Processed by Selective Laser Melting, Journal of Materials Engineering and Performance 23 (12) (2014) 4421–4428.

[110] S. Sarkar, C. S. Kumar, A. K. Nath, Effect of Different Heat Treatments on Mechanical Properties of Laser Sintered Additive Manufactured Parts, Journal of Manufacturing Science and Engineering 139 (11) (2017) 111010.
URL http://manufacturingscience.asmedigitalcollection.asme.org/article.aspx?doi=10.1115/1.4037437

[111] M. Kamal, G. Rizza, Design for metal additive manufacturing for aerospace applications, in: Additive Manufacturing for the Aerospace Industry, Elsevier, 2019, pp. 67–86.
URL https://www.sciencedirect.com/science/article/pii/B9780128140628000054

[112] S. Raghavan, B. Zhang, P. Wang, C.-N. Sun, M. L. S. Nai, T. Li, J. Wei, Effect of different heat treatments on the microstructure and mechanical properties in selective laser melted INCONEL 718 alloy, Materials and Manufacturing Processes 32 (14) (2017) 1588–1595.
URL https://www.tandfonline.com/doi/full/10.1080/10426914.2016.1257805

[113] W. M. Tucho, P. Cuvillier, A. Sjolyst-Kverneland, V. Hansen, Microstructure and hardness studies of Inconel 718 manufactured by selective laser melting before and after solution heat treatment, Materials Science and Engineering: A 689 (February) (2017) 220–232.
URL https://linkinghub.elsevier.com/retrieve/pii/S092150931730223X

[114] Y. Zhang, L. Yang, T. Chen, W. Zhang, X. Huang, J. Dai, Investigation on the optimized heat treatment procedure for laser fabricated IN718 alloy, Optics & Laser Technology 97 (2017) 172–179.
URL https://linkinghub.elsevier.com/retrieve/pii/S0030399216314566

[115] W. Tillmann, C. Schaak, J. Nellesen, M. Schaper, M. Aydinöz, K.-P. Hoyer, Hot isostatic pressing of IN718 components manufactured by selective laser melting, Additive Manufacturing 13 (2017) 93–102.
URL https://linkinghub.elsevier.com/retrieve/pii/S2214860416300495

[116] R. Seede, A. Mostafa, V. Brailovski, M. Jahazi, M. Medraj, Microstructural and Microhardness Evolution from Homogenization and Hot Isostatic Pressing on Selective Laser Melted Inconel 718: Structure, Texture, and Phases, Journal of Manufacturing and Materials Processing 2 (2) (2018) 30.
URL http://www.mdpi.com/2504-4494/2/2/30

[117] X. Yao, S. K. Moon, G. Bi, A hybrid machine learning approach for additive manufacturing design feature recommendation, Rapid Prototyping Journal 23 (6) (2017) 983–997.
URL https://www.emerald.com/insight/content/doi/10.1108/RPJ-03-2016-0041/full/html

[118] S. L. Chan, Y. Lu, Y. Wang, Data-driven cost estimation for additive manufacturing in cybermanufacturing, Journal of Manufacturing Systems 46 (2018) 115–126.
URL https://linkinghub.elsevier.com/retrieve/pii/S0278612517301577

[119] A. T. Gaynor, Topology Optimization Algorithms for Additive Manufacturing, Ph.D. thesis (feb 2015).

[120] Z. Zhu, N. Anwer, Q. Huang, L. Mathieu, Machine learning in tolerancing for additive manufacturing, CIRP Annals 67 (1) (2018) 157–160.
URL https://linkinghub.elsevier.com/retrieve/pii/S0007850618301434

[121] S. Chowdhury, K. Mhapsekar, S. Anand, Part Build Orientation Optimization and Neural Network-Based Geometry Compensation for Additive Manufacturing Process, Journal of Manufacturing Science and Engineering 140 (3).
URL https://asmedigitalcollection.asme.org/manufacturingscience/article/doi/10.1115/1.4038293/366667/Part-Build-Orientation-Optimization-and-Neural

[122] H. P. Nagarajan, H. Mokhtarian, H. Jafarian, S. Dimassi, S. Bakrani-Balani, A. Hamedi, E. Coatanéa, G. Gary Wang, K. R. Haapala, Knowledge-based design of artificial neural network topology for additive manufacturing process modeling: A new approach and case study for fused deposition modeling, Journal of Mechanical Design, Transactions of the ASME 141 (2).
URL https://asmedigitalcollection.asme.org/mechanicaldesign/article/doi/10.1115/1.4042084/368156/KnowledgeBased-Design-of-Artificial-Neural-Network

[123] Z. Jin, Z. Zhang, G. X. Gu, Autonomous in-situ correction of fused deposition modeling printers using computer vision and deep learning, Manufacturing Letters 22 (2019) 11–15.
URL https://linkinghub.elsevier.com/retrieve/pii/S2213846319300847

[124] Y. Wang, J. Huang, Y. Wang, S. Feng, T. Peng, H. Yang, J. Zou, A CNN-Based Adaptive Surface Monitoring System for Fused Deposition Modeling, IEEE/ASME Transactions on Mechatronics 25 (5) (2020) 2287–2296.
URL https://ieeexplore.ieee.org/document/9097947/

[125] A. Alafaghani, M. A. Ablat, H. Abedi, A. Qattawi, Modeling the influence of fused filament fabrication processing parameters on the mechanical properties of ABS parts, Journal of Manufacturing Processes 71 (2021) 711–723.
URL https://linkinghub.elsevier.com/retrieve/pii/S1526612521007180

[126] J. Lyu, S. Manoochehri, Dimensional prediction for FDM machines using artificial neural network and support vector regression, in: Proceedings of the

ASME Design Engineering Technical Conference, Vol. 1, American Society of Mechanical Engineers, 2019.
URL https://asmedigitalcollection.asme.org/IDETC-CIE/proceedings/IDETC-CIE2019/59179/Anaheim,California,USA/1069651

[127] S. Deswal, R. Narang, D. Chhabra, Modeling and parametric optimization of FDM 3D printing process using hybrid techniques for enhancing dimensional preciseness, International Journal on Interactive Design and Manufacturing (IJIDeM) 13 (3) (2019) 1197–1214.
URL https://link.springer.com/article/10.1007/s12008-019-00536-z

[128] B. C. Csaji, Approximation with Artificial Neural Networks, Ph.D. thesis, Eindhoven University of Technology (2001).
URL http://citeseerx.ist.psu.edu/viewdoc/download?doi=10.1.1.101.2647{&}rep=rep1{&}type=pdf

[129] V. Kůrková, Kolmogorov's theorem and multilayer neural networks, Neural Networks 5 (3) (1992) 501–506.
URL https://linkinghub.elsevier.com/retrieve/pii/0893608092900128

[130] P. Agrawal, R. Girshick, J. Malik, Analyzing the Performance of Multilayer Neural Networks for Object Recognition, in: Lecture Notes in Computer Science (including subseries Lecture Notes in Artificial Intelligence and Lecture Notes in Bioinformatics), Vol. 8695 LNCS, Springer Verlag, 2014, pp. 329–344.
URL http://link.springer.com/10.1007/978-3-319-10584-0{_}22

[131] G. Arulampalam, A. Bouzerdoum, A generalized feedforward neural network architecture for classification and regression, Neural Networks 16 (5-6) (2003) 561–568.
URL https://linkinghub.elsevier.com/retrieve/pii/S0893608003001163

[132] F. Murtagh, Multilayer perceptrons for classification and regression, Neurocomputing 2 (5-6) (1991) 183–197.
URL https://linkinghub.elsevier.com/retrieve/pii/0925231291900235

[133] M. Paliwal, U. A. Kumar, Neural networks and statistical techniques: A review of applications, Expert Systems with Applications 36 (1) (2009) 2–17.
URL https://linkinghub.elsevier.com/retrieve/pii/S0957417407004952

[134] M. Jamli, N. Farid, The sustainability of neural network applications within finite element analysis in sheet metal forming: A review, Measurement 138 (2019) 446–460.
URL https://linkinghub.elsevier.com/retrieve/pii/S0263224119301526

[135] J. Zhou, J. Ren, C. Yao, Multi-objective optimization of multi-axis ball-end milling Inconel 718 via grey relational analysis coupled with RBF neural network and PSO algorithm, Measurement 102 (2017) 271–285.
URL https://linkinghub.elsevier.com/retrieve/pii/S0263224117300799

[136] N. H. Alharthi, S. Bingol, A. T. Abbas, A. E. Ragab, E. A. El-Danaf, H. F. Alharbi, Optimizing Cutting Conditions and Prediction of Surface Roughness in Face Milling of AZ61 Using Regression Analysis and Artificial Neural Network, Advances in Materials Science and Engineering 2017 (2017) 1–8.
URL https://www.hindawi.com/journals/amse/2017/7560468/

[137] E. Ezugwu, D. Fadare, J. Bonney, R. Da Silva, W. Sales, Modelling the correlation between cutting and process parameters in high-speed machining of Inconel 718 alloy using an artificial neural network, International Journal of Machine Tools and Manufacture 45 (12-13) (2005) 1375–1385.
URL https://linkinghub.elsevier.com/retrieve/pii/S0890695505000556

[138] T. Sathish, Prediction of springback effect by the hybridisation of ANN with PSO in wipe bending process of sheet metal, Progress in Industrial Ecology, An International Journal 12 (1/2) (2018) 112.
URL http://www.inderscience.com/link.php?id=95881

[139] C. Herriott, A. D. Spear, Predicting microstructure-dependent mechanical properties in additively manufactured metals with machine- and deep-learning methods, Computational Materials Science 175 (2020) 109599.
URL https://linkinghub.elsevier.com/retrieve/pii/S0927025620300902

[140] A. M. Khorasani, I. Gibson, A. Ghasemi, A. Ghaderi, Modelling of laser powder bed fusion process and analysing the effective parameters on surface characteristics of Ti-6Al-4V, International Journal of Mechanical Sciences 168 (2020) 105299.
URL https://linkinghub.elsevier.com/retrieve/pii/S0020740319326463

[141] P. Chokshi, R. Dashwood, D. J. Hughes, Artificial Neural Network (ANN) based microstructural prediction model for 22MnB5 boron steel during tailored hot stamping, Computers & Structures 190 (2017) 162–172.
URL https://linkinghub.elsevier.com/retrieve/pii/S0045794917304856

[142] W. Marquardt, Adaptivity in Process Systems Modeling, in: Computer Aided Chemical Engineering, Vol. 10, Elsevier, 2002, pp. 42–56.
URL https://linkinghub.elsevier.com/retrieve/pii/S1570794602800384

[143] S. Mondal, D. Gwynn, A. Ray, A. Basak, Investigation of Melt Pool Geometry Control in Additive Manufacturing Using Hybrid Modeling, Metals 10 (5) (2020) 683.
URL https://www.mdpi.com/2075-4701/10/5/683/htm

[144] L. C. Dial, S. Ghosh, N. C. Kumar, V. S. Kumar, V. K. Gupta, T. Hanlon, V. S. Dheeradhada, K. S. Aggour, J. Vinciquerra, A physics-informed data driven approach to additive manufacturing parameter optimization, Advanced Materials & Processes 177 (7) (2019) 16–21.
URL https://go.gale.com/ps/i.do?p=AONE{&}sw=w{&}issn=08827958{&}v=2.1{&}it=r{&}id=GALE{%}7CA604896706{&}sid=googleScholar{&}linkaccess=fulltext

[145] Q. Zhu, Z. Liu, J. Yan, Machine learning for metal additive manufacturing: predicting temperature and melt pool fluid dynamics using physics-informed neural networks, Computational Mechanics 67 (2) (2021) 619–635.
URL https://link.springer.com/article/10.1007/s00466-020-01952-9

[146] A. Haghighi, L. Li, A hybrid physics-based and data-driven approach for characterizing porosity variation and filament bonding in extrusion-based additive manufacturing, Additive Manufacturing 36 (2020) 101399.
URL https://linkinghub.elsevier.com/retrieve/pii/S2214860420307715

[147] B. Kapusuzoglu, S. Mahadevan, Physics-Informed and Hybrid Machine Learning in Additive Manufacturing: Application to Fused Filament Fabrication, JOM 72 (12) (2020) 4695–4705.
URL https://link.springer.com/10.1007/s11837-020-04438-4

[148] Y. Du, T. Mukherjee, T. DebRoy, Physics-informed machine learning and mechanistic modeling of additive manufacturing to reduce defects, Applied

Materials Today 24 (2021) 101123.
URL https://linkinghub.elsevier.com/retrieve/pii/S2352940721001888

[149] ASTM Int., ASTM, Standard Test Methods for Tension Testing of Metallic Materials, Astm (C) (2009) 1–27.
URL http://www.astm.org/Standards/E8.htm

[150] Electro Optical Systems Finland Oy, Material data sheet EOS StainlessSteel PH1 (2017).
URL https://cdn0.scrvt.com/eos/2c79c109ca82d0e7/07f8e87d836c/SS-PH1-M290{_}Material{_}data{_}sheet{_}01-17{_}en.pdf

[151] E. GmbH, Electro Optical Systems, EOS NickelAlloy IN718 Material Data Sheet 49 (2020) 5.
URL https://cdn.eos.info/42267944478781ab/dce8f525f068/NiAll-IN718-M400W{_}Material{_}data{_}sheet{_}03-16{_}en.pdf

[152] J. M. Moyer, G. S. Ansell, The volume expansion accompanying the martensite transformation in iron-carbon alloys, Metallurgical Transactions A 1975 6:9 6 (9) (1975) 1785–1791.
URL https://link.springer.com/article/10.1007/BF02642308

[153] C. Buchanan, V.-P. Matilainen, A. Salminen, L. Gardner, Structural performance of additive manufactured metallic material and cross-sections, Journal of Constructional Steel Research 136 (2017) 35–48.
URL https://www.sciencedirect.com/science/article/pii/S0143974X16307714{#}f0020

[154] A. Dempsey, D. Liu, A. N. Palazotto, R. Abrahams, Dynamic Properties of Additively Manufactured 15-5 Stainless Steel and Three-Dimensional Microstructure Characterization, in: 57th AIAA/ASCE/AHS/ASC Structures, Structural Dynamics, and Materials Conference, American Institute of Aeronautics and Astronautics, Reston, Virginia, 2016.
URL http://arc.aiaa.org/doi/10.2514/6.2016-1510

[155] E.-W. Huang, S. Y. Lee, J. Jain, Y. Tong, K. An, N.-T. Tsou, T.-N. Lam, D. Yu, H. Chae, S.-W. Chen, S.-M. Chen, H.-S. Chou, Hardening steels by the generation of transient phase using additive manufacturing, Intermetallics 109 (2019) 60–67.
URL https://linkinghub.elsevier.com/retrieve/pii/S0966979519301074

[156] Y. Sun, R. J. Hebert, M. Aindow, Effect of heat treatments on microstructural evolution of additively manufactured and wrought 17-4PH stainless steel, Materials & Design 156 (2018) 429–440.
URL https://linkinghub.elsevier.com/retrieve/pii/S0264127518305434

[157] H. Chae, E.-W. Huang, J. Jain, H. Wang, W. Woo, S.-W. Chen, S. Harjo, T. Kawasaki, S. Y. Lee, Plastic anisotropy and deformation-induced phase transformation of additive manufactured stainless steel, Materials Science and Engineering: A 762 (2019) 138065.
URL https://linkinghub.elsevier.com/retrieve/pii/S0921509319308512

[158] D. M. Jafarlou, C. Walde, V. K. Champagne, S. Krishnamurty, I. R. Grosse, Influence of cold sprayed Cr3C2-Ni coating on fracture characteristics of additively manufactured 15Cr-5Ni stainless steel, Materials & Design 155 (2018) 134–147.
URL https://linkinghub.elsevier.com/retrieve/pii/S0264127518304489

[159] D. Croccolo, M. De Agostinis, S. Fini, G. Olmi, N. Bogojevic, S. Ciric-Kostic, HOW BUILD ORIENTATION AND THICKNESS OF ALLOWANCE MAY AFFECT THE FATIGUE RESPONSE OF DMLS PRODUCED 15-5 PH STAINLESS STEEL, 2018.
URL http://www.eos.info/material-

[160] M. Alnajjar, F. Christien, K. Wolski, C. Bosch, Evidence of austenite by-passing in a stainless steel obtained from laser melting additive manufacturing, Additive Manufacturing 25 (2019) 187–195.
URL https://linkinghub.elsevier.com/retrieve/pii/S2214860418304664

[161] C. J. Slunder, A. F. Hoenie, A. M. Hall, Thermal and mechanical treatment for precipitation hardening stainless steels, Tech. rep. (oct 1967).

[162] Y. Lu, S. Wu, Y. Gan, T. Huang, C. Yang, L. Junjie, J. Lin, Study on the microstructure, mechanical property and residual stress of SLM Inconel-718 alloy manufactured by differing island scanning strategy, Optics & Laser Technology 75 (2015) 197–206.
URL https://linkinghub.elsevier.com/retrieve/pii/S0030399215002108

[163] C. Silva, M. Song, K. Leonard, M. Wang, G. Was, J. Busby, Characterization of alloy 718 subjected to different thermomechanical treatments, Materials

Science and Engineering: A 691 (2017) 195–202.
URL https://linkinghub.elsevier.com/retrieve/pii/S0921509317303350

[164] C. Slama, M. Abdellaoui, Structural characterization of the aged Inconel 718, Journal of Alloys and Compounds 306 (1-2) (2000) 277–284.
URL https://linkinghub.elsevier.com/retrieve/pii/S0925838800007891

[165] J. Schröder, T. Mishurova, T. Fritsch, I. Serrano-Munoz, A. Evans, M. Sprengel, M. Klaus, C. Genzel, J. Schneider, G. Bruno, On the influence of heat treatment on microstructure and mechanical behavior of laser powder bed fused Inconel 718, Materials Science and Engineering: A 805 (2021) 140555.
URL https://linkinghub.elsevier.com/retrieve/pii/S092150932031618X

[166] Z. Huda, T. Zaharinie, H. Metselaar, S. Ibrahim, G. J. Min, Kinetics of Grain Growth in 718 Ni-Base Superalloy, Archives of Metallurgy and Materials 59 (3) (2014) 847–852.
URL http://journals.pan.pl/dlibra/publication/102721/edition/88738/content

[167] Z. Guo, W. Sha, Quantification of Precipitation Hardening and Evolution of Precipitates, MATERIALS TRANSACTIONS 43 (6) (2002) 1273–1282.
URL https://www.jstage.jst.go.jp/article/matertrans/43/6/43{_}6{_}1273/{_}article

[168] S. Zhang, X. Lin, L. Wang, X. Yu, Y. Hu, H. Yang, L. Lei, W. Huang, Strengthening mechanisms in selective laser-melted Inconel718 superalloy, Materials Science and Engineering: A 812 (2021) 141145.
URL https://linkinghub.elsevier.com/retrieve/pii/S0921509321004147

[169] F. Jafarian, M. Imaz Ciaran, D. Umbrello, P. Arrazola, L. Filice, H. Amirabadi, Finite element simulation of machining Inconel 718 alloy including microstructure changes, International Journal of Mechanical Sciences 88 (2014) 110–121.
URL https://linkinghub.elsevier.com/retrieve/pii/S0020740314002720

[170] W. Huang, Z. Wang, J. Yang, H. Yang, X. Zeng, Effects of process parameters and heat treatment on the microstructure and mechanical properties of selective laser melted Inconel 718, in: Solid Freeform Fabrication 2018: Proceedings

of the 29th Annual International Solid Freeform Fabrication Symposium - An Additive Manufacturing Conference, SFF 2018, 2020, pp. 1268–1276.

[171] V. Popovich, E. Borisov, A. Popovich, V. Sufiiarov, D. Masaylo, L. Alzina, Impact of heat treatment on mechanical behaviour of Inconel 718 processed with tailored microstructure by selective laser melting, Materials & Design 131 (2017) 12–22.
URL https://linkinghub.elsevier.com/retrieve/pii/S0264127517305476

[172] M. Aydinöz, F. Brenne, M. Schaper, C. Schaak, W. Tillmann, J. Nellesen, T. Niendorf, On the microstructural and mechanical properties of post-treated additively manufactured Inconel 718 superalloy under quasi-static and cyclic loading, Materials Science and Engineering: A 669 (2016) 246–258.
URL https://linkinghub.elsevier.com/retrieve/pii/S0921509316306062

[173] M. M. Kirka, F. Medina, R. Dehoff, A. Okello, Mechanical behavior of post-processed Inconel 718 manufactured through the electron beam melting process, Materials Science and Engineering: A 680 (2017) 338–346.
URL https://linkinghub.elsevier.com/retrieve/pii/S0921509316312904

[174] A. Strondl, M. Palm, J. Gnauk, G. Frommeyer, Microstructure and mechanical properties of nickel based superalloy IN718 produced by rapid prototyping with electron beam melting (EBM), Materials Science and Technology 27 (5) (2011) 876–883.
URL https://www.tandfonline.com/doi/abs/10.1179/026708309X12468927349451

[175] K. A. Unocic, L. M. Kolbus, R. R. Dehoff, S. N. Dryepondt, B. A. Pint, High-Temperature Performance of UNS N07718 Processed by Additive Manufacturing, in: NACE Corrosion, 2014.
URL https://www.researchgate.net/publication/276353527

[176] D. Zhang, W. Niu, X. Cao, Z. Liu, Effect of standard heat treatment on the microstructure and mechanical properties of selective laser melting manufactured Inconel 718 superalloy, Materials Science and Engineering: A 644 (2015) 32–40.
URL https://linkinghub.elsevier.com/retrieve/pii/S0921509315300745

[177] M. Kirka, D. Greeley, C. Hawkins, R. Dehoff, Effect of anisotropy and texture on the low cycle fatigue behavior of Inconel 718 processed via electron beam

melting, International Journal of Fatigue 105 (2017) 235–243.
URL https://linkinghub.elsevier.com/retrieve/pii/S014211231730350X

[178] J. Strößner, M. Terock, U. Glatzel, Mechanical and Microstructural Investigation of Nickel-Based Superalloy IN718 Manufactured by Selective Laser Melting (SLM), Advanced Engineering Materials 17 (8) (2015) 1099–1105.
URL http://doi.wiley.com/10.1002/adem.201500158

[179] S. Sui, H. Tan, J. Chen, C. Zhong, Z. Li, W. Fan, A. Gasser, W. Huang, The influence of Laves phases on the room temperature tensile properties of Inconel 718 fabricated by powder feeding laser additive manufacturing, Acta Materialia 164 (2019) 413–427.
URL https://linkinghub.elsevier.com/retrieve/pii/S1359645418308322

[180] L. Zhu, Z. Xu, Y. Gu, Effect of laser power on the microstructure and mechanical properties of heat treated Inconel 718 superalloy by laser solid forming, Journal of Alloys and Compounds 746 (2018) 159–167.
URL https://linkinghub.elsevier.com/retrieve/pii/S0925838818307576

[181] Y. L. Kuo, S. Horikawa, K. Kakehi, The effect of interdendritic δ phase on the mechanical properties of Alloy 718 built up by additive manufacturing (2017).

[182] D. Deng, J. Moverare, R. L. Peng, H. Söderberg, Microstructure and anisotropic mechanical properties of EBM manufactured Inconel 718 and effects of post heat treatments, Materials Science and Engineering: A 693 (2017) 151–163.
URL https://linkinghub.elsevier.com/retrieve/pii/S0921509317303994

[183] N. El-Bagoury, T. Matsuba, K. Yamamoto, H. Miyahara, K. Ogi, Influence of Heat Treatment on the Distribution of Ni₂Nb and Microsegregation in Cast Inconel 718 Alloy, MATERIALS TRANSACTIONS 46 (11) (2005) 2478–2483.
URL https://www.jstage.jst.go.jp/article/matertrans/46/11/46{_}11{_}2478/{_}article

[184] M. Rafiei, H. Mirzadeh, M. Malekan, Micro-mechanisms and precipitation kinetics of delta (δ) phase in Inconel 718 superalloy during aging, Journal of Alloys and Compounds 795 (2019) 207–212.
URL https://linkinghub.elsevier.com/retrieve/pii/S0925838819316597

[185] Lyu, Liu, Hu, Yang, Huang, Shi, The δ Phase Precipitation of an Inconel 718 Superalloy Fabricated by Electromagnetic Stirring Assisted Laser Solid Forming, Materials 12 (16) (2019) 2604.
URL /pmc/articles/PMC6720743//pmc/articles/PMC6720743/?report=abstracthttps://www.ncbi.nlm.nih.gov/pmc/articles/PMC6720743/ https://www.mdpi.com/1996-1944/12/16/2604

[186] S. Metals, SPECIAL METALS INCONEL G-3, Alloy Digest 70 (8) (2021) 1–28.
URL http://www.specialmetals.com/assets/smc/documents/inconel{_}alloy{_}718.pdfhttps://dl.asminternational.org/alloy-digest/article/70/8/Ni-774/17730/SPECIAL-METALS-INCONEL-G-3Ni-22-25Cr-19-5Fe-7Mo